Interpretation of L-band brightness temperatures of differently tilled bare soil plots

Marin Dimitrov

Energie & Umwelt / Energy & Environment
Band / Volume 292
ISBN 978-3-95806-098-2

JÜLICH
FORSCHUNGSZENTRUM

Energie & Umwelt / Energy & Environment
Band / Volume 292
ISBN 978-3-95806-098-2

JÜLICH
FORSCHUNGSZENTRUM

Schriften des Forschungszentrums Jülich
Reihe Energie & Umwelt / Energy & Environment Band / Volume 292

Forschungszentrum Jülich GmbH
Institute of Bio- and Geosciences
Agrosphere (IBG-3)

Interpretation of L-band brightness temperatures of differently tilled bare soil plots

Marin Dimitrov

Schriften des Forschungszentrums Jülich
Reihe Energie & Umwelt / Energy & Environment Band / Volume 292

ISSN 1866-1793 ISBN 978-3-95806-098-2

Bibliographic information published by the Deutsche Nationalbibliothek.
The Deutsche Nationalbibliothek lists this publication in the Deutsche
Nationalbibliografie; detailed bibliographic data are available in the
Internet at http://dnb.d-nb.de.

Publisher and Distributor: Forschungszentrum Jülich GmbH
Zentralbibliothek
52425 Jülich
Tel: +49 2461 61-5368
Fax: +49 2461 61-6103
Email: zb-publikation@fz-juelich.de
www.fz-juelich.de/zb

Cover Design: Grafische Medien, Forschungszentrum Jülich GmbH

Printer: Grafische Medien, Forschungszentrum Jülich GmbH

Schriften des Forschungszentrums Jülich
Reihe Energie & Umwelt / Energy & Environment, Band / Volume 292

D 5 (Diss., Bonn, Univ., 2015)

ISSN 1866-1793
ISBN 978-3-95806-098-2

The complete volume is freely available on the Internet on the Jülicher Open Access Server (JuSER)
at www.fz-juelich.de/zb/openaccess.

Summary

The structure of the surface soil layer is strongly influenced by soil tillage practices with important consequences for the soil hydraulic properties and soil moisture dynamics in the top soil layer. In this study, an L-band microwave radiometer and an infrared camera were used to monitor bare soil plots with different structure: tilled, seedbed, and compacted plots. The L-band brightness temperatures were calculated from the raw radiometric data using the radiometer effective transmissivity estimated with the described new algorithm for sky calibration. The new calibration algorithm reduces the bias of brightness temperature estimates. Radiative transfer, dielectric mixing, roughness correction, and soil hydrological models were coupled to determine and disentangle soil hydraulic and surface roughness parameters of the bare soil plots from time series of L-band brightness temperatures using inverse modeling. Two soil hydraulic property models were considered: the uni-modal model of Mualem van Genuchten and the bi-modal model of Durner. Microwave radiative transfer was modeled by two different approaches: the Fresnel equation with depth averaged dielectric permittivity of 2 cm or 5 cm thick surface layers, and a coherent radiative transfer model (CRTM) that accounts for vertical gradients in dielectric permittivity. Two global optimization algorithms ($DREAM_{ZS}$ and SCE-UA) were implemented to estimate the optimal solution and the posterior distribution of the soil hydraulic and surface roughness parameters. Brightness temperatures simulated by the CRTM and the 2-cm layer Fresnel model fitted well to the measured ones suggesting that L-band brightness temperatures may be linked to the soil moisture in a 2 cm thick surface layer. Differences in absolute and normalized L-band brightness temperatures between the plots reflect the effect of tillage on the soil structure. The inversely estimated surface roughness parameters compared well with those derived from laser profiler measurements. Both the laboratory derived and the retrieved from L-band brightness temperatures water retention curves were bi-modal. In order to validate the inversely retrieved soil hydraulic functions, simulated water contents were compared with in situ measurements and differences in predicted evaporation rates between the plots were compared with differences in measured IR temperatures. Depth specific calibration relations were found to be essential to derive soil moisture from near-to-surface installed sensors. Furthermore, differences in simulated actual evaporation rates between the plots were confirmed by observed differences in measured IR temperatures.

The results, presented in this study, indicate that effects of soil management on soil surface roughness and soil hydraulic properties can be inferred from L-band brightness temperatures.

Zusammenfassung

Die hydraulischen Eigenschaften von Böden und die zeitliche Dynamik der Bodenfeuchte werden im Wesentlichen von der Bodenstruktur bestimmt, die durch Bodenbearbeitung in der obersten Bodenschicht stark beeinflusst wird. In dieser Studie wurden daher verschiedene Bodeneigenschaften unterschiedlich intensiv bearbeiteter vegetationsloser Bödenstrukturen (d.h. nach Pflügen; nach Pflügen und Eggen; nach Pflügen, Eggen und Verdichten) über fünf Zeiträume von 28 Tagen mit einem L-Band Radiometer, einer Infrarotkamera und einigen Bodenfeuchtesensoren, erfasst.

Da die Ableitung von den uni-modalen Mualem van Genuchten (MvG) und bi-modalen Durner hydraulischen Parametern aus L-Band Radiometerdaten von besonderem Interesse war, wurden diverse Modelle in einer Inversionsprozedur gekoppelt, die mit zwei globalen Optimierungsalgorithmen ($DREAM_{zs}$ und SCE-UA) gestartet wurden. Neben den hydraulischen Parametern wurden auch der Bodenwassergehalt der obersten Bodenschicht sowie die Korrektur der Rauigkeit bei allen drei Bodenstrukturen abgeleitet und mit gemessenen Werten verglichen.

Beide Algorithmen lieferten Ergebnisse, die einen starken Einfluss der Bodenbearbeitung zeigten. Die hydraulische Parametern, die für alle fünf verschiedene Messperioden ermitteln wurden, zeigten Unterschiede bei allen drei untersuchten Oberflächenstrukturen.

Der Vergleich der modellierten und gemessenen Bodenwassergehaltwerte mittels RMSD in den ersten 0 – 2 cm und 0 – 5 cm der Bodenschicht haben ergeben, dass die L-band Strahlungstemperaturen in einer Bodenschicht von 0 – 2 cm den Bodenwassergehalt genauer beschreiben, als die 0 – 5 cm Schicht. Weiterhin wurden Unterschiede in den simulierten tatsächlichen Verdunstungsraten zwischen den Strukturen durch beobachtete Unterschiede in den gemessenen mittels einer Infrarotkamera Oberflächentemperaturen ermittelt. Die Korrekturparameter der Oberflächenrauigkeit aller untersuchten Flächen, die aus der Inversionsprozedur berechnet wurden, waren in guter Übereinstimmung mit den gemessenen Parametern mit einem Laserprofilometer.

Die Ergebnisse, die in dieser Studie präsentiert sind, zeigen, dass hydraulische Parametern von vegetationslosen Böden aus L-Band Strahlungstemperaturen abgeleitet werden können und zwar für verschiedene Oberflächenstrukturen.

Content

Summary III
Zusammenfassung IV
Content V
List of figures VIII
List of tables XII
List of abbreviations XIV
I General introduction 15
1 Research unit MUSIS: overall goals of the research project 15
2 Background 16
II New improved algorithm for sky calibration of L-band radiometers JÜLBARA and ELBARA II 18
1 Abstract 19
2 Introduction 19
3 Calibration algorithms 19
3.1 Internal calibration 19
3.2 External calibration 20
3.2.1 Algorithm 1: Cable loss correction 20
3.2.2 Algorithm 2: Effective transmissivity 20
4 Sky measurements 21
5 Results and discussion 22
5.1 JÜLBARA 22
5.2 ELBARA II 24
6 Conclusions 26
7 Acknowledgments 26
III Soil hydraulic parameters and surface soil moisture of a tilled bare soil plot inversely derived from L-Band brightness temperatures 27
1 Abstract 28
2 Introduction 28
3 Materials and methods 31
3.1 Experimental setup and instrumentation 31
3.2 Models 32
3.2.1 Hydrologic model 32

3.2.2 Radiative transfer model 33
3.2.3 Coherent radiative transfer model (CRTM) 34
3.2.4 Fresnel equation 36
3.2.5 Surface roughness correction model 37
3.3 Model coupling and parameter estimation 38
3.4 Model validation 40
4 Results and discussion 42
4.1 Measured and modelled brightness temperature 42
4.2 Surface roughness correction factor 46
4.3 Water retention and hydraulic conductivity functions 48
4.4 Site- and depth- specific calibration of soil moisture sensors 53
4.5 Comparison between retrieved and in situ measured soil moisture 55
5 Summary and conclusion 62
6 Acknowledgments 64
IV Soil hydraulic parameters of bare soil plots with different soil structure inversely derived from L-band brightness temperatures 65
1 Abstract 66
2 Introduction 66
3 Materials and Methods 69
3.1 Experimental setup and instrumentation 69
3.2 Models 72
3.2.1 Governing flow equation and soil hydraulic properties 72
3.3 Model coupling and parameter estimation 73
3.3.1 Forward run and model coupling 73
3.3.2 Parameter estimation for plots with different soil structure 74
3.3.3 Global optimization algorithms 75
3.4 Objective / likelihood functions 75
4 Results and disscussion 76
4.1 Measured and modelled brightness temperature 76
4.2 Water retention and hydraulic conductivity functions 83
4.3 Surface roughness correction factor 88
4.4 Retrieved and in situ measured soil moisture content 90
4.5 Soil surface temperature and evaporation 96
5 Summary and conclusion 99

6 Acknowledgments 101
V Synopsis 102
1 Summarizing conclusions 102
2 Outlook 103
References 105
Acknowledgements 116

List of figures

Figure I.1 Scales on the soil surface, covered by MUSIS. The subprojects with their abbreviations and working zones are shown as P2-P9. 15
Figure II.1 (a) JÜLBARA gain variations with air temperature. (b) JÜLBARA effective transmissivity variations with air temperature. 22
Figure II.2 ELBARA II effective transmissivities variations with air temperature: (a) horizontal polarization and (b) vertical polarization. 25
Figure III.1 L-band radiometer JÜLBARA and laser profiler over the plot (left). Mechanical field preparation (right). 31
Figure III.2 Parameters of the multilayer coherent radiative transfer model (from Bass et al., 1996) .. 35
Figure III.3 Flow chart of the coupled inversion procedure. Blue filled boxes represent models, white boxes are input or output variables, gray filled boxes are model parameters that are derived from minimizing the objective function (orange filled box), brown filled boxes are output variables that are compared with measurements. 40
Figure III.4 Time series (a-b) and one-to-one plots (c-d) of measured (blue line) and modeled brightness temperature TBHs from simulated soil moisture profiles using the Durner bi-modal model (DBM) coupled with the coherent radiative transfer model CRTM (magenta lines or dots) or with the Fresnel equation using the mean dielectric permittivity of the 0 - 2 cm surface layer (bright green lines or dots), or of the 0 - 5 cm surface layer (dark green lines or dots) for periods DOY 92-120, 2011 (a and c) and DOY 158-186, 2011 (b and d). Black lines in a-b represent the hourly precipitation rates during the investigated periods. 43
Figure III.5 Time series (a-c) of measured (blue line) and modeled brightness temperature TBHs from simulated soil moisture profiles using the Durner bi-modal model (DBM) coupled with the coherent radiative transfer model CRTM (magenta lines), or with the Fresnel equation using the mean dielectric permittivity of the 0 - 2 cm surface layer (bright green lines), or of the 0 - 5 cm surface layer (dark green lines) or for periods 2011: DOY 186-214 (a), 2011: DOY 226-254 (b) and 2009: DOY 272-300. Black lines represent the hourly precipitation rates during the investigated periods. 44
Figure III.6 RMSDs between measured and modeled L-band brightness temperatures (TBH) for different combinations of radiative transfer models: Fresnel or CRTM with soil hydraulic functions: (a) Durner bi-modal model (DBM) or (b) Mualem van Genuchten (MvG). 45
Figure III.7 Volumetric water content θ as a function of pressure head, h, (a, c) and hydraulic conductivity, K, as function of the volumetric water content (b, d) for the Durner bi-modal model (a, b) and the Mualem van Genuchten model (c, d). The parameters of the curves were retrieved from time series of the brightness temperatures using the coherent radiative transfer model (CRTM) for different time periods. The black lines represent water retention and conductivity curves that are derived from lab measurements: open circles are mean values and the bars represent the ranges. For the hydraulic conductivity curve, only the saturated hydraulic conductivity was measured. 49

Figure III.8 Volumetric water content θ as a function of pressure head, h, (a, c) and hydraulic conductivity, K, as function of the volumetric water content (b, d) for the Durner bi-modal model (a, b) and the Mualem van Genuchten model (c, d). The parameters of the curves were retrieved for different time periods from time series of the brightness temperatures using the Fresnel equation with depth averaged dielectric permittivity in the 0 - 2 cm layer. The black lines represent water retention and conductivity curves that are derived from lab measurements: open circles are mean values and the bars represent the ranges. For the hydraulic conductivity curve, only the saturated hydraulic conductivity was measured. 52

Figure III.9 Ratio of the Durner bi-modal to the Mualem van Genuchten unsaturated hydraulic conductivities KDBM/KMvG as a function of pressure head, h, which were retrieved for the different time periods from brightness temperatures (TBH) using the coherent radiative transfer model (a) or the Fresnel equation (b). 53

Figure III.10 Relation between gravimetrically measured volumetric moisture content, θ, and relative dielectric permittivity, ε_r, measured by DECAGON 5TE sensors at 2 cm (red stars) and 5 cm (blue stars) below the soil surface. The colored lines are fits of a quadratic equation through the measurement points and the black line represents the Topp equation (Topp et al., 1980), which is used by the sensors to calculate soil moisture. 54

Figure III.11 Time series for two periods: DOY 92-120, 2011 (a, b) and DOY 158-186, 2011 (c, d), and two depths: 2 cm (a, c) and 5 cm (b, d) of volumetric soil moisture contents, θ, that are obtained from sensor readings using a site and depth specific calibration (blue lines) and retrieved from L-band brightness temperatures using the Durner bi-modal hydraulic model coupled with the CRTM (magenta lines), or with the Fresnel equation using the mean dielectric permittivity of the 0 - 2 cm layer (bright green line) or of the 0 - 5 cm layer (dark green line). The transparent blue bands around the sensor readings represent the 95% confidence intervals of the mean of the sensor readings at a certain time and depth. 56

Figure III.12 Time series for 2011: DOY 188-216 (a), 2011: DOY 226-254 (b), and 2009: DOY 272-300 (c) of volumetric soil moisture contents, θ, at 2 cm depth that are obtained from sensor readings using a site and depth specific calibration (blue lines) and from brightness temperatures using the Durner bi-modal hydraulic model and the CRTM (magenta lines) model. The transparent blue bands around the sensor readings represent the 95% confidence intervals of the mean of the sensor readings at a certain time and depth. 57

Figure III.13 Time series for periods 2011: DOY 188-216 (a), 2011: DOY 226-254 (b), and 2009: DOY 272-300 (c) of volumetric soil moisture contents, θ, at 5 cm depth that are obtained from sensor readings using a site and depth specific calibration (blue lines) and from brightness temperatures using the Durner bi-modal hydraulic model and the CRTM (magenta lines) model. The transparent blue bands around the sensor readings represent the 95% confidence intervals of the mean of the sensor readings at a certain time and depth. 58

Figure III.14 RMSDs between measured soil moisture contents using a site and depth specific calibration, and retrieved soil moisture contents at 2 cm (a, c) and 5 cm (b, d) depth for all investigated periods (x-axis in DOY) and for different combinations of radiative transfer models: CRTM or Fresnel equation with depth averaged dielectric permittivity in the 0 - 2 cm or 0 - 5 cm surface layer; and different soil hydraulic functions: (a, b) Durner bi-modal model (DBM); or (c, d) Mualem van Genuchten (MvG)..... 59
Figure III.15 Time series for two periods: DOY 92-120, 2011 (a, b) and DOY 158-186, 2011 (c, d), and two depths: 2 cm (a, c) and 5 cm (b, d) of volumetric soil moisture contents, θ, that are obtained from sensor readings using a site and depth specific calibration (blue lines) and retrieved from brightness temperatures using the CRTM and the Durner bi-modal (magenta line) or the Mualem van Genuchten model (red line). The transparent blue bands represent the 95% confidence intervals of the mean of measured moisture contents at a certain time and depth. 60
Figure III.16 Time series for two periods: DOY 92-120, 2011 (a, b) and DOY 158-186, 2011 (c, d), and two depths: 2 cm (a, c) and 5 cm (b, d) of volumetric soil moisture contents, θ, that are retrieved from brightness temperatures using the CRTM and the Durner bi-modal model: at the respective depths (magenta line); that are averaged over the entire presumed sensor's measurement volume, i.e. with inclusion of an air layer for the sensor installed at 2 cm depth, (red line); or that are averaged over the sensor's measurement volume excluding this air layer (dark magenta line). 61
Figure IV.1 Top: mechanical field preparation (tilled plot (left from the tractor), seedbed plot (right from the tractor)). Photo from DOY 223. Bottom: location of the radiometer tower, different plots and -3 dB radiometer footprints, labeled lines and color scale denote the elevation (m.a.s.l.). 69
Figure IV.2 Tilled, seedbed and compacted plot (left). Topography of a 1500 x 500 mm area of the tilled, seedbed and compacted plot measured with the laser profiler. Photos and topography from DOY 96. 72
Figure IV.3 Time series of measured brightness temperatures TBHs from the tilled plot, the seedbed plot and the compacted plot, as well as cumulative rainfall for periods (a) DOY 92-120, (b) DOY 158-186, (c) DOY 188-216 and (d) DOY 226-254. 77
Figure IV.4 Time series of measured (dotted black line) and modeled (black line) brightness temperatures TBHs of the compacted plot for period DOY 92-120 (a) and DOY 158-186 (b). The transparent gray bands represent the 95% confidence intervals of the modeled brightness temperatures estimated with $DREAM_{ZS}$. 78
Figure IV.5 Time series of measured and modeled normalized TBHs, calculated as the difference between TBHs from tilled and compacted plots (a and c) or as the difference between TBHs from seedbed and compacted plots (b and d) for periods DOY 92-120 (a and b) and DOY 158-186 (c and d). 80
Figure IV.6 Time series of measured and modeled normalized TBH, calculated as the difference between TBHs from tilled and compacted plots (a and c) or as the difference between TBHs from

seedbed and compacted plots (b and d) for periods DOY 188-216 (a and b) and DOY 226-254 (c and d)..... 81
Figure IV.7 Volumetric water content θ (a, c, e), and hydraulic conductivity, K (b, d, f) as function of pressure head h. The parameters of the curves were derived from time series of the brightness temperatures using SCE-UA for tilled plot (a, b), seedbed plot (c, d) and compacted plot (e, f). The gray zones represent the 95% confidence intervals and were constructed using the marginal distributions of soil hydraulic parameters obtained with $DREAM_{zs}$ for the periods DOY 92-120 and DOY 158-186. 84
Figure IV.8 Histograms of the marginal posterior distributions of surface roughness parameter σ for periods DOY 92-120 (a-c) and DOY 158-186 (d-f) for tilled plot (a, d), seedbed plot (b, e) and compacted plot (c, f). The star represents the σ parameter in the parameter set with the highest likelihood. 88
Figure IV.9 Time series of volumetric soil moisture contents at 2 cm for tilled, seedbed and compacted plots: measured with soil moisture sensors (a) and retrieved from L-band brightness temperatures (b). Deviations from averaged moisture contents during a period: measured (c) and modeled (d). 91
Figure IV.10 Time series of volumetric soil moisture contents at 2 cm for tilled, seedbed, and compacted plots: measured with soil moisture sensors (a) and retrieved from L-band brightness temperatures (b). Deviations from averaged moisture contents during a period: measured (c) and modeled (d). 92
Figure IV.11 Time series of volumetric soil moisture contents at 2 cm for tilled, seedbed and compacted plots: measured with soil moisture sensors (a) and retrieved from L-band brightness temperatures (b). Deviations from averaged moisture contents during a period: measured (c) and modeled (d). 93
Figure IV.12 Time series of volumetric soil moisture contents at 2 cm for tilled, seedbed, and compacted plots: measured with soil moisture sensors (a) and retrieved from L-band brightness temperatures (b). Deviations from averaged moisture contents during a period: measured (c) and modeled (d). 94
Figure IV.13 Averages over time during an investigation period of modeled and measured soil moisture contents at 2 cm depth (a) and standard deviations of the variations over time during an investigation period of measured and modeled soil moisture contents (b). The symbols represent the plots and the colors the different periods. 95
Figure IV.14 Time series of differences of measured infrared temperature between the tilled and compacted plot and between the seedbed and compacted plot for period DOY 95-110 (a) and period DOY 165-180 (c). Potential evaporation and actual evaporation simulated with HYDRUS using the $DREAM_{zs}$ parameter set with the highest likelihood for tilled, seedbed and compacted plots (b and d). 97

List of tables

Table II.1 JÜLBARA results from DOY 91.71 to DOY 92.97, N = 1640, $TB_{,MODEL}$ = 5.11 K 23
Table II.2 JÜLBARA results from DOY 80.67 to DOY 80.92, N = 359, $TB_{,MODEL}$ = 5.12 K 23
Table II.3 ELBARA II results from DOY 192.68 to DOY 223.99, N = 13489, $TB_{,MODEL}$ = 4.92 K..... 24
Table III.1 Input and output of the coupled inversion scheme. 38
Table III.2 Ranges of air temperature, T_{air}, L-band brightness temperature for horizontal polarization, TBH, volumetric soil moisture, θ, and cumulative rainfall, rain, during the different observation periods. 39
Table III.3 Dates of mechanical field preparations and of laser profiler measurements, root-mean-square-roughness height σ: measured with laser profiler, calculated from the amount of rain since the measurement day until the end of the measurement period, σ(P) and inverted from measured brightness temperatures for different measurement periods. Values between parentheses are the minimal and maximal σ_i along individual profiles..... 47
Table III.4 Parameters of the Durner bi-modal soil hydraulic functions derived from lab measurements on soil cores and retrieved for the different measurement periods from measured brightness temperatures using coupled inversion with the CRTM or with Fresnel 0 – 2 cm. The last two rows show the ranges of inverted parameter values obtained for the different measurement periods. 50
Table III.5 Parameters of the Mualem van Genuchten soil hydraulic functions derived from lab measurements on soil cores and retrieved for the different measurement periods from measured brightness temperatures using coupled inversion with the CRTM or with Fresnel 0 – 2 cm. The first row shows the ranges of parameter values that were used for the inversion, last two rows show the ranges of inverted parameter values obtained for the different measurement periods. 51
Table IV.1 Parameters of the Durner bi-modal soil hydraulic functions estimated for the tilled plot and derived by $DREAM_{zs}$ and SCE-UA from measured L-band brightness temperatures using coupled inversion for the different measurement periods. 82
Table IV.2 Parameters of the Durner bi-modal soil hydraulic functions estimated for the seedbed plot and derived by $DREAM_{zs}$ and SCE-UA from measured L-band brightness temperatures using coupled inversion for the different measurement periods. 82
Table IV.3 Parameters of the Durner bi-modal soil hydraulic functions estimated for the compacted plot and derived by $DREAM_{zs}$ and SCE-UA from measured L-band brightness temperatures using coupled inversion for the different measurement periods. 83
Table IV.4 Dates of mechanical field preparations and of laser profiler measurements, root-mean-square-roughness height σ: measured with laser profiler and inverted with $DREAM_{zs}$ and SCE-UA from measured L-band brightness temperatures for different measurement periods and plots. Values given in parentheses are the minimal and the maximal σ_i along individual profiles. 89

Table IV.5 Potential evaporation and actual evaporation simulated with HYDRUS-1D using the $DREAM_{ZS}$ or SCE-UA parameter set with the highest likelihood for tilled, seedbed, and compacted plot..... 99

List of abbreviations

CA	Calibration assembly
CRTM	Coherent radiative transfer model
DBM	Durner bi-modal model
DOY	Day of year
DREAM	DiffeRential Evolution Adaptive Metropolis
FZJ	Research Centre Jülich
H-pol	Horizontal polarisation
MUSIS	Multi-Scale Interfaces in Unsaturated Soil
MvG	Mualem van Genuchten
RF	Radio frequency
RFI	Radio-frequency interference
RMSD	Root mean square deviation
RTM	Radiative transfer model
SCE-UA	Shuffled Complex Evolution
SMAP	Soil Moisture Active Passive Mission
SMOS	Soil Moisture and Ocean Salinity
TB	Brightness temperature
TBH	Brightness temperature at horizontal polarization
TERENO	TERrestrial ENviromental Observatories
UFZ	Centre for Environment Research
V-pol	Vertical polarisation

I General introduction

1 Research unit MUSIS: overall goals of the research project

The following work was done while working on a subproject within the international research unit “Multi-Scale Interfaces in Unsaturated Soil” (MUSIS) at the Institute Agrosphere (IBG-3), Research Centre Jülich, Germany.

MUSIS is a collaborative project of the University of Stuttgart, Technical University Braunschweig, Leibniz University Hannover, Swiss Federal Institute of Technology Zürich, Centre for Environment Research (UFZ) and Research Centre Jülich (FZJ). It is currently in its second research phase. During the first phase of MUSIS the hypothesis was that the different types of interfaces are not properly represented in flow models, which make flow models close to the soil surface so problematic. The scientific work was focused on the following three interfaces: 1) water – air interface as well as movement of fluids; 2) soil surface interface at the top soil layer and 3) the solid interfaces between pore and grain and between aggregates itself. Research activities were conducted at several scales: pore, cluster, and field plot scales (Figure I.1).

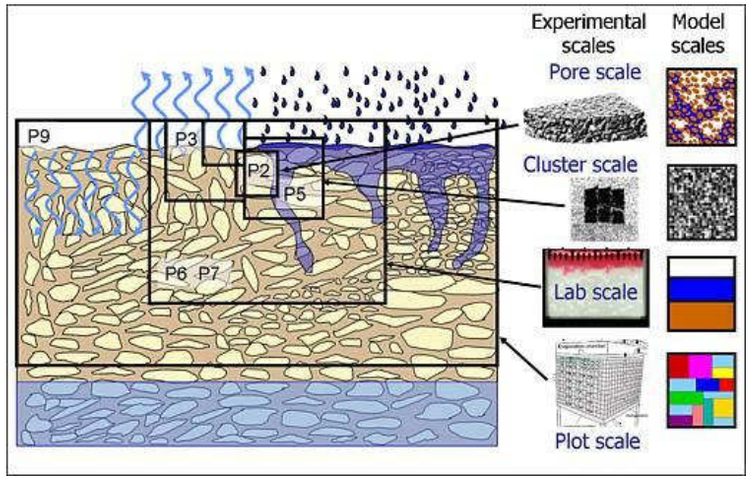

Figure I.1 Scales on the soil surface, covered by MUSIS. The subprojects with their abbreviations and working zones are shown as P2-P9.

Source: http://www.musis.uni-hannover.de/430.html

The work of the scientific team from the Institute Agrosphere, Research Centre Jülich, during this stage was primarily focused on examining the effect of different bare soil surface

structures on the L-band brightness temperature, infrared soil temperature, soil moisture content and soil hydraulic properties at field plot scale.

The overall goals of the scientific work were to provide answers to the following questions:

1. What is the effect of different bare soil surface structures on the physical properties of the surface layer?
2. Can hydraulic properties of different soil structures be derived using remote sensing measurements, which are related to the surface soil moisture (in particular measurements with L-band radiometer)?

Therefore, different ground-based sensors as well as remote sensing equipment were used to collect data from several measurement plots that were prepared with different soil surface structure. This information was consequently used to derive soil hydraulic properties, soil moisture and evaporation on the top soil layer. Since the used remote sensing methods cannot directly provide information about the soil physical properties, an inverse modeling was applied in this scientific work. Top-down approaches, where soil physical parameters can be estimated by inverse modeling of remote sensed data (Mohanty, 2013) were implemented at a field plot scale for three different types of soil structure.

2 Background

The correct estimation and characterization of the soil hydraulic properties of unsaturated soils play an important role for the proper interpretation of many problems in hydrology, ecology, environmental sciences, soil science, agriculture, and other disciplines (Durner and Lipsius, 2005). Information about the soil hydraulic properties is necessary in nearly all basic and applied aspects of soil, water, nutrient, and salinity management research. Moreover, the soil hydraulic properties are by far the most important land surface parameters that govern the partitioning of soil moisture between infiltration and evaporation fluxes at a range of spatial scales (Mohanty, 2013).

Soil moisture is a key variable for understanding the hydrological processes in the vadose zone (Vereecken et al., 2008). For weather and climate predictions from the regional to the global scale, an accurate knowledge of the soil moisture is needed. Measurements of soil moisture at the field plot scale can be used for determination of the soil water balance, for understanding of biogeochemical processes, for further development of hydrologic models. Different remote sensing techniques (instruments that are not in direct contact with the soil) can provide information about the surface soil moisture at the field plot scale. Within several

research programs or missions in the past decades near surface soil moisture was retrieved using passive microwave sensing equipment at the field plot scale.

The basis for low frequency microwave remote sensing of soil moisture is the strong contrast between the dielectric constant of water and dry soil. The emitted microwave radiation from the soil is influenced by the soil moisture content of the top soil layer, but also by the water present in the vegetation layer, soil texture, the soil and canopy temperatures, and nonetheless the soil surface roughness. All these factors should be taken into account during the retrieval of soil moisture from the measured microwave radiation. Within the retrieval, where several models are coupled, information about soil hydraulic properties can be extracted. However, accurate interpretation of microwave observations and their inversion for the estimation of hydrologic properties is challenging as each of the above listed factors has to be properly accounted for.

Soil hydraulic properties (i.e. water retention and hydraulic conductivity) are important land surface parameters that govern the partitioning of soil moisture between infiltration and evaporation fluxes at spatial scales (Mohanty, 2013). Some research groups parameterized soil hydraulic parameters and soil texture using a combination of satellite or aircraft based L-band data, soil moisture data and soil hydraulic properties (e.g. Hogue et al., 2005; Santanello Jr et al., 2007; Peters‐Lidard et al., 2008). On the other hand, short-term ground-based passive microwave campaigns conducted with L-band radiometer were used for prediction of water and energy fluxes (Camillo et al., 1986); of soil water retention, hydraulic conductivity, bulk density or air entry pressure (Burke et al., 1998) or of soil texture class (Chang and Islam, 2000). However, these radiometers must be calibrated very accurately, since the soil brightness temperature should be known to within 1 K (Delahaye et al., 2002).

II New improved algorithm for sky calibration of L-band radiometers JÜLBARA and ELBARA II

M. Dimitrov[(1)], K.G. Kostov[(2)], F. Jonard[(1)], K.Z. Jadoon[(1,3)], M. Schwank[(4)], L. Weihermüller[(1)], N. Hermes[(1)], J. Vanderborght[(1)], and H. Vereecken[(1)]

[(1)]Research Centre Jülich, Institute of Bio- and Geosciences: Agrosphere (IBG 3), 52425 Jülich, Germany
[(2)]Bulgarian Academy of Sciences, Institute of Electronics, 1784 Sofia, Bulgaria
[(3)]Water Desalination and Reuse Center, KAUST, Thuwal, 23955-6900, Saudi Arabia
[(4)]German Research Centre for Geosciences, 14473 Potsdam, Germany

Conference proceedings paper
doi:10.1109/MicroRad.2012.6185259
Microwave Radiometry and Remote Sensing of the Environment (MicroRad)
12th Specialist Meeting, 05.03.2012 – 09.03.2012, Rome, Italy

1 Abstract

We propose a new algorithm for sky calibration of the L-band radiometers JÜLBARA and ELBARA II, introducing the effective transmissivities of the instruments. The suggested approach was tested using experimental data obtained at the Selhausen test site, Germany. It was shown that for JÜLBARA the effective transmissivities depend strongly on the air temperature and decrease with increasing air temperature, while for ELBARA II such strong dependence was not observed. It was also shown that the effective transmissivities account for the antenna and feed cable loss effects, and for the variations of the radiometer gain due to air temperature changes. The new calibration algorithm reduces significantly the bias of brightness temperature estimates for both radiometers, especially for JÜLBARA.

2 Introduction

The sky emission is widely used as a well known noise source for external calibration of microwave radiometers. For L-band radiometers with built-in noise sources for internal calibration of the radiometer receiver, the sky calibration is also important for periodic external calibration of the radiometer system including the antenna and the feed cables.

The main goals of this study are: (a) to describe the new algorithm for sky calibration of the L-band radiometers JÜLBARA and ELBARA II, both of which have built-in noise sources for internal calibration (b) to present the experimental results, and (c) to compare the algorithms performance.

3 Calibration algorithms

3.1 Internal calibration

The noise temperatures $T_{B,INT,p}$ at the radiometer inputs for horizontal and vertical polarizations were calculated as follows:

$$T_{B,INT,p} = \frac{T_{HOT} - T_{COLD}}{U_{HOT} - U_{COLD}} \left(U_p - U_{COLD} \right) + T_{COLD}, \qquad \textbf{[II.I]}$$

where T_{HOT} and T_{COLD} are the noise temperatures of the internal hot and cold calibration sources ($T_{HOT} > T_{COLD}$), U_{HOT} and U_{COLD} are the corresponding instrumental raw data in units

of volts at the output of the RF path, and U_p are the voltages, associated with the antenna measurements with p = H and p = V for horizontal (H-pol) and vertical (V-pol) polarizations, respectively.

$$S = (T_{HOT} - T_{COLD})/(U_{HOT} - U_{COLD}) \qquad \textbf{[II.II]}$$

S (K/V) is the slope of the internal calibration equation and G = 1/S (V/K) is the net gain of the radiometer system including the RF-path.

3.2 External calibration

The radiometer systems were directed toward the sky and the brightness temperatures $T_{B,EXT,p}$ were estimated as presented below using two different algorithms.

3.2.1 Algorithm 1: Cable loss correction

As shown in (Schwank et al., 2010b) and (Schwank et al., 2012), the noise contributions due to feed cable loss $L_{FC,p}$ (dB) and cable temperature $T_{FC,p}$ (K) can be corrected using [II.III]

$$T_{B,EXT,p} = \frac{T_{B,INT,p} - (1 - t_{FC,p})T_{FC,p}}{t_{FC,p}}, \qquad \textbf{[II.III]}$$

where $t_{FC,p}$ is the feed cable transmissivity, which is calculated from the measured cable loss as follows:

$$t_{FC,p} = 10^{(-L_{FC,p}/10)}. \qquad \textbf{[II.IV]}$$

The measured air temperature was used as approximation for the cable temperature $T_{FC,p}$ as recommended in (Schwank et al., 2010b) and (Schwank et al., 2012).

3.2.2 Algorithm 2: Effective transmissivity

We introduce an effective transmissivity $t_{eff,p}$ defined as:

$$t_{eff,p} = \frac{T_{air} - T_{B,INT,p}}{T_{air} - T_{B,MODEL}}, \qquad \textbf{[II.V]}$$

where T_{air} (K) is the air temperature and $T_{B,MODEL}$ is the sky brightness temperature calculated from the model given in (Pellarin et al., 2003).

The new calibration algorithm is:

$$T_{B,EXT,p} = \frac{T_{B,INT,p} - (1 - t_{eff,p})T_{air}}{t_{eff,p}}. \qquad \textbf{[II.VI]}$$

4 Sky measurements

The experiments were conducted at the Selhausen test site of the Research Centre Jülich (FZJ), Germany. Radiometric measurements of the sky scene were performed with L-band radiometer JÜLBARA from April till September 2011, three times a day, namely from 7 to 8 am, from 3 to 4 pm, and from 11 pm to 0 am. The ELBARA II radiometer was also oriented toward the sky and measured continuously between 11 July and 11 August 2011. Measurements of the air temperature near to the radiometer systems were carried out simultaneously with the radiometric measurements. Measurements of the feed cables physical temperatures of JÜLBARA were also collected. The radiometers were mounted on different platforms, about 30 meters from each other. For the sky measurements the radiometers were oriented toward the south and toward the north, respectively with incidence angles of 135° for JÜLBARA and 140° for ELBARA II relative to nadir.

The Dicke-type radiometer JÜLBARA was built based on the same concept as the ELBARA radiometer (Matzler et al., 2003) and measures in the protected region of L-band at two frequency ranges 1.400–1.414 GHz (Channel 1 (CH1)) and 1.414–1.427 GHz (Channel 2 (CH2)), respectively. The radiometer was equipped with two internal calibration sources, namely hot noise source (338 K) and cold source (278 K), and a conical horn antenna with 12° full beamwidth at -3 dB. Detailed description of ELBARA II is given in (Schwank et al., 2010b). A resistive noise source and an active cold source were used as hot and cold calibration sources, respectively, in the ELBARA II calibration assembly (Schwank et al., 2010b). ELBARA II was equipped with a conical horn antenna with -3 dB full beamwidth of 24°. Both L-band radiometers worked with 10 seconds integration time. The radiometer resolution (sensitivity) was 0.1 K. One measurement cycle lasts about 45 seconds and was performed every minute (Schwank et al., 2010b).

5 Results and discussion

Equation [II.I] was used to calculate $T_{B,INT,p}$ from the raw radiometric data. Then $T_{B,EXT,p}$ were estimated using [II.III] for Algorithm 1 and [II.V] and [II.VI] for Algorithm 2. It should be noticed that

$$T_{B,p} = 0.5(T_{B,p,CH1} + T_{B,p,CH2}) \qquad \textbf{[II.VII]}$$

5.1 JÜLBARA

The mean values of the data obtained between 13th and 26th April 2011, during the one hour sky measurements from 3 pm to 4 pm will be used to illustrate the radiometer behavior and the algorithm performance. The feed cable losses were measured in the High Frequency Laboratory, Peter Grünberg Institute, FZJ. The mean values for the frequency range 1.400 – 1.420 GHz were used, namely 0.15 dB and 0.133 dB for the feed cables for H-pol and V-pol, respectively.

Figure II.1 (a) and (b) show the variations of the radiometer gain and the effective transmissivity $t_{eff,p}$ due to air temperature changes. It is obvious that both radiometer gain and effective transmissivity $t_{eff,p}$ depend on air temperature and decrease with increasing T_{air}.

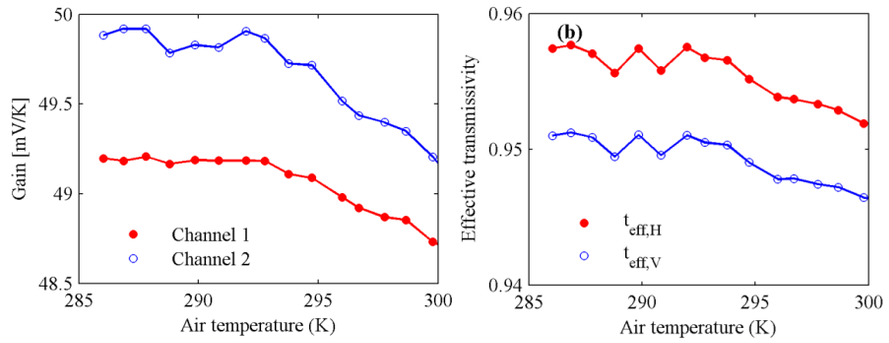

Figure II.1 (a) JÜLBARA gain variations with air temperature. (b) JÜLBARA effective transmissivity variations with air temperature.

The data obtained during continuous sky measurements from DOY 91.7132 to DOY 92.9715 were used to test the algorithm performance. Because of JÜLBARA orientation to the south, distinct contamination due to the sun emission was registered. The contaminated data from DOY 92.4396 to DOY 92.559 were removed and the remaining 1640 measurements were used for algorithm comparison. The results are summarized in Table II.1.

In all tables Delta = mean($T_{B,EXT,P}$) – mean($T_{B,MODEL}$) is calculated for the corresponding data set.

Table II.1 JÜLBARA results from DOY 91.71 to DOY 92.97, N = 1640, $TB_{,MODEL}$ = 5.11 K

			Mean $t_{eff,p}$		$t_{eff,p}$	
	$T_{B,H}$ (K)	$T_{B,V}$ (K)	Algorithm 1 Cable loss corr.	Algorithm 2	$T_{B,H}$	$T_{B,V}$
Min	4.06	7.27	1.78	1.98	5.07	5.07
Max	12.39	15.34	10.20	10.25	5.13	5.13
Mean	7.40	10.42	5.11	5.11	5.11	5.11
std	1.16	1.13	1.16	1.13	0.02	0.02
Delta	2.29	5.31	0.00	0.00	0.00	0.00

From the results presented in Table II.1 the following conclusions could be drawn: for Algorithm 1 there is a systematic bias between $T_{B,EXT}$ and $T_{B,MODEL}$, namely 2.29 K and 5.31 K at H-pol and V-pol respectively; for Algorithm 2 there is no bias. When Algorithm 2 is used with the mean values of the effective transmissivities calculated for the whole data set (n = 1640), the standard deviation is the same as for Algorithm 1. For Algorithm 2 with the instantaneous values of $t_{eff,p}$, the standard deviation (std) is very small.

Linear regression equations $t_{eff,H}$ (T_{air}) and $t_{eff,V}$ (T_{air}) were derived using the data set described above with n = 1640. Then Algorithm 2 was tested with another independent data set collected from DOY 80.6684 to DOY 80.9178, total duration six hours and n = 359. The results are presented in Table II.2. The linear regression equations $t_{eff,H}$ (T_{air}) and $t_{eff,V}$ (T_{air}) were used for estimating the effective transmissivities $t_{eff,p}$ from the measured air temperature T_{air}.

Table II.2 JÜLBARA results from DOY 80.67 to DOY 80.92, N = 359, $TB_{,MODEL}$ = 5.12 K

	Algorithm 1 Cable loss correction		*Algorithm 2* Linear regression $t_{eff,p}$ (T_{air})	
	$T_{B,H}$	$T_{B,V}$	$T_{B,H}$	$T_{B,V}$
Min	3.76	6.35	2.98	2.53
Max	8.78	12.89	7.40	8.16
Mean	6.81	9.64	5.43	5.23
std	0.98	1.07	0.79	0.86
Delta	1.69	4.52	0.31	0.11

The comparison of the results estimated with Algorithm 1 and Algorithm 2 presented in Table II.2 clearly shows the significant improvement of the calibration accuracy obtained using the new calibration algorithm – the bias is substantially reduced and the standard deviation is smaller.

5.2 ELBARA II

Distinct RFI were present in the sky radiometric data – bursts of the order of 40 to 60 K with a maximum of 450 K at H-polarization for DOY 207.378. The RFI-distorted periods were removed by using the following selection criterion:

$$\text{abs}((T_{B,CH1} - T_{B,CH2}) - \text{mean}(T_{B,CH1} - T_{B,CH2})) < 0.3\text{K}, \qquad \textbf{[II.VIII]}$$

where mean($T_{B,CH1}$- $T_{B,CH2}$) is the mean value calculated for the whole data set. The selection criterion given in [II.VIII] was applied for H-pol and V-pol data. Only the data fulfilling the criterion [II.VIII] simultaneously for H-pol and V-pol were used for algorithm testing. After the RFI removal, data set with n = 13489 was obtained.

The ELBARA II feed cable losses were specified as $L_H = L_V = 0.254$ dB by the manufacturer.

According to (Schwank et al., 2010b), the ELBARA II calibration assembly (CA) is designed as a separate module to allow for independent operation for cross calibration among other L-band radiometers. The temperature of the CA is stabilized to ± 0.1 K. The brightness temperature of the active cold source T_{ACS} was estimated from the measured temperature of the resistive noise source T_{RS}, mounted in the CA, using the linear regression equation given in Section 3.1.4 in (Schwank et al., 2010b). The brightness temperature T_{ACS} was calculated for every measurement cycle. Mean T_{ACS} = 40.99 K with standard deviation 0.016 K was obtained for the whole data set (n = 13489). The corresponding values for the CA temperatures, namely mean T_{RS} = 313.14 K and standard deviation 0.07 K confirmed the excellent temperature stability of the calibration assembly of ELBARA II reported in (Schwank et al., 2012).

The two algorithms for estimating $T_{B,EXT,p}$ were applied and the results are presented in Table II.3.

Table II.3 ELBARA II results from DOY 192.68 to DOY 223.99, N = 13489, $TB_{,MODEL}$ = 4.92 K

	Algorithm 1 Cable loss corr.		***Algorithm 2***			
			Mean $t_{eff,p}$		$t_{eff,p}$	
	$T_{B,H}$	$T_{B,V}$	$T_{B,H}$	$T_{B,V}$	$T_{B,H}$	$T_{B,V}$
Min	1.99	3.09	3.79	3.50	4.88	4.88
Max	6.28	9.75	8.04	10.15	4.95	4.95
Mean	3.16	4.50	4.92	4.92	4.92	4.92
std	0.49	0.69	0.49	0.69	0.01	0.01
Delta	- 1.76	- 0.42	0.00	0.00	0.00	0.00

For Algorithm 1 there is again a bias, namely – 1.76 K and – 0.42 K at H-pol and V-pol, respectively. The conclusions for Algorithm 2 are similar to that for JÜLBARA – no bias and very small standard deviation, in case that the instantaneous values of $t_{eff,p}$ were used.

Figure II.2 (a) and Figure II.2 (b) show the dependence of effective transmissivities $t_{eff,H}$ and $t_{eff,V}$ on the air temperature. There are two clusters: the first cluster (top) contains data suggesting linear dependence of $t_{eff,H}$ and $t_{eff,V}$ vs. T_{air} (small gradients $\Delta t_{eff,p}/\Delta T_{air}$); the second cluster contains data that deviate slightly from this linear dependence and also relatively small numbers of outliers. From the histograms of $t_{eff,H}$ and $t_{eff,V}$ presented in Figure II.2 (c) and Figure II.2 (d) it can be seen that most of the data are close to the corresponding average values. At H-pol about 80 % of the $t_{eff,H}$ data are in the range from 0.947 to 0.951, i.e. mean ($t_{eff,H}$) ± 0.002. At V-pol about 70 % of the $t_{eff,V}$ data are in the range from 0.943 to 0.947, i.e. mean ($t_{eff,V}$) ± 0.002. It should be noticed that change of $\Delta t_{eff} = 0.002$ of the effective transmissivities $t_{eff,H}$ and $t_{eff,V}$ leads to a corresponding change of $\Delta T_{B,EXT,p} \approx \Delta t T_{air} \approx 0.6$ K. It should be also mentioned that the change of $\Delta t_{eff} = 0.002$ corresponds to cable loss change of $\Delta L = 0.01$ dB.

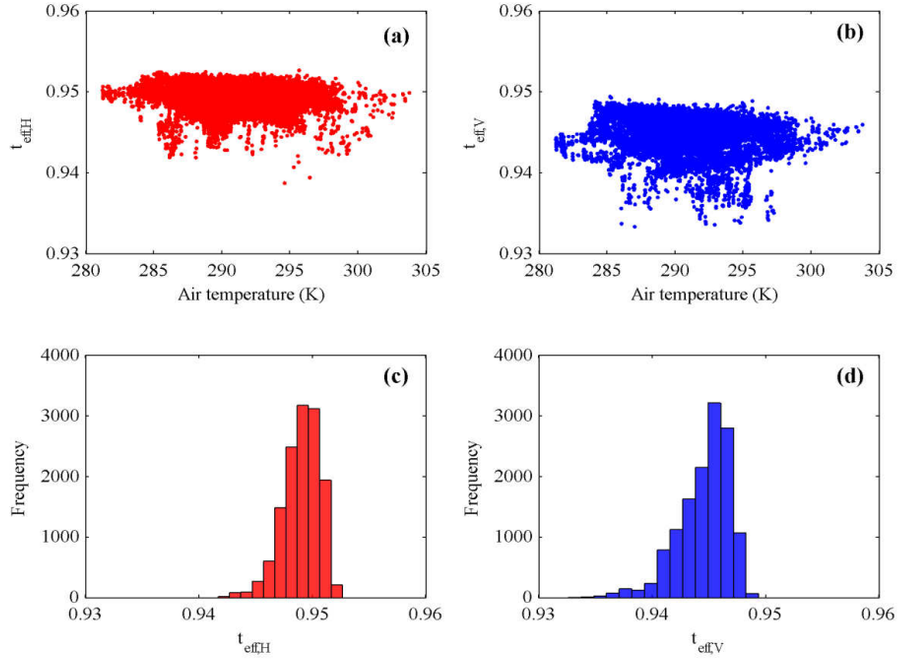

Figure II.2 ELBARA II effective transmissivities variations with air temperature: (a) horizontal polarization and (b) vertical polarization.

From the results presented for JÜLBARA and ELBARA II radiometers, it is obvious that the effective transmissivities $t_{eff,H}$ and $t_{eff,V}$ estimated using [II.VI] account for the feed cable

loss effects and for the variations of the radiometer gain due to air temperature changes. The effective transmissivities also account for the effects of antenna loss. As shown in (Zannoni et al., 2008), the antenna transmissivities for pyramidal rectangular horns are ≤ 1, namely 0.9920, 0.9872, and 0.9972 at 0.6, 0.82, and 2.5 GHz, respectively.

6 Conclusions

From this study the following conclusions could be drawn. The measured radiometric sky data must be RFI free. The air temperature may be used as a proxy for feed cable physical temperature, but care must be taken to ensure that the temperature sensor and the feed cables are protected from direct sunlight. The feed cable loss must be estimated very accurately in order to reduce the systematic bias of brightness temperatures obtained with Algorithm 1. It was shown that for JÜLBARA the effective transmissivities depend strongly on air temperature and decrease with increasing air temperature. It was proved that the linear regression equations $t_{eff,H}$ (T_{air}) and $t_{eff,V}$ (T_{air}) could be used for estimating the effective transmissivities from the measured air temperature. It was also shown that the new calibration algorithm reduces significantly the bias of brightness temperature estimates for both radiometers, especially for JULBARA.

We think that testing of the new calibration algorithm using data obtained with the other ELBARA II radiometers, currently operating in SMOS-relevant field campaigns in Europe, will be very beneficial for the radiometric community.

7 Acknowledgments

The authors express their thanks to H. Jagdfeld, T. Ortmanns and W. Schmitz from the Central Institute of Technology, FZJ. Special thanks to R. Harms and F. Engels from the Agrosphere Institute (IBG-3), to H. Meier from the Central Institute of Electronics, FZJ, and to A. Fox from the High Frequency Laboratory, Peter Grünberg Institute, FZJ.

The work presented here was carried out in the frame of the research group MUSIS funded by German Research Foundation (DFG) and of TERENO, funded by the Federal Ministry of Education and Research, Germany (BMBF).

III Soil hydraulic parameters and surface soil moisture of a tilled bare soil plot inversely derived from L-Band brightness temperatures

M. Dimitrov[(1)], J. Vanderborght[(1)], K.G. Kostov[(2)], K.Z. Jadoon[(1, 3)], L. Weihermüller[(1)], T. J. Jackson[(4)], R. Bindlish[(4)], Y. Pachepsky[(5)], M. Schwank[(6)] and H. Vereecken[(1)]

[(1)] Research Centre Jülich, Institute of Bio- and Geosciences: Agrosphere (IBG 3), Jülich, 52425, Germany

[(2)] Bulgarian Academy of Sciences, Institute of Electronics, Sofia, 1784, Bulgaria

[(3)] Water Desalination and Reuse Center, King Abdullah University of Science and Technology (KAUST), Thuwal, 23955-6900, Saudi Arabia

[(4)] USDA Agricultural Research Service, Hydrology and Remote Sensing Laboratory, Beltsville, 20705-2350, USA

[(5)] USDA Agricultural Research Service, Environmental Microbial and Food Safety Laboratory, Beltsville, 20705-2350, USA

[(6)] Swiss Federal Institute WSL, Mountain Hydrology and Torrents, Zürcherstrasse 111, 8903 Birmensdorf, Switzerland

Vadose Zone Journal 2014, Vol. 13, № 1
doi:10.2136/vzj2013.04.0075
Received: Apr 23, 2013
Published: January 13, 2014

1 Abstract

We coupled a radiative transfer model and a soil hydrological model HYDRUS 1D (Simunek et al., 2008) with an optimization routine to derive soil hydraulic parameters, surface roughness, and soil moisture of a tilled bare soil plot using measured brightness temperatures at 1.4 GHz (L-band), rainfall, and potential soil evaporation. The robustness of the approach was evaluated using five 28-day data sets representing different meteorological conditions. We considered two soil hydraulic property models: the uni-modal Mualem van Genuchten and the bi-modal model of Durner. Microwave radiative transfer was modeled by three different approaches: the Fresnel equation with depth averaged dielectric permittivity of either 2 or 5 cm thick surface layers and a coherent radiative transfer model (CRTM) that accounts for vertical gradients in dielectric permittivity. Brightness temperatures simulated by the CRTM and the 2-cm layer Fresnel model fitted well to the measured ones. L-band brightness temperatures are therefore related to the dielectric permittivity and soil moisture in a 2 cm thick surface layer. The surface roughness parameter that was derived from brightness temperatures using inverse modeling was similar to direct estimates from laser profiler measurements. The lab derived water retention curve was bi-modal and could be retrieved consistently for the different periods from brightness temperatures using inverse modeling. A uni-modal soil hydraulic property function underestimated the hydraulic conductivity near saturation. Surface soil moisture contents simulated using retrieved soil hydraulic parameters were compared with in-situ measurements. Depth specific calibration relations were essential to derive soil moisture from near-to-surface installed sensors.

2 Introduction

Knowledge about soil moisture and soil hydraulic properties is essential for weather and climate predictions, as well as to calculate the soil water balance and to determine plant growth and watershed run off (e.g. Robinson et al., 2008; Vereecken et al., 2008).

Passive microwave remote sensing at L-band (1-2 GHz) allows for the retrieval of soil moisture from the soil brightness temperature (e.g. Shutko, 1982; Schmugge, 1985; Jackson et al., 1999). For more than three decades, various measurement campaigns for estimation of soil moisture from brightness temperature using ground- or aircraft- based radiometers were carried out (e.g. de Rosnay et al., 2006; Bindlish et al., 2008; Jonard et al., 2011; Montzka et al., 2013). The satellite of the European Space Agency with its Soil Moisture and Salinity Mission (SMOS), which was launched successfully in 2009, and the one of NASA with its

Soil Moisture Active Passive Mission (SMAP), which is scheduled for launch in 2015, are equipped, among other measurement systems, with L-band radiometers for measuring brightness temperature (e.g. Entekhabi et al., 2010; Kerr et al., 2010). The data products can improve meteorological and climate predictions on a global scale (Kerr et al., 2010). On a smaller spatial scale, brightness temperatures measured using ground-based radiometers can provide information about the local surface soil moisture. This information is indispensable for the development of soil moisture retrieval models and the validation of corresponding space borne data products.

To simulate water and energy fluxes, the soil hydraulic properties, i.e. the soil water retention curve and the hydraulic conductivity curve which relate volumetric water content, water potential and hydraulic conductivity, are crucial (Camillo et al., 1986). Hydraulic soil properties are commonly measured in small soil samples. To simulate soil water fluxes on larger scales, spatial distributions of soil hydraulic parameters are derived from soil maps and databases using relationships between soil hydraulic parameters and soil properties, e.g. soil texture. However, soil hydraulic parameters are known to be highly spatially variable and the question whether soil properties measured on a small spatial scale can be used to predict time series of averaged fluxes and water contents on a larger spatial scale is the topic of intensive research (Vereecken et al., 2007). In order to tackle this mismatch between simulation and measurement scales, experimental methods that provide information about soil water content on a larger spatial scale, such as L-band radiometry, are of interest. This larger scale information of soil moisture could be used to derive with inverse modeling soil hydraulic parameters that are relevant at this scale.

The L-band brightness temperature is however not a direct measure of soil moisture. It depends on the vertical distributions of dielectric permittivity and soil temperature, and on soil surface roughness (Mattikalli et al., 1998). The dielectric permittivity depends strongly on the soil moisture content and is also influenced by other soil properties such as the bulk density, organic matter and clay content (e.g. Wang and Schmugge, 1980; Roth et al., 1990). To link the L-band brightness measurements to soil moisture contents, a coupled modeling approach that combines simulations of water, temperature, and dielectric permittivity profiles with simulations of brightness temperatures for a certain soil surface roughness seems necessary. The simulated soil moisture profiles depend on the meteorological boundary conditions (precipitation and soil evaporation) and the soil hydraulic properties. As a consequence, soil hydraulic properties may be retrieved from L-band brightness temperatures using coupled inverse modeling approaches in which models that simulate water and energy

fluxes in the soil profile are coupled with dielectric mixing and radiative transfer models (e.g. Camillo et al., 1986; Mattikalli et al., 1995; Burke et al., 1998; Mattikalli et al., 1998; Chang and Islam, 2000).

However, different radiative transfer and hydraulic property models can be used in the coupled inversion and the parameterization of the soil hydraulic functions as well as the prediction of the soil moisture contents may depend on the chosen models. Therefore, a validation of the derived surface soil moisture contents is necessary. For such a validation, in-situ installed soil moisture sensors need to be used. Such sensors always average soil moisture contents over a certain soil volume or a certain soil layer thickness. Especially for near surface measurements of soil moisture, the measurement volume of an in-situ sensor may extend into regions above the soil, which affects the sensor reading. Furthermore, the microwave emission depth increases with decreasing moisture (Escorihuela et al., 2010). Both instances make the validation of near surface soil moisture content retrieved from L-band brightness temperatures using in-situ soil moisture probes a non-trivial task.

In this study, we evaluated the effect of using different hydraulic property functions: the uni-modal Mualem van Genuchten model (MvG) (Van Genuchten, 1980) versus the bi-modal model of Durner (DBM) (Durner, 1994; Priesack and Durner, 2006), and of using different radiative transfer models: a coherent radiative transfer model (CRTM) that accounts for the effects of vertical gradients of dielectric permittivity close to the soil surface and the Fresnel equation which assumes a vertically homogeneous dielectric permittivity in the soil profile, on the retrieved soil moisture contents and soil hydraulic parameters. The retrieved soil moisture contents were compared with in-situ monitored soil moisture contents. Unlike the other studies presented above, which focused on relatively short measurement periods over undisturbed plots, we consider in this paper five 28-day time series consisting of several infiltration, redistribution and evaporation events in order to cover a wide range of soil hydrological conditions. For each time period, an independent set of inversely estimated hydraulic parameters was derived. Variation of estimated hydraulic parameters between different time periods could be due to changing hydraulic properties of the top soil layer over time. It could also be due to a lack of sensitivity of the L-Band brightness temperatures to a parameter so that this parameter cannot be estimated accurately from brightness temperatures using inverse modeling. By comparing the soil hydraulic properties obtained for the different measurement periods, the robustness of the obtained parameters by the inversion procedure was evaluated.

In addition, we monitored brightness temperatures of the relatively rough surface of a tilled soil. This adds additional complexity since an additional parameter, which needs to be estimated using the inversion routine, has to be included in the model to describe the microwave emission from a rough soil surface.

3 Materials and methods

3.1 Experimental setup and instrumentation

From September 2009 to December 2009 and from March 2011 to September 2011 a trapezoidal bare soil plot with widths between 12 m and 8 m and 28 m length was monitored after tilling using a spring tine cultivator (Figure III.1). The plot was located within the Selhausen test site of the Forschungszentrum Jülich, Germany, which is part of the TERENO observatory (Zacharias et al., 2011). The mechanical field preparation was repeated four times during the measurement campaigns: on September 27, 2009 (day of the year (DOY) 270), March 15, 2011 (DOY 74), May 27, 2011 (DOY 147) and August 11, 2011 (DOY 223), respectively. The field was kept free of weeds using herbicides. The soil has a silt loam texture (14.5 % sand, 69 % silt and 16.5 % clay), according to the U.S. Department of Agriculture (USDA) textural classification. A detailed description of the test site Selhausen is given by (Weihermuller et al., 2007).

Figure III.1 L-band radiometer JÜLBARA and laser profiler over the plot (left). Mechanical field preparation (right).

Ten ECH$_2$O 5TE sensors (Decagon Devices Inc., Pullman, WA, USA) were installed horizontally in five different locations at two different depths: 2 cm and 5 cm (five sensors per depth). Relative dielectric permittivity of the soil, ε_r, and soil temperature T_{Soil} (°C) were

recorded in 10 minutes intervals and stored automatically by two Em50 data loggers (Decagon Devices Inc., Pullman, WA, USA).

The Dicke-type L-band radiometer JÜLBARA (operation frequency of 1.4 GHz equivalent to wavelength of 21.4 cm) with dual-mode horn antenna (12° full beamwidth at -3 dB) was mounted on a fixed tower at 12.5 m height above the tilled plot to measure the brightness temperature TB (K) with fixed angle of incidence β_0 = 50° (accounting for a 2° slope of the field plot). JÜLBARA was developed as a successor of the ELBARA radiometer (Matzler et al., 2003) and measures in the protected L-band at two frequencies ranges (1.400 – 1.414 GHz and 1.414-1.427 GHz) simultaneously. The radiometer was equipped with two internal calibration sources: hot load (338 K) and cold load (278 K). Additionally, external calibration of the radiometer with sky measurements was performed daily during the whole investigation period in 2011 and periodically in 2009. The integration time of the measurements was set to 10 seconds and the sensitivity of the radiometer was 0.1 K. The measurements were recorded continuously in 2 minutes intervals, but hourly mean values of the measured TB were used in the calculations.

Two weather stations, located on the test site, were used to provide meteorological data during the whole investigation period. The measured air temperature, precipitation, wind speed, humidity at 2 m height and the solar and global radiation were used as forcing for the hydrological model. From the measured meteorological data, hourly potential evaporation was derived according to the FAO guidelines (Allen et al., 1998).

3.2 Models

3.2.1 Hydrologic model

In this study, 1-D vertical water flow was simulated in a homogeneous and isotropic rigid porous medium by Richards equation (Jury and Horton, 2004):

$$\frac{\partial \theta(h)}{\partial t} = \frac{\partial}{\partial z}\left[K(\theta)\left(\frac{\partial h}{\partial z} + 1\right)\right] \qquad \textbf{[III.I]}$$

where h (cm) is the pressure head, θ (cm^3 cm^{-3}) is the volumetric water content, K(θ) (cm/min) is the hydraulic conductivity function, and z (cm) is the elevation (positive upward).

We used either a uni-modal or a bi-modal pore size distribution model to describe the unsaturated soil hydraulic properties θ(h) and K(θ) in Eq. [III.I]. Both models use the

statistical pore-connection model of (Mualem, 1976) to derive the K(θ) from the θ(h) functions and use a functional form that was proposed by (Van Genuchten, 1980) to represent pore size distributions. The θ(h) and K(θ) functions can be represented in general as (Priesack and Durner, 2006)

$$\theta(h) = \begin{cases} \theta_r + (\theta_s - \theta_r)(w_1 S_{e1}(h) + w_2 S_{e2}(h)) & h < 0 \\ \theta_s & h \geq 0 \end{cases} \qquad \textbf{[III.II]}$$

$$S_{e,i}(h) = \left[1 + (\alpha_i |h|)^{n_i}\right]^{-m_i} \qquad \textbf{[III.III]}$$

$$K(\theta) = K_s \frac{(w_1 S_{e_1} + w_2 S_{e_2})^1 \left(w_1 \alpha_1 \left[1 - (1 - S_{e_1}^{1/m_1})^{m_1}\right] + w_2 \alpha_2 \left[1 - (1 - S_{e_2}^{1/m_2})^{m_2}\right] \right)^2}{(w_1 \alpha_1 + w_2 \alpha_2)^2} \qquad \textbf{[III.IV]}$$

where θ_r and θ_s are, respectively, the residual and saturated volumetric water contents ($cm^3\ cm^{-3}$), S_{ei} is the saturation degree of the i^{th} pore size distribution, α_i (cm^{-1}) and n_i are shape parameters, $m_i = 1\text{-}1/n_i$, and w_i is the volume fraction of the i^{th} pore size distribution with $w_1 + w_2 = 1$, and l is the pore-connectivity parameter which was assumed to be 0.5 (Mualem, 1976). For $w_2 = 0$, the pore size distribution is uni-modal and the Mualem-van Genuchten functions (MvG) are obtained (Van Genuchten, 1980). For $w_2 > 0$, the pore size distribution is bi-modal and the Durner bi-modal model (DBM) functions (Durner, 1994) are obtained.

The Richards equation was solved numerically using the HYDRUS 1D code (Simunek et al., 2008) for a 200 cm deep soil profile using a spatial discretization of 0.25 cm. Atmospheric boundary conditions using hourly measured rain, calculated potential evapotranspiration rates, and a unit hydraulic head gradient were defined at the top and bottom of the soil profile, respectively. As proposed by (Chanzy et al., 2008) for a wet climate, a uniform initial pressure head of -100 cm and a spin-up period of one month were used.

3.2.2 Radiative transfer model

The microwave brightness temperature of a soil medium, TB, is governed by the dielectric and temperature depth profiles. Brightness temperatures at horizontal polarization

TBH were used because they are more sensitive to soil moisture changes. Using radiative transfer theory, TBH is given by (Ulaby et al., 1986):

$$TBH = [1 - R_H]\, T_{eff} + TB_{sky} R_H \qquad \textbf{[III.V]}$$

where R_H is the reflectivity for horizontal polarization, and TB_{sky} is the sky brightness temperature that was calculated as in (Pellarin et al., 2003). T_{eff} in Eq. [III.V] is an effective soil temperature which can be calculated as shown in (Ulaby et al., 1986) if soil moisture and soil temperature profiles are available. Several models were proposed for simplifying the calculation of T_{eff} using limited profile information (Choudhury et al., 1982; Wigneron et al., 2001; Holmes et al., 2006). These models required the so called deep soil temperature T_{deep}, measured at least 50 cm below the soil surface. Wigneron et al., 2008, investigated also the simplest possible approximation $T_{eff} \approx T_s(z)$ for z in the range from 0 to 10 cm and found that reasonably good results were obtained for z in the range from 2 to 5 cm. We used the measured soil temperature at 2 cm as an approximation to T_{eff} because, firstly, we did not have experimental data for the deep soil temperature T_{deep}, and secondly, the measured temperature T_s (2 cm) characterizes well the temperature variations of the soil layer (0 - 2 cm), which thickness is close to the so called soil moisture sampling depth (e.g. Kostov and Vichev, 1995; Escorihuela et al., 2010).

In general, for simulation of soil reflectivity, R_H, the radiative transfer theory differentiates between coherent and non-coherent model approaches which, respectively, consider or do not consider the phase of the signal. Furthermore, the soil can either be considered to be a dielectrically layered or a homogeneous medium. In this study, we investigated the applicability of a coherent radiative transfer model that resolves the vertical gradients of dielectric permittivity due to gradients in soil moisture content and of the Fresnel equation that assumes a vertically uniform dielectric permittivity or water content in a surface soil layer.

3.2.3 Coherent radiative transfer model (CRTM)

When electromagnetic radiation falls onto a stack of thin films, multiple reflections take place within this structure. Depending on the source of radiation and the layer thickness, the reflected beams may be coherent and interfere with each other (Bass et al., 1996). Figure III.2 shows a thin-film system with N layers, where $p_i = \sqrt{\varepsilon_{r,i}}$ ($\varepsilon_{r,i}$ is the relative dielectric

permittivity of the i^{th} soil layer) is the refractive index and d_i is the thickness of i^{th} layer, and p_s and p_a are the refractive indices of the deeper soil or substrate and the air, respectively. The angle of incidence β_0, the frequency, f, and the polarization of the incident radiation are given as external variables of the system (Bass et al., 1996). The reflection coefficient r_H for horizontal polarization, which is related to the reflectivity R_H, as:

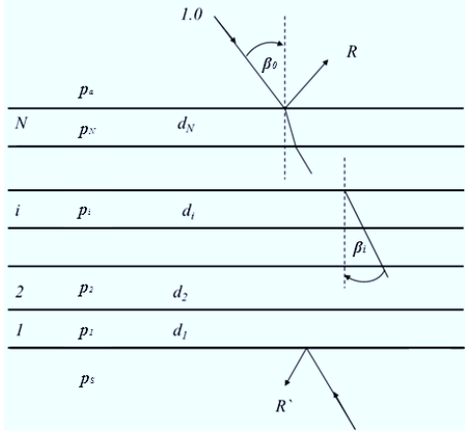

Figure III.2 Parameters of the multilayer coherent radiative transfer model (from Bass et al., 1996)

$$R_H = |r_H|^2 \qquad \textbf{[III.VI]}$$

is for the multilayer with N layers given by (Bass et al., 1996):

$$r_H = \frac{\eta_a E_a - H_a}{\eta_a E_a + H_a} \qquad \textbf{[III.VII]}$$

where η_a is effective refractive index of air and E_a and H_a are electric and magnetic vectors in the incident media (air). The effective refractive index of the soil medium or substrate is given by:

$$\eta_x = \frac{p_x}{\cos\beta_x} \qquad \textbf{[III.VIII]}$$

where β_x is the incidence angle in a layer or in the substrate which is related by Snell's law to the refractive index of the air and incidence angle β_0 as:

$$p_a \sin\beta_o = p_x \sin\beta_x \qquad \textbf{[III.IX]}$$

The vectors E_a and H_a are given by:

$$\begin{bmatrix} E_a \\ H_a \end{bmatrix} = M \begin{bmatrix} 1 \\ \eta_s \end{bmatrix} \qquad \textbf{[III.X]}$$

where M is the product matrix given by:

$$M = M_N M_{N-1} \ldots M_i \ldots M_2 M_1 \qquad \textbf{[III.XI]}$$

M_i in Eq. [III.XI] is a 2 x 2 matrix and represents the i^{-th} layer of the system:

$$M_i = \begin{bmatrix} \cos\partial_i & \frac{j}{\eta_i}\sin\partial_i \\ j\eta_i \sin\partial_i & \cos\partial_i \end{bmatrix} \qquad \textbf{[III.XII]}$$

where j is the imaginary number, $\partial_i = \frac{2\pi}{\lambda}(p_i d_i \cos\beta_i)$, and λ is the wavelength.

The considered layer thickness corresponded with the spatial discretization used for the soil water flow simulations using HYDRUS 1D and was 0.25 cm, which corresponds with approximately 1 % of the L-band wavelength in free space. In general, the layer thickness must be much smaller than the wavelength to obtain accurate results. The layer thickness of 0.25 cm was selected as a compromise between the model calculation time and accuracy.

From the simulated θ profiles, ε_r depth profiles were calculated using the dielectric mixing model (Wang and Schmugge, 1980).

3.2.4 Fresnel equation

For a soil with a smooth surface and constant dielectric properties with depth, the reflectivity R_H can be calculated using the Fresnel equation (Njoku and Entekhabi, 1996):

$$R_H = \left(\frac{\cos\beta_0 - \sqrt{\varepsilon_r - \sin^2\beta_0}}{\cos\beta_0 + \sqrt{\varepsilon_r - \sin^2\beta_0}} \right)^2 \qquad \textbf{[III.XIII]}$$

The relative dielectric permittivity ε_r in the Fresnel equation was obtained by taking the arithmetic mean of the relative dielectric permittivities in the 2 cm and in the 5 cm top soil layers, which were derived from HYDRUS 1D simulated θ profiles using a dielectric mixing model (Wang and Schmugge, 1980). These layers were selected because good correspondence between L-band brightness temperatures and soil moisture was observed experimentally for soil layer depths between 2 cm and 5 cm (Newton et al., 1982; Wang, 1987; Kostov and Vichev, 1995; Jackson et al., 1997). In the following, we will use Fresnel 0 - 5 cm and Fresnel 0 - 2 cm to indicate that TBH were calculated using the Fresnel equation (Eq. [III.XIII]) with averaged relative dielectric permittivities, ε_r, in the 0 - 5 cm and 0 - 2 cm surface soil layers, respectively.

3.2.5 Surface roughness correction model

For rough soil surface Eqs. [III.VI] and [III.XIII] for calculating the soil reflectivity must be modified to account for surface scattering. As the surface roughness increases, the brightness temperature increases and the sensitivity of brightness temperature to soil moisture decreases (Njoku and Entekhabi, 1996). Random rough surfaces are typically characterized in physically based radiative transfer models using statistical parameters, such as standard deviation of surface heights or the root-mean-square-roughness height, σ, spatial correlation length and spatial correlation function (Schwank et al., 2010a). These physically-based models provide insight into the scattering mechanisms, but are often computationally intensive and require detailed information about the surface roughness. For this reason, simpler semi-empirical roughness correction models were often used in retrieval and inversion algorithms.

We used a simpler model for correcting the roughness effects that was proposed by (Choudhury et al., 1979) and considers only the root-mean-square-roughness height, σ. According to this model, the rough surface reflectivity R_{rH}, is related to the reflectivity of a smooth surface R_H as:

$$R_{rH} = R_H \exp\left(-\frac{16\pi^2}{\lambda^2}\sigma^2 \cos^2\beta_0\right) \qquad \textbf{[III.XIV]}$$

This model was verified using radiometric measurements (Ulaby et al., 1986) and it was shown that σ values retrieved from brightness temperatures using Eq. [III.XIV] were smaller than the measured ones. Recently, (Wigneron et al., 2011) showed that σ that was estimated from L-band radiometric measurements using Eq. [III.XIV] underestimates the root-mean-square-roughness height that was derived from direct measurements. Therefore, σ in Eq. [III.XIV] was considered as an additional fitting parameter. It should be noted that this model does not consider the effects of larger scale (regular) structures, e.g. periodic structures with a scale larger than approximately 0.1 m, that cannot be treated as random roughness (Schwank et al., 2010a) and that might be expected in moldboard tilled fields. However, in chisel tilled fields such regular structures are less pronounced so that Eq. [III.XIV] was used to model the effect of surface roughness in this study.

3.3 Model coupling and parameter estimation

The models, described in the previous sections, were coupled as shown in Figure III.3. The HYDRUS 1D code was used to generate soil moisture profiles. Dielectric permittivity profiles $\varepsilon_r(z)$ were calculated from these soil moisture profiles using the dielectric model of (Wang and Schmugge, 1980). In the next step the reflectivity, R_H, was calculated from these $\varepsilon_r(z)$ profiles with the CRTM or the Fresnel model and corrected for surface roughness using Eq. [III.XIV]. Finally, brightness temperatures, TBH, were calculated using Eq. [III.V]. The models with their inputs and outputs are presented in Table III.1.

Table III.1 Input and output of the coupled inversion scheme.

Model	Input	Output
Hydrological model	rain, ETo	soil moisture profile
Dielectric model	soil moisture profile	relative dielectric permittivity $\varepsilon_r(z)$
CRTM, Fresnel equation	$\varepsilon_r(z)$	Reflectivity R_H
Roughness correction	R_H, roughness coefficient σ^2	Roughness corrected reflectivity, R_{rH}.
RTM	R_{rH}, effective temperature T_{eff}	Brightness temperatureTBH

In the optimization procedure, the objective function, i.e. the sum of the squared normalized differences between measured and modeled brightness temperatures, was minimized by fitting the hydraulic soil parameters of the top soil layer (0 – 30 cm) and the root-mean-square-roughness height σ. A global optimization approach, the Shuffled Complex

Evolution (SCE-UA) (Duan et al., 1993) was used to derive the optimal parameter set that minimizes the objective function.

Table III.2 Ranges of air temperature, T_{air}, L-band brightness temperature for horizontal polarization, TBH, volumetric soil moisture, θ, and cumulative rainfall, rain, during the different observation periods.

		T_{air} (K)	TBH (K)	θ 2cm (cm^3 cm^{-3})	θ 5cm (cm^3 cm^{-3})	Total rain (cm)
DOY	min	275.9	205.14	0.087	0.12	
92-120	max	300.6	279.58	0.184	0.195	1.49
2011	difference	24.7	74.44	0.097	0.075	
DOY	min	281.6	146.5	0.218	0.206	
158-186	max	306.8	232.4	0.362	0.347	13.32
2011	difference	25.2	85.9	0.144	0.141	
DOY	min	281.8	138.54	0.178	0.175	
188-216	max	302.3	263.9	0.315	0.286	6.61
2011	difference	20.5	125.36	0.137	0.111	
DOY	min	281.4	139.48	0.255	0.221	
226-254	max	306.3	250.6	0.391	0.369	9.01
2011	difference	24.9	111.12	0.137	0.149	
DOY	min	275.1	165.58	0.163	0.185	
272-300	max	293.16	251.2	0.326	0.335	5.7
2009	difference	18.06	85.62	0.163	0.15	

The data series was split up into five 28-d periods (DOY 272-300, 2009; DOY 92-120, 2011; DOY 158-186, 2011 DOY 188-216, 2011 and DOY 226-254, 2011). For each of these periods, the soil hydraulic parameters and root-mean-square-roughness height were optimized using the above described inversion approach. By splitting up the dataset, the inversion approach could be tested for different soil hydrological conditions. Some meteorological and measured parameters for all of the periods are summarized in Table III.2. In general the periods may be characterized as either: mostly dry with a maximal brightness temperature of 279.6 K (DOY 92-120, 2011), mostly wet with a minimal brightness temperature of 138.5 K (DOY 226-254, 2011 and DOY 188-216, 2011), or mixed (with dry and wet phases). The total amount of rain ranged between 1.49 cm (DOY 92-120, 2011) and 13.32 cm (DOY 158-186, 2011). The different amounts of rainfall in the different periods were reflected in large variations in surface soil moisture contents. Between some of these periods, a field preparation was done, which changed the surface roughness and the soil moisture sensors were reinstalled.

In the following, we focus on two time series that differed strongly: a dry period (DOY 92-120, 2011) and a wet period (DOY 158-186, 2011). Data for the other periods is also presented to demonstrate that similar results were obtained for these periods.

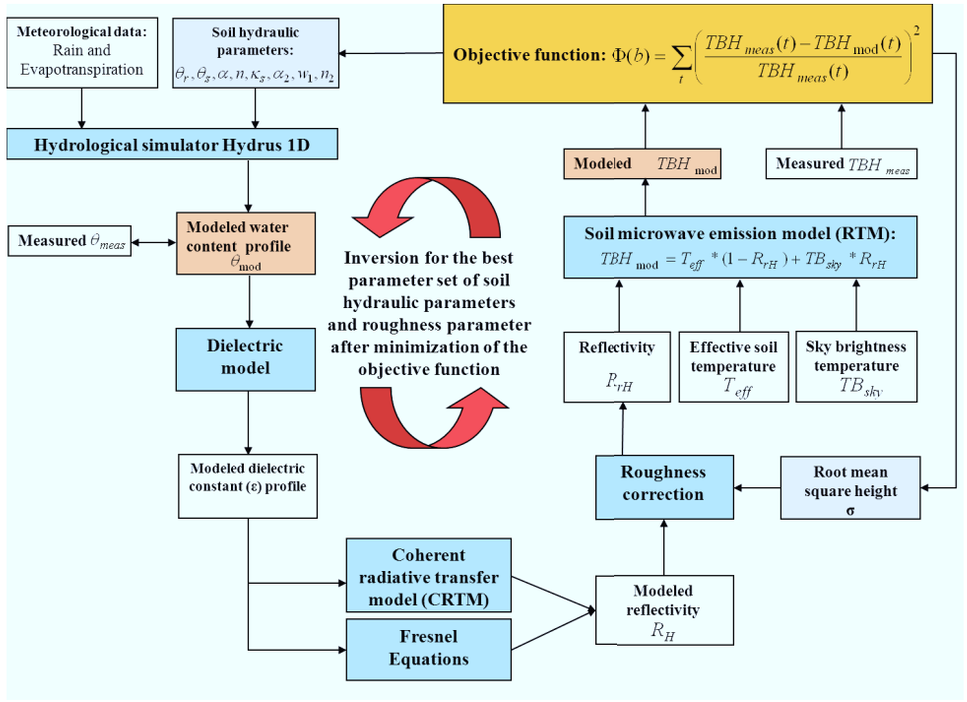

Figure III.3 Flow chart of the coupled inversion procedure. Blue filled boxes represent models, white boxes are input or output variables, gray filled boxes are model parameters that are derived from minimizing the objective function (orange filled box), brown filled boxes are output variables that are compared with measurements.

3.4 Model validation

To validate the inversely derived or retrieved soil hydraulic properties from L-band brightness temperatures, they were compared with hydraulic properties determined on soil samples in the lab. Five cylindrical undisturbed soil samples of 100 cm³ (5.1 cm length and 5 cm i.d.) were taken from the top soil layer (0 - 5 cm depth) on DOY 80, 2011. The soil water retention curve was obtained by equilibrating the samples at different pressure heads after placing them on a sand box with a hanging water table or in pressure cells. The saturated hydraulic conductivity was measured with a permeameter using the constant head method.

The water contents measured by 5TE sensors installed at 2 and 5 cm depth were compared with simulated water contents at these depths by HYDRUS 1D using the optimized hydraulic properties. Because a soil moisture sensor does not measure at a single depth but averages water contents within a certain volume of influence, differences between the simulated water contents at the sensor depth and the actually measured water contents by the sensor can be expected. A detailed analysis and an exact evaluation of the sensor's volume of influence and the distribution of weighting factors that are used to calculate depth weighted averaged water contents would require the calculation of electromagnetic fields generated by the sensor in a heterogeneous medium around the sensor, which is beyond the scope of this study. However, to obtain a first rough estimate of the impact that vertical variations of water contents could have on sensor readings and their comparison with simulated water contents at a single depth, we used a very crude approximation, which is outlined below, of the measurement volume of the 5TE sensor and the distributions of weighting factors within it. Subsequently, these weighting factors were used to calculate depth averaged water contents from simulated water content profiles which were compared with simulated water contents at 2 and 5 cm depth. According to the manufacturer, the volume of influence of the 5TE sensors is 0.3 liters. As a simple approximation, we assumed that the 0.3 liters volume corresponds to a block of 6.5 x 6.5 x 7.2 cm^3 (7.2 cm is an estimate of the radiating length of the sensor) and that the sensor averages the dielectric permittivity within this volume. For the sensor at 2 cm depth, the measurement volume would also include a 1.25 cm thick air layer with air dielectric permittivity $\varepsilon_a = 1$. According to the manufacturer of 5TE sensors, the electromagnetic field produced by the sensor decreases with distance from the sensor electrodes. However, the distribution of the sensor sensitivity to soil dielectric permittivity (water content) within the 0.3 liters volume of influence is not known. In order to mimic the averaging performed by the 5TE sensors we assumed that the weighting factors used for calculating the depth weighted mean of simulated soil moisture contents decrease linearly with distance from the sensor electrodes. We also assumed that the weighting factors at the upper and lower surface of the presumed measurement volume are equal to $1/e = 0.3679$ of its value in the center of the measurement volume.

To relate the sensor readings to soil water contents, soil and depth specific calibration relations were derived as proposed by the manufacturer (Cobos and Chambers, 2010). By using depth specific calibration relations, the impact of the air layer on the measurement by the sensor at 2 cm depth was indirectly accounted for. A box with a surface of 60 x 40 cm^2 and a height of 32 cm was filled with soil taken from the test site. Starting from sieved and air

dried soil ($\theta \sim 0.04$ cm^3 cm^{-3}) the soil was wetted to almost full saturation ($\theta \sim 0.44$ cm^3 cm^{-3}) in seven steps. After every step the soil was again well mixed and homogenized and repacked into the box. For each step, the volumetric water content was determined on at least two 100 cm^3 soil samples. Ten sensors, two at each depth, were installed horizontally in the soil box between 1.8 cm and 12 cm below the soil surface. The raw sensor readings of the 5TE sensors were transformed into relative dielectric permittivity using the given in 5TE Operator's Manual formula: ε_r=RawData/50.

The inversely estimated soil surface roughness parameter σ was compared with the root-mean-square roughness height that was derived from the three-dimensional laser profiler LMP-II, developed by the Institute of Agricultural Engineering, University of Bonn. More information about the measurement system is given in (Sun et al., 2006). For each measurement, 124 parallel profiles of 1500 mm length were sampled with a sampling interval of 2 mm. The distance between parallel profiles was 4 mm. The obtained surface heights were detrended using a 2-D linear fit and the variance of the detrended surface heights in the scanned plot was determined from the variances, σ^2_i and means, μ_i of the detrended surface heights along individual profiles as:

$$\sigma^2 = \frac{1}{N}\sum_{i=1}^{N}\sigma_i^2 + \frac{1}{N-1}\sum_{i=1}^{N}(\mu_i - \mu_\bullet)^2 \qquad \textbf{[III.XV]}$$

where N is the number of profiles and $\mu_\bullet$ is the average of the detrended surface heights in the plot.

The laser profiler measurements were done at the start of the measurement periods. Due to rainfall, the surface roughness decreased over time. To account for this decrease we assumed that the root-mean-square-roughness height decreases exponentially with the accumulated amount of rainfall and could be calculated as (Zobeck and Onstad, 1987)

$$\sigma(P) = \sigma 0.89 * e^{-0.026*P} \qquad \textbf{[III.XVI]}$$

where $\sigma(P)$ is the root-mean-square-roughness height after a certain amount of cumulative precipitation P (cm).

4 Results and discussion

4.1 Measured and modelled brightness temperature

The modeled brightness temperatures were derived based on measurements of soil temperature and on simulations of the water content profiles using fitted DBM or MvG

parameters in combination with either the CRTM or the Fresnel equation with averaged dielectric permittivity in the 0 - 2 cm or in the 0 - 5 cm soil layers.

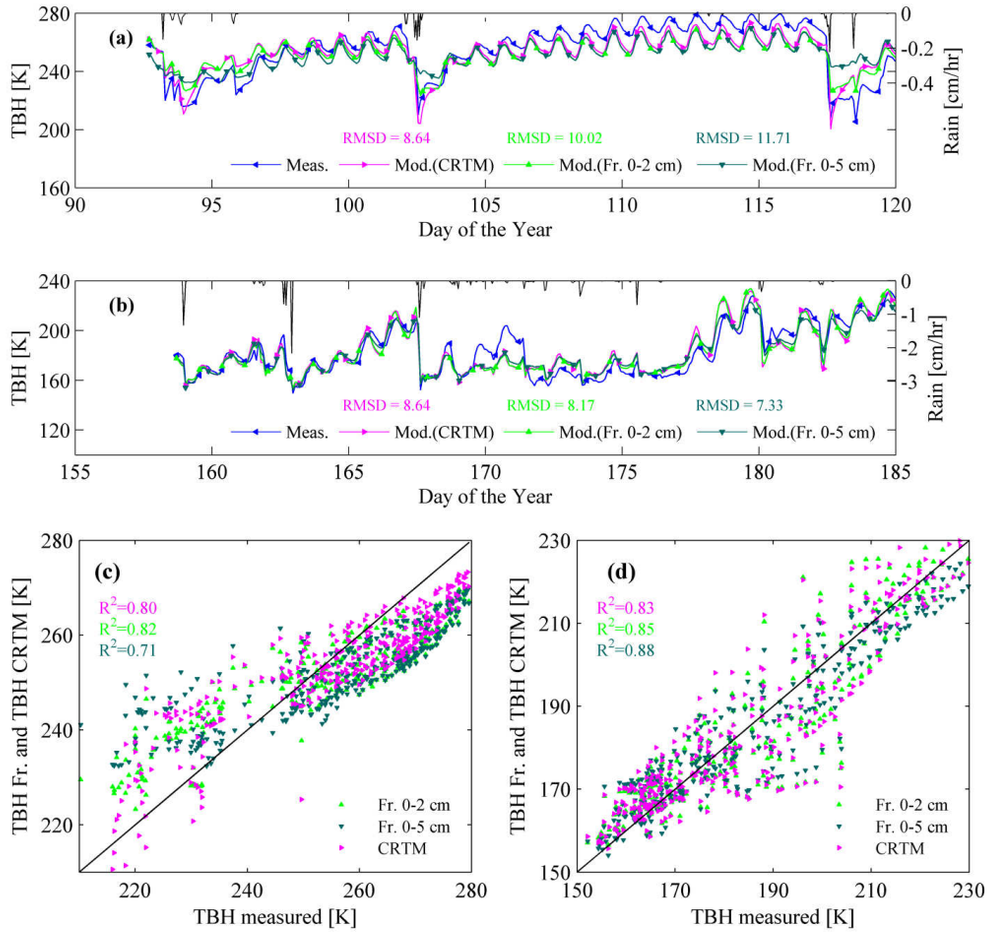

Figure III.4 Time series (a-b) and one-to-one plots (c-d) of measured (blue line) and modeled brightness temperature TBHs from simulated soil moisture profiles using the Durner bi-modal model (DBM) coupled with the coherent radiative transfer model CRTM (magenta lines or dots) or with the Fresnel equation using the mean dielectric permittivity of the 0 - 2 cm surface layer (bright green lines or dots), or of the 0 - 5 cm surface layer (dark green lines or dots) for periods DOY 92-120, 2011 (a and c) and DOY 158-186, 2011 (b and d). Black lines in a-b represent the hourly precipitation rates during the investigated periods.

Figure III.4 (a-d) shows the modeled and the measured brightness temperatures at horizontal polarization (TBH) as well as the measured precipitation. During days without rain, diurnal variations in TBH up to 20 K were mainly caused by diurnal variations in soil temperature. Also diurnal fluctuations of surface soil water content and dielectric permittivity

resulting from diurnal evaporation dynamics contribute to the diurnal TBH dynamics. But, the measured and simulated diurnal water content fluctuations were small (0.01 cm^{-3} cm^{-3}) so that their effect on TBH was small when compared with the fluctuations in TBH due to soil temperature fluctuations. The comparison between the measured and modeled TBH confirm that for wet soil the diurnal TBH fluctuations can be reproduced well using the approximation $T_{eff} \approx T_s$ (2 cm) (e.g. Figure III.4 (b) and Figure III.5).

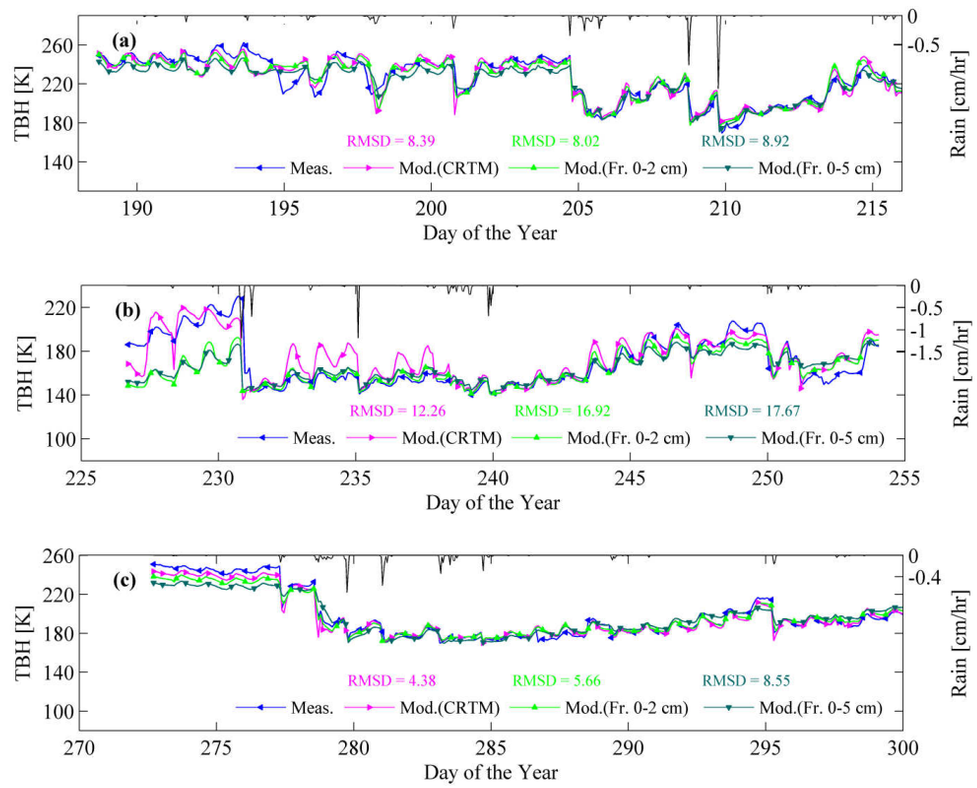

Figure III.5 Time series (a-c) of measured (blue line) and modeled brightness temperature TBHs from simulated soil moisture profiles using the Durner bi-modal model (DBM) coupled with the coherent radiative transfer model CRTM (magenta lines), or with the Fresnel equation using the mean dielectric permittivity of the 0 - 2 cm surface layer (bright green lines), or of the 0 - 5 cm surface layer (dark green lines) or for periods 2011: DOY 186-214 (a), 2011: DOY 226-254 (b) and 2009: DOY 272-300. Black lines represent the hourly precipitation rates during the investigated periods.

Contrary, for dry soil (e.g. Figure III.4 (a), DOY 105-116), the modeled diurnal TBH variations are bigger than the measured ones. This indicates that diurnal variation of the soil temperature at 2 cm depth is larger than variation of the effective temperature which is in agreement with the fact that the effective sampling depth of the radiometer increases when the

soil gets drier. Several rain events occurred during the mostly dry period (DOY 92-120), which were immediately observed by the radiometer. The measured TBH decreased with more than 50 K just after the main rain events and increased subsequently again due to drying out of the soil surface. After the rain events (e.g. DOY 103 and 117) the TBH values modeled with Fresnel 0 – 5 cm were not able to reach the measured TBH and were considerably different from the modeled TBH using Fresnel 0 – 2 cm or using CRTM. On DOY 117 differences of 43 K between CRTM and Fresnel 0 – 5 cm, of 26.2 K between CRTM and Fresnel 0 – 2 cm, and of 18.8 K between Fresnel 0 – 2 cm and Fresnel 0 – 5 cm were obtained. After rain, the upper part of the soil surface layer was wetted whereas the deeper part was still dry. This led to different values of the calculated mean dielectric permittivity used in the Fresnel equation (Eq. [III.XIII]), depending on the thickness of the surface layer that was considered. During the drying phase after the second rain event (DOY 103), all models underestimated the TBH. This indicates that the models overestimated the surface soil moisture and hence the dielectric permittivity during this evaporation period (see also Figure III.14).

The total amount of rain during the wet period (DOY 158-186) presented in Figure III.4 (b) was more than a factor 10 larger than during the dry period (see Table III.2). During the dry period, the rain events can be characterized as light rain with precipitation rates up to 0.25 cm/hr whereas during the wet period most of the rain events can be classified as heavy rain with precipitation rates between 1 and 2 cm/hr. The root mean square deviation (RMSD) values between measured and modeled TBH given in Figure III.6 differed between the periods and the models.

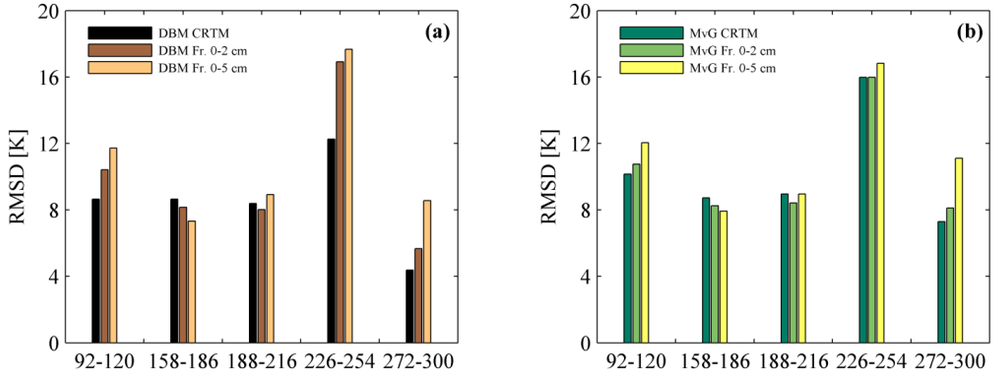

Figure III.6 RMSDs between measured and modeled L-band brightness temperatures (TBH) for different combinations of radiative transfer models: Fresnel or CRTM with soil hydraulic functions: (a) Durner bi-modal model (DBM) or (b) Mualem van Genuchten (MvG).

When considering all periods and both hydraulic soil functions (MvG and DBM) the RMSDs varied from 4.4 K for the period DOY 272-300, 2009 with DBM and CRTM up to 16.9 K for the period DOY 226-254, 2011 with DBM and Fresnel 0 – 2 cm and 17.7 K with Fresnel 0 – 5 cm (see Figure III.6). In general, RMSDs are fairly similar for the different soil hydraulic functions (DBM and MvG). For two of the wet periods (DOY 158-186, 2011 and DOY 188-216, 2011) the RMSDs were very similar for all model combinations and varied between 8.0 and 8.9 K. During these wet periods, the simulated soil moisture contents were apparently relatively uniform within the surface soil layer so that both the Fresnel 0 – 2 cm and Fresnel 0 – 5 cm models, which do not resolve vertical variations of relative dielectric permittivity or soil moisture with depth, gave similar results as the CRTM model. It must be noted that this behaviour is closely linked to the hydraulic properties of the fine textured soil with a relatively large water holding capacity. In a coarse textured soil, the soil surface layer may lose rapidly a large amount of water and dry out considerable due to rapid drainage so that even during relatively wet periods, large vertical gradients in water content may occur after a rainfall event. For the other periods, the DBM model coupled with the CRTM resulted in the smallest RMSDs. They were comparable with the results from Fresnel 0 – 2 cm but smaller than the RMSDs obtained with Fresnel 0 – 5 cm. In these periods, vertical variations of soil moisture and dielectric permittivity in the top soil layer, e.g. after a rainfall event on a dry soil, that can be accounted for by the CRTM apparently influenced the calculated TBHs. Yet, using a sufficiently shallow surface soil layer for calculating average dielectric permittivity or moisture content, i.e. Fresnel 0 – 2 cm, may still be a viable alternative to reproduce the dynamics of measured TBHs. In addition, the DBM model has more flexibility than the MvG model to represent the soil hydraulic properties and consequently simulate the dynamics of the soil moisture contents and match the simulated TBHs to the measured ones.

4.2 Surface roughness correction factor

The root-mean-square-roughness height that was derived from laser profiler measurements varied between 1.41 and 2.19 cm for the investigated periods (Table III.3). The roughness parameter σ of the model of (Choudhury et al., 1979) (Eq. [III.XIV]) that was retrieved from the brightness temperatures using inverse modeling, did, for a given measurement period, not vary a lot between the different radiative transfer and soil hydraulic property models and ranged from 1.01 to 2.52 cm (Table III.3). Of note is that, except for the dry period DOY 92-120, 2011, σ retrieved using Fresnel 0 – 5 cm was slightly smaller than for the case that Fresnel 0 – 2 cm was used. The range of retrieved σ is similar to the range of

measured (Eq. [III.XV]) and calculated σ's (Eq. [III.XVI]), which represent the roughness at the beginning and the end of the L-band measurement period, respectively. But, the variation of measured σ between different periods is not reproduced by the retrieved ones.

Table III.3 Dates of mechanical field preparations and of laser profiler measurements, root-mean-square-roughness height σ: measured with laser profiler, calculated from the amount of rain since the measurement day until the end of the measurement period, σ(P) and inverted from measured brightness temperatures for different measurement periods. Values between parentheses are the minimal and maximal σ_i along individual profiles.

Period	Prep.	Meas.		σ (cm)						
	DOY	DOY	Measured	σ(P)	Inverted					
					CRTM DBM	Fresnel 0 - 2 cm DBM	Fresnel 0 - 5cm DBM	CRTM MvG	Fresnel 0 - 2 cm MvG	Fresnel 0- 5 cm MvG
92-120	74	96	1.41 (0.97-1.79)	1.20	2.50	2.38	2.52	2.37	2.35	2.39
158-186	147	158	2.19 (1.97-2.48)	1.37	1.28	1.24	1.19	1.24	1.25	1.13
188-216	147	186	1.60 (1.33-1.86)	1.20	1.65	1.62	1.50	1.59	1.58	1.41
226-254	223	224	1.50 (1.05-1.82)	1.00	1.04	1.08	1.04	1.02	1.02	1.01

The retrieved roughness parameter was larger for the period DOY 92-120, 2011 and smaller for the period DOY 158-186, 2011 than the measured roughness parameter. It should be noted that for the period DOY 92-120, 2011, also the retrieved hydraulic functions for the DBM and MvG models deviate considerably from the other periods and from the lab derived curves (see further and Figure III.7). The difference between the directly measured and inversely estimated roughness parameter σ could be attributed to: a) the difference between the small 1.5 x 0.5 m footprint of the laser profiler and the much larger footprint of the radiometer combined with the large spatial variability of the surface roughness of tilled soil as is evidenced by the variability of σ derived from individual profiles (see values in parentheses in Table III.3), b) the impact of the simultaneous inverse estimation of several parameters, i.e. the hydraulic parameters and σ, which due to multicolinearity may increase the uncertainty of individual parameter estimates, c) temporal variability of the surface roughness over time (due to rain and erosion) vs. constant surface roughness over time in the inversion routine. Finally, it should be noticed that the roughness correction model is a semi-empirical model so that the fitted roughness parameter is not necessarily directly comparable with a direct estimation of this parameter from measurements of the soil surface roughness. But, despite the problems listed above, our results show that plausible estimates of the soil surface roughness parameter σ, i.e. in the same order of magnitude as direct measurements, are obtained when it is estimated together with soil hydraulic parameters from radiometer measurements using a

coupled inversion approach. In order to validate this finding, further studies in which the surface roughness is varied more than in this study have to be carried out.

4.3 Water retention and hydraulic conductivity functions

Figure III.7 presents water retention (a and c) and hydraulic conductivity curves (b and d) for the DBM (a and b) and the MvG (c and d) models that were derived for each of the investigated periods from the measured brightness temperatures using the coupled inversion scheme with the CRTM radiative transfer model. Similar graphs obtained with the Fresnel 0 – 2 cm layer model are given in Figure III.8. The black open circles (a and c) show the mean water contents of five undisturbed soil samples and the bars show the maximum and the minimum at each pressure step. The black lines are the fitted water retention curves to the lab data. For the hydraulic conductivity curve, the measured saturated conductivity of the soil samples and the Mualem model was used to derive the conductivity curve from the water retention curve. In Table III.4 and Table III.5, the parameters of the DBM and of the MvG hydraulic functions that were derived from the lab data and from the inversion of the brightness temperatures in the different periods are given.

The lab derived water retention data suggest a bi-modal pore size distribution (w_2 is clearly larger than 0 and α_2 is considerably larger than α_1, see Table III.4). This behavior could also be observed from the retrieved parameters from inversion of L-band brightness temperatures (Table III.4). The variation of the hydraulic parameters and the retrieved retention and conductivity curves, which were obtained from the different time periods, reflects both uncertainty and temporal variation of the hydraulic properties. The different meteorological conditions and consequently different soil hydrological states during the different periods constrain the hydraulic functions in different ranges of pressure heads, water contents, and conductivities, which also influences the retrieved hydraulic parameters. Especially for the dry period (DOY 92-120, 2011 brown line in Figure III.7), when the soil was drier and pressure heads lower than in the other periods, the derived hydraulic curves for the DBM and MvG models deviate considerably from the other periods and from the lab derived curves. The ranges of the retrieved parameters for the different periods are smaller than the initial parameter ranges that were considered as possible parameter values in the optimization algorithm. This indicates that the L-band brightness temperatures contain information to constrain hydraulic parameters. The Fresnel and CRTM radiative transfer

models give similar ranges of retrieved parameters so that the choice of the radiative transfer model does not have a notable effect on the retrieved parameters.

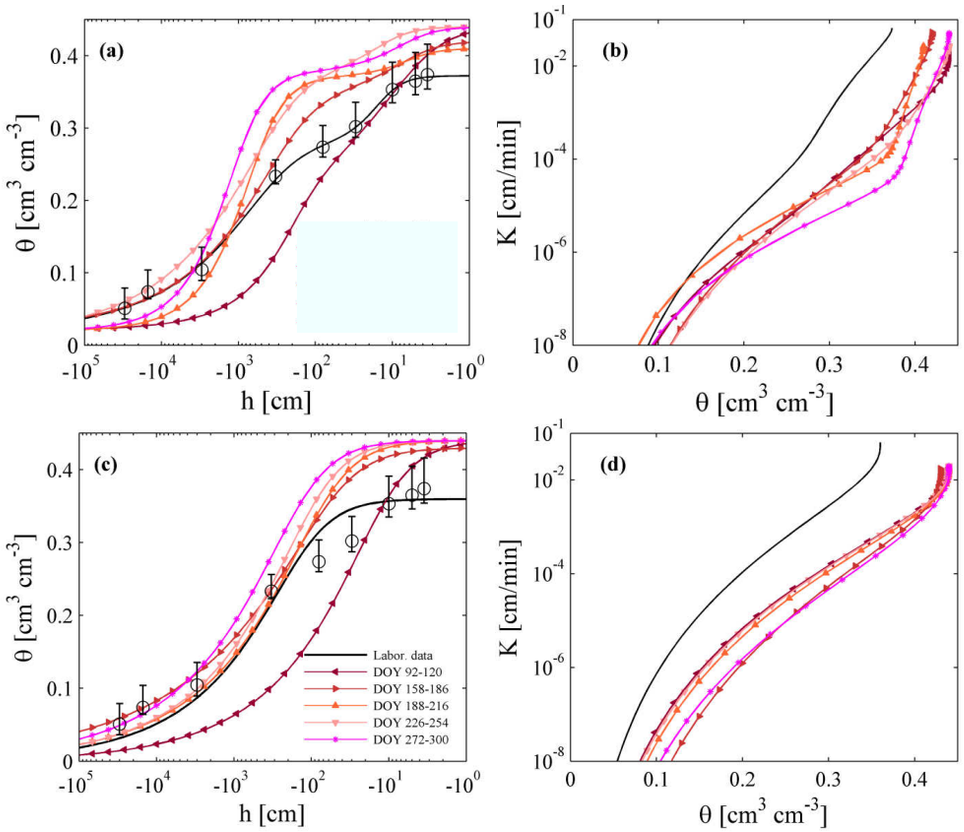

Figure III.7 Volumetric water content θ as a function of pressure head, h, (a, c) and hydraulic conductivity, K, as function of the volumetric water content (b, d) for the Durner bi-modal model (a, b) and the Mualem van Genuchten model (c, d). The parameters of the curves were retrieved from time series of the brightness temperatures using the coherent radiative transfer model (CRTM) for different time periods. The black lines represent water retention and conductivity curves that are derived from lab measurements: open circles are mean values and the bars represent the ranges. For the hydraulic conductivity curve, only the saturated hydraulic conductivity was measured.

When comparing the lab derived and retrieved parameters in Table III.4 and Table III.5, there are some differences for the saturated water content, θ_s, saturated conductivity, K_s, the shape parameter, α_2, and the volume fraction, w_2, of the 'macropore' domain. The saturated soil moisture values θ_s that were retrieved from L-band measurements varied for all periods between θ_s = 0.41 and 0.44 $cm^3\ cm^{-3}$, and were higher than θ_s, estimated from the lab data (θ_s = 0.373 $cm^3\ cm^{-3}$). The lower estimates obtained from the lab data could be explained by the

extrapolation of the water retention curve from the point with the highest matric head to the water content for a matric head of 0 cm.

Table III.4 Parameters of the Durner bi-modal soil hydraulic functions derived from lab measurements on soil cores and retrieved for the different measurement periods from measured brightness temperatures using coupled inversion with the CRTM or with Fresnel 0 – 2 cm. The last two rows show the ranges of inverted parameter values obtained for the different measurement periods.

		θ_r ($cm^3\ cm^{-3}$)	θ_s ($cm^3\ cm^{-3}$)	α_1 (1/cm)	n_1 -	K_s (cm/min)	λ -	w_2 -	α_2 (1/cm)	n_2 -
		Laboratory data								
		0.01	0.373	0.0032	1.44	0.066	0.5	0.26	0.0759	2.64
Model	Period DOY	Inverted from TBH								
	Initial Range -	0-0.05	0.30 – 0.45	(1-100)10^{-3}	1.1 – 2	(20 – 200)10^{-3}	0.5	0.1-0.6	(10-600)10^{-3}	1 - 4
CRTM	92-120	0.02	0.44	0.0066	1.98	0.020	0.5	0.6	0.22	1.47
Fresnel	92-120	0	0.44	0.0048	1.98	0.020	0.5	0.6	0.33	1.46
CRTM	158-186	0.02	0.42	0.005	1.46	0.054	0.5	0.17	0.2	1.92
Fresnel	158-186	0.01	0.42	0.0051	1.72	0.0513	0.5	0.14	0.34	2.33
CRTM	188-216	0.02	0.41	0.0019	1.98	0.027	0.5	0.1	0.195	2.3
Fresnel	188-216	0.02	0.44	0.0039	1.88	0.027	0.5	0.22	0.16	2.7
CRTM	226-254	0.01	0.44	0.0034	1.43	0.0277	0.5	0.14	0.09	2.12
Fresnel	226-254	0.01	0.43	0.0019	1.43	0.0427	0.5	0.12	0.09	2.06
CRTM	272-300*	0.02	0.44	0.0011	1.99	0.052	0.5	0.15	0.178	1.98
Fresnel	272-300*	0.02	0.43	0.0012	1.99	0.051	0.5	0.12	0.27	1.99
CRTM	Range	0.01-0.02	0.41-0.44	0.0011-0.0066	1.43-1.99	0.02-0.054	0.5	0.1-0.6	0.09-0.22	1.5-2.3
Fresnel	Range	0-0.02	0.42-0.44	0.0012-0.0051	1.43-1.99	0.02-0.053	0.5	0.12-0.6	0.09-0.34	1.8-2.7

*data from 2009

The highest pressure head that was considered for the water retention curves was on average -3.5 cm, i.e. the equilibrium pressure head in the middle of the soil sample when the water level was 1 cm below the bottom of the soil sample. At this pressure head, the larger interaggregate pores of the tilled soil were drained already so that the saturated water content may be larger than the measured water content at -3.5 cm. From the measured dry bulk density of the soil cores (1.49 gr cm^{-3}), a porosity of 0.44 was calculated, which is also considerably larger than the measured water content at -3.5 cm but corresponds better with θ_s retrieved from L-band measurements.

Table III.5 Parameters of the Mualem van Genuchten soil hydraulic functions derived from lab measurements on soil cores and retrieved for the different measurement periods from measured brightness temperatures using coupled inversion with the CRTM or with Fresnel 0 – 2 cm. The first row shows the ranges of parameter values that were used for the inversion, last two rows show the ranges of inverted parameter values obtained for the different measurement periods.

		θ_r ($cm^3\ cm^{-3}$)	θ_s ($cm^3\ cm^{-3}$)	α (1/cm)	n -	K_s (cm/min)	λ -
		Laboratory data					
		0.00	0.36	0.0083	1.44	0.066	0.5
Model	Period DOY	Inverted from TBH					
	Initial Range	0-0.05	0.30 0.45	$(1\text{-}100)10^{-3}$	1.1- 2	$(2\text{-}200)10^{-3}$	0.5
CRTM	92-120	0.02	0.44	0.091	1.43	0.0204	0.5
Fresnel	92-120	0,02	0.44	0.091	1.42	0.0200	0.5
CRTM	158-186	0.01	0.43	0.02	1.31	0.0204	0.5
Fresnel	158-186	0.02	0.43	0.024	1.33	0.0201	0.5
CRTM	188-216	0.01	0.44	0.0158	1.4	0.0201	0.5
Fresnel	188-216	0.01	0.44	0.04	1.44	0.0201	0.5
CRTM	226-254	0.02	0.44	0.0115	1.42	0.0209	0.5
Fresnel	226-254	0.02	0.44	0.012	1.42	0.0204	0.5
CRTM	272-300*	0.0	0.44	0.0079	1.4	0.0206	0.5
Fresnel	272-300*	0.0	0.44	0.0079	1.38	0.0206	0.5
CRTM	Range	0-0.02	0.43-0.44	0.0079-0.091	1.31-1.42	0.0201-0.0209	0.5
Fresnel	Range	0-0.02	0.43-0.44	0.0079-0.091	1.33-1.44	0.02-0.0206	0.5

*data from 2009

The fact that water contents in the lab samples were not measured for pressure heads larger than -3.5 cm may explain why the α_2 parameter that was derived from the lab data was smaller than the α_2 parameter that was retrieved from L-band brightness temperatures. The inverse of α_2 is related to an effective pore size of the macropore region, of which apparently only the smaller pores were filled with water at a pressure head of -3.5 cm in the lab samples. In a similar vein, the volume fraction of the macropore domain, w_2 that was derived from brightness temperatures was in most cases larger than the w_2 derived from lab measurements.

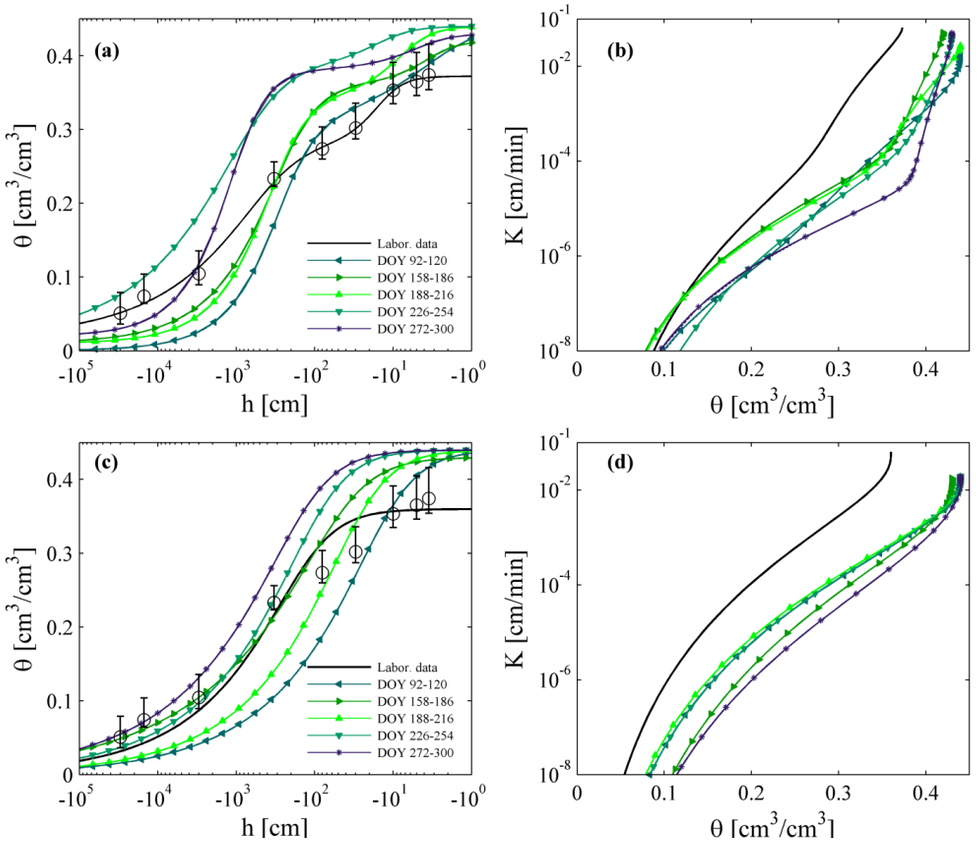

Figure III.8 Volumetric water content θ as a function of pressure head, h, (a, c) and hydraulic conductivity, K, as function of the volumetric water content (b, d) for the Durner bi-modal model (a, b) and the Mualem van Genuchten model (c, d). The parameters of the curves were retrieved for different time periods from time series of the brightness temperatures using the Fresnel equation with depth averaged dielectric permittivity in the 0 - 2 cm layer. The black lines represent water retention and conductivity curves that are derived from lab measurements: open circles are mean values and the bars represent the ranges. For the hydraulic conductivity curve, only the saturated hydraulic conductivity was measured.

The retrieved saturated hydraulic conductivity was smaller than the lab measured saturated conductivity, especially for the uni-modal MvG model. The saturated conductivity that is measured on 5.1 cm long soil columns may be very large when large pores that connect the in- and outflow side of the column are present. In the field soil, the water flux through these pores may be much smaller once they are completely filled with water and water can only leave these pores by infiltrating into the soil matrix. Therefore, using the measured saturated hydraulic conductivity on short soil columns together with the Mualem model and a

uni-modal pore size distribution model (van Genuchten water retention curve) may lead to a strong overestimation of the unsaturated hydraulic conductivity of structured soils (e.g. Schaap and Leij, 2000; Weynants et al., 2009). The retrieved parameters were derived by fitting the coupled model to time series of brightness temperatures and the corresponding moisture contents represented most of the times unsaturated soil conditions. As a consequence, the retrieved parameters represent the hydraulic properties under unsaturated conditions. Because of the impact of interaggregate pores on the measured saturated hydraulic conductivity and on the retrieved saturated water content, which was larger than the saturated water content measured in the lab, the retrieved hydraulic conductivity for given water content was considerably lower than the hydraulic conductivity that was derived from the lab parameters. The bi-modal pore size distribution model has the flexibility to represent the impact of interaggregate pores or macropores on the hydraulic properties. It should be noted that for all except the dry period, (DOY 92-120, 2011), the DBM model predicted higher hydraulic conductivities close to saturation, i.e. for $h > -1$ cm, than the MvG model whereas for lower pressure heads, i.e. $h < -10$ cm, the hydraulic conductivities obtained with the DBM model were generally smaller than the ones derived using the MvG model (see Figure III.9).

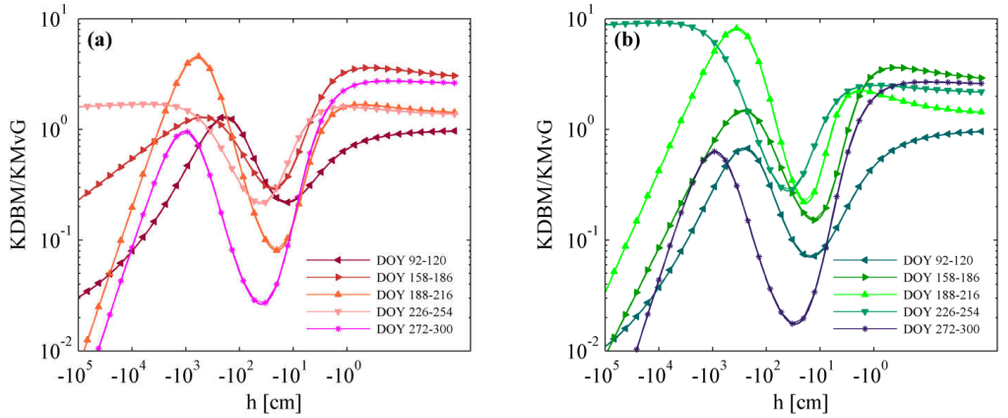

Figure III.9 Ratio of the Durner bi-modal to the Mualem van Genuchten unsaturated hydraulic conductivities KDBM/KMvG as a function of pressure head, h, which were retrieved for the different time periods from brightness temperatures (TBH) using the coherent radiative transfer model (a) or the Fresnel equation (b).

4.4 Site- and depth- specific calibration of soil moisture sensors

The relationship between relative dielectric permittivity ε_r obtained from the 5TE sensors and the corresponding volumetric soil moisture is presented in Figure III.10 for two sensor

depths: 2 and 5 cm. For sensors that were installed deeper in the calibration box, the relationship did not differ substantially from the sensor at 5 cm depth (results not shown), as was expected since the soil was uniformly packed in the box, the water content did not vary with depth, and measurement volume of the deeper installed sensors was completely within the calibration box and did not include an additional air layer. The data points were fitted by a quadratic relationship, which was found also appropriate for other soil types (Cobos and Chambers, 2010), using a least squares method. Also shown in Figure III.10 is the Topp equation (Topp et al., 1980) which is used by the software, provided by the manufacturer, to convert the measured dielectric permittivity to volumetric soil moisture.

The relation between sensor derived dielectric permittivity and water content was clearly different for the sensors installed at 2 and 5 cm depth. For the same soil water content, the dielectric permittivity that was derived by the sensor at 2 cm depth was lower than the dielectric permittivity derived from the sensor at 5 cm depth. This is consistent with the anticipated effect of the low dielectric permittivity of the air layer above the soil surface on the dielectric permittivity measured by a sensor installed close to the soil surface. The implication of this different relationship for 5TE sensors installed at 2 cm depth can be an underestimation of the soil moisture content of up to 0.05 cm^3 cm^{-3} when a relationship for sensors that are installed deeper is used.

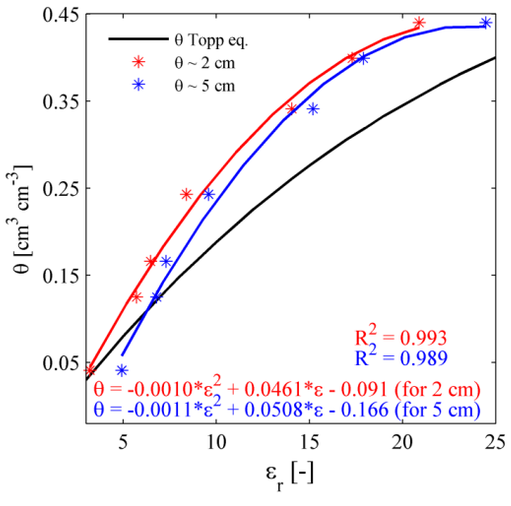

Figure III.10 Relation between gravimetrically measured volumetric moisture content, θ, and relative dielectric permittivity, ε_r, measured by DECAGON 5TE sensors at 2 cm (red stars) and 5 cm (blue stars) below the soil surface. The colored lines are fits of a quadratic equation through the measurement points and the black line represents the Topp equation (Topp et al., 1980), which is used by the sensors to calculate soil moisture.

The relation between sensor derived dielectric permittivity and soil moisture content also deviated considerably from the Topp equation. This deviation (e.g. for $\varepsilon_r = 15$ the deviation is more than 0.1 $cm^3\ cm^{-3}$) was found to be considerably larger than the accuracy of the soil moisture measurement that is suggested by the manufacturer to be $\pm$ 0.03 $cm^3\ cm^{-3}$. We do not understand the causes for this deviation well but it should be noted that this deviation does not necessarily imply that Topp's equation is not valid for this soil. It could also indicate that the sensor derived dielectric permittivity deviates from the bulk soil dielectric permittivity due to disturbances of the soil close to the sensor, such as air gaps or local soil compaction around the sensor.

4.5 Comparison between retrieved and in situ measured soil moisture

Figure III.11 shows measured and retrieved soil moistures using the DBM in combination with the CRTM, Fresnel 0 – 2 cm, or Fresnel 0 – 5 cm models at 2 and 5 cm depth for the two considered observation periods. Similar figures for other time periods are presented in Figure III.12 and Figure III.13.

Overall, a good agreement between retrieved and measured soil moisture contents was obtained. However, the changes of retrieved and sensor measured water contents after a rainfall event differed considerably. After main rain events the measured TBH values decreased with more than 50 K (e.g. at DOY 93, 102.5 and 117.41, as well as DOY 162.6, 167.6 and 180, see Figure III.4). The maximum changes in the measured soil water content values after rain events were 0.04 $cm^3\ cm^{-3}$ at 2 cm and 0.024 $cm^3\ cm^{-3}$ at 5 cm for the dry period and 0.07 $cm^3\ cm^{-3}$ at 2 cm and 0.056 $cm^3\ cm^{-3}$ at 5 cm for the wet period. The maximum changes in the retrieved soil water content values using CRTM after rain events were considerably larger than the changes measured by the soil sensors. The retrieved soil moisture changes were 0.14 $cm^3\ cm^{-3}$ at 2 cm and 0.009 $cm^3\ cm^{-3}$ at 5 cm for the dry period and 0.21 $cm^3\ cm^{-3}$ at 2 cm and 0.12 $cm^3\ cm^{-3}$ at 5 cm for the wet period, respectively.

The soil hydrological model simulates with high vertical resolution the temporal changes of water content and consequently dielectric permittivity distributions within the top soil layer during and after a rainfall event and their impact on the brightness temperature is modeled using the CRTM radiative transfer model. This implies that the difference in dynamics of retrieved and sensor measured soil moisture contents after a rainfall event cannot be attributed to neglecting vertical variations of soil moisture and dielectric permittivity in the top soil layer in the retrieval algorithm.

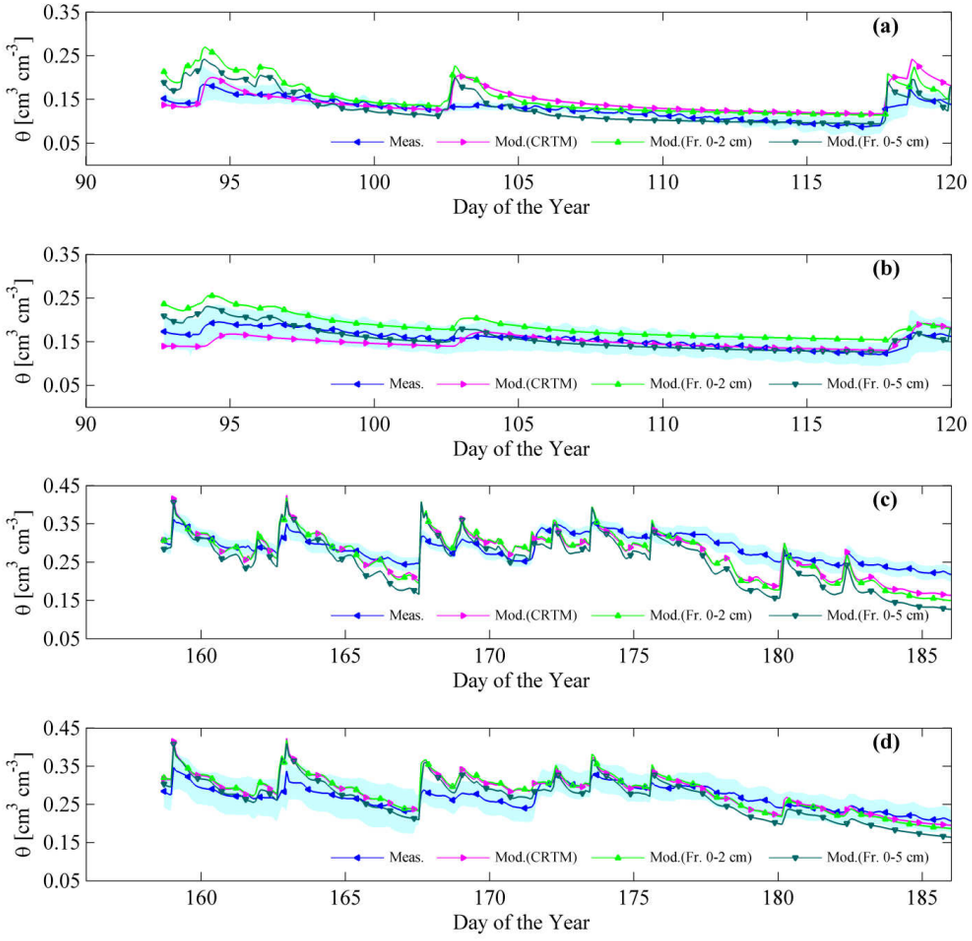

Figure III.11 Time series for two periods: DOY 92-120, 2011 (a, b) and DOY 158-186, 2011 (c, d), and two depths: 2 cm (a, c) and 5 cm (b, d) of volumetric soil moisture contents, θ, that are obtained from sensor readings using a site and depth specific calibration (blue lines) and retrieved from L-band brightness temperatures using the Durner bi-modal hydraulic model coupled with the CRTM (magenta lines), or with the Fresnel equation using the mean dielectric permittivity of the 0 - 2 cm layer (bright green line) or of the 0 - 5 cm layer (dark green line). The transparent blue bands around the sensor readings represent the 95% confidence intervals of the mean of the sensor readings at a certain time and depth.

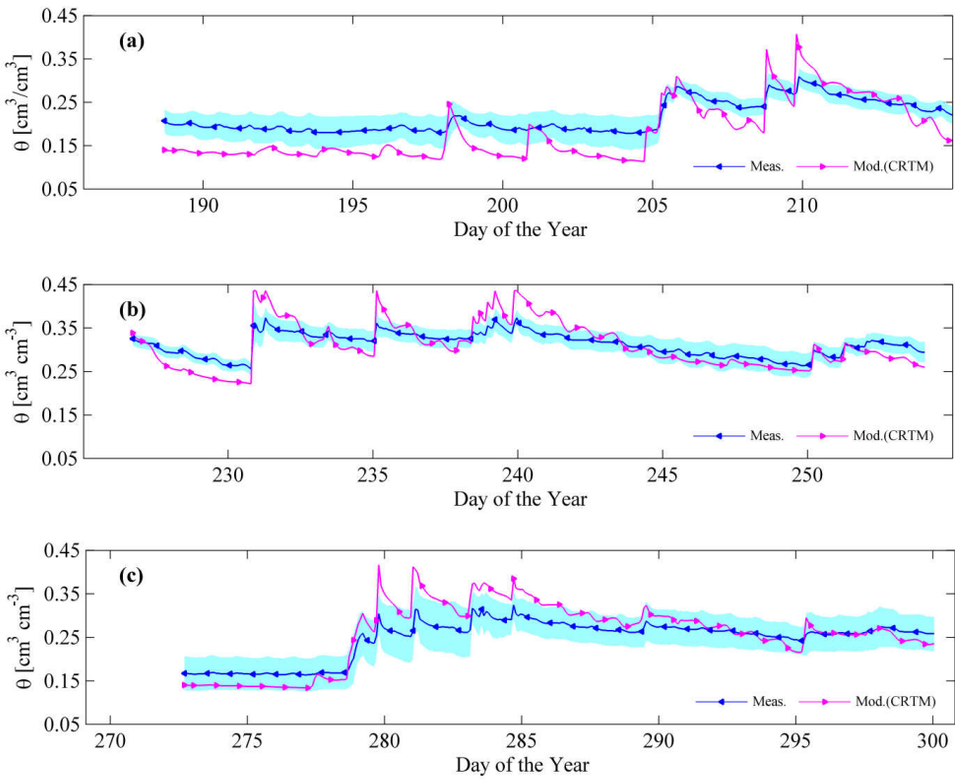

Figure III.12 Time series for 2011: DOY 188-216 (a), 2011: DOY 226-254 (b), and 2009: DOY 272-300 (c) of volumetric soil moisture contents, θ, at 2 cm depth that are obtained from sensor readings using a site and depth specific calibration (blue lines) and from brightness temperatures using the Durner bi-modal hydraulic model and the CRTM (magenta lines) model. The transparent blue bands around the sensor readings represent the 95% confidence intervals of the mean of the sensor readings at a certain time and depth.

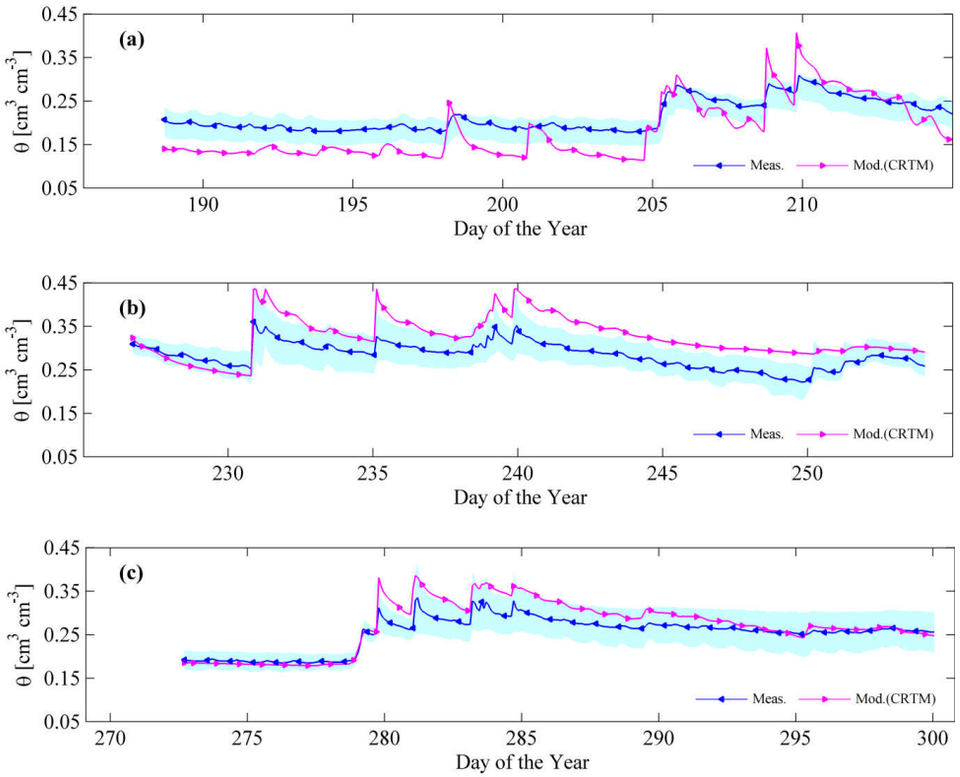

Figure III.13 Time series for periods 2011: DOY 188-216 (a), 2011: DOY 226-254 (b), and 2009: DOY 272-300 (c) of volumetric soil moisture contents, θ, at 5 cm depth that are obtained from sensor readings using a site and depth specific calibration (blue lines) and from brightness temperatures using the Durner bi-modal hydraulic model and the CRTM (magenta lines) model. The transparent blue bands around the sensor readings represent the 95% confidence intervals of the mean of the sensor readings at a certain time and depth.

In Figure III.14 (a - d), the RMSDs between the in situ measured soil moisture using the depth and site-specific calibration and moisture contents retrieved from brightness temperatures using different radiative transfer models (CRTM, Fresnel 0 – 2 cm, and Fresnel 0 – 5 cm) and different soil hydraulic functions (DBM and MvG) are shown. The RMSD values with CRTM were, for both soil hydraulic properties models: DBM and MvG, mostly slightly lower than the values obtained with Fresnel 0 – 2 cm and Fresnel 0 – 5 cm (except for the dry period DOY 92-120, 2011 at 2 cm). However, the RMSD values estimated with Fresnel 0 – 5 cm were always higher than the other two (except wet period DOY 226-254, 2011 where all values were identical). The similar RMSDs between observed and retrieved soil moisture contents for the CRTM and Fresnel 0 – 2 cm suggested that simulated vertical variations of soil water content in the upper 2 cm soil layer were not so important for the brightness temperatures.

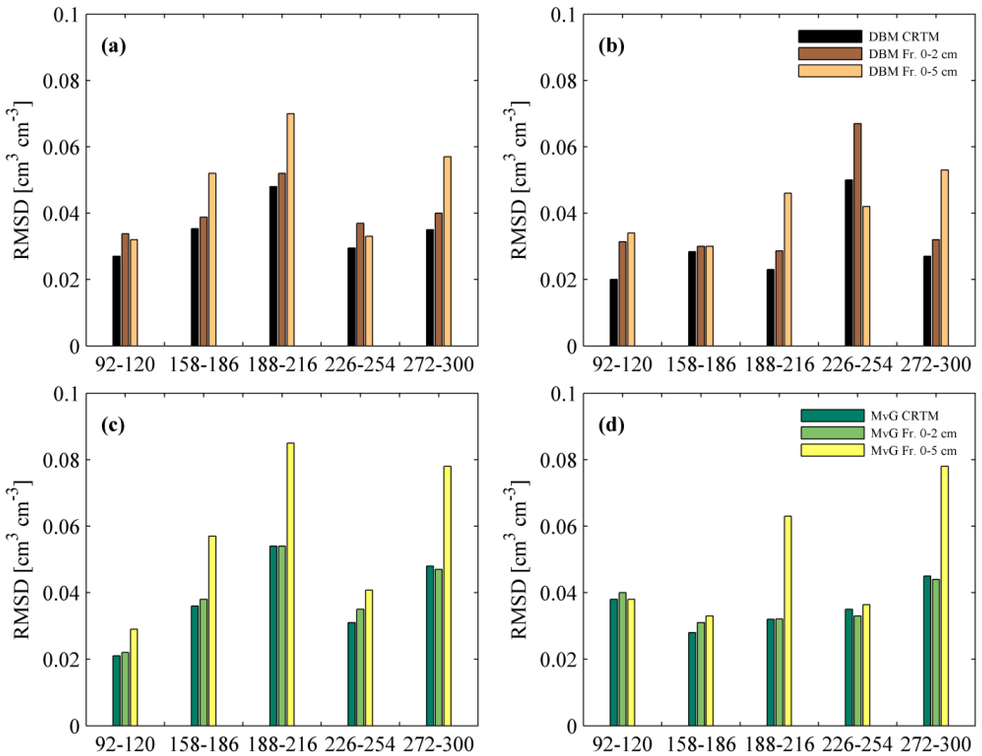

Figure III.14 RMSDs between measured soil moisture contents using a site and depth specific calibration, and retrieved soil moisture contents at 2 cm (a, c) and 5 cm (b, d) depth for all investigated periods (x-axis in DOY) and for different combinations of radiative transfer models: CRTM or Fresnel equation with depth averaged dielectric permittivity in the 0 - 2 cm or 0 - 5 cm surface layer; and different soil hydraulic functions: (a, b) Durner bi-modal model (DBM); or (c, d) Mualem van Genuchten (MvG).

Figure III.15 shows the retrieved water contents when the MvG or the DBM hydraulic functions are used together with the CRTM radiative transfer model.

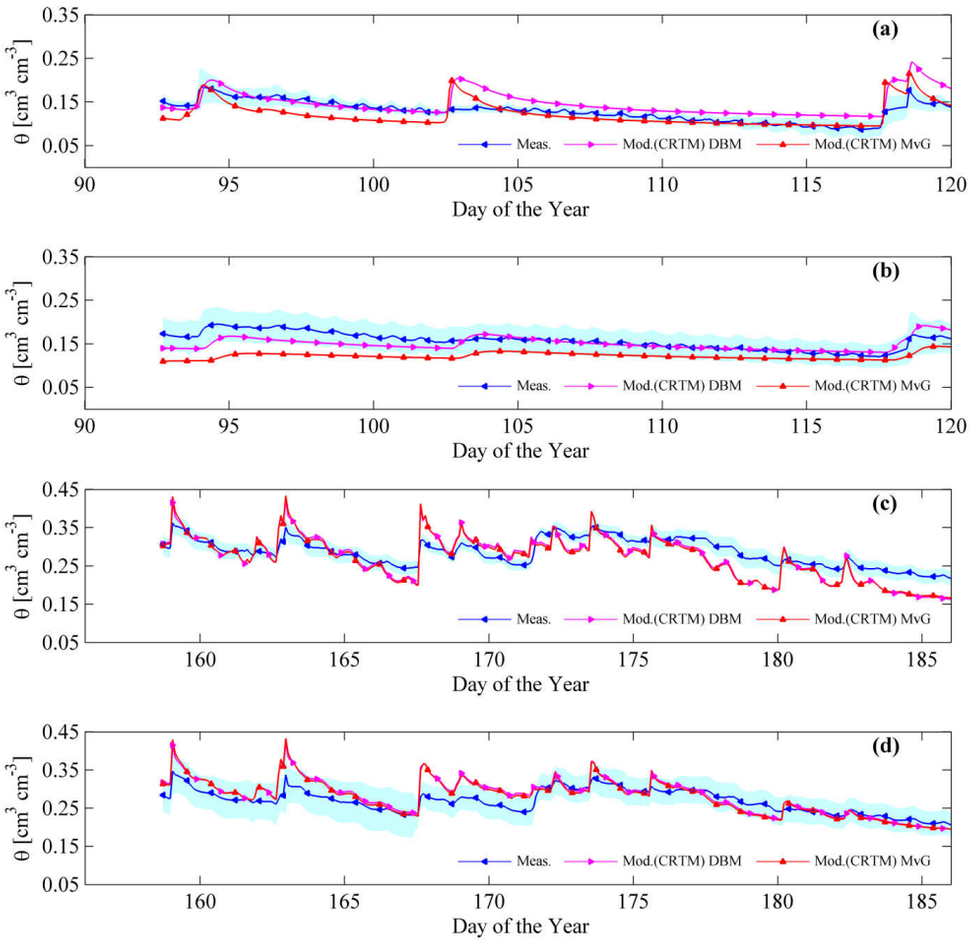

Figure III.15 Time series for two periods: DOY 92-120, 2011 (a, b) and DOY 158-186, 2011 (c, d), and two depths: 2 cm (a, c) and 5 cm (b, d) of volumetric soil moisture contents, θ, that are obtained from sensor readings using a site and depth specific calibration (blue lines) and retrieved from brightness temperatures using the CRTM and the Durner bi-modal (magenta line) or the Mualem van Genuchten model (red line). The transparent blue bands represent the 95% confidence intervals of the mean of measured moisture contents at a certain time and depth.

When comparing the RMSDs obtained for the DBM and MvG hydraulic functions (see Figure III.14), the DBM leads in general to smaller RMSDs than the MvG. The smaller RMSDs between observed and simulated brightness temperatures for the CRTM and DBM model combination (Figure III.6) were apparently transferred into smaller RMSDs between

retrieved and measured soil moisture contents. However, it must be noted that the effects were small and not always present.

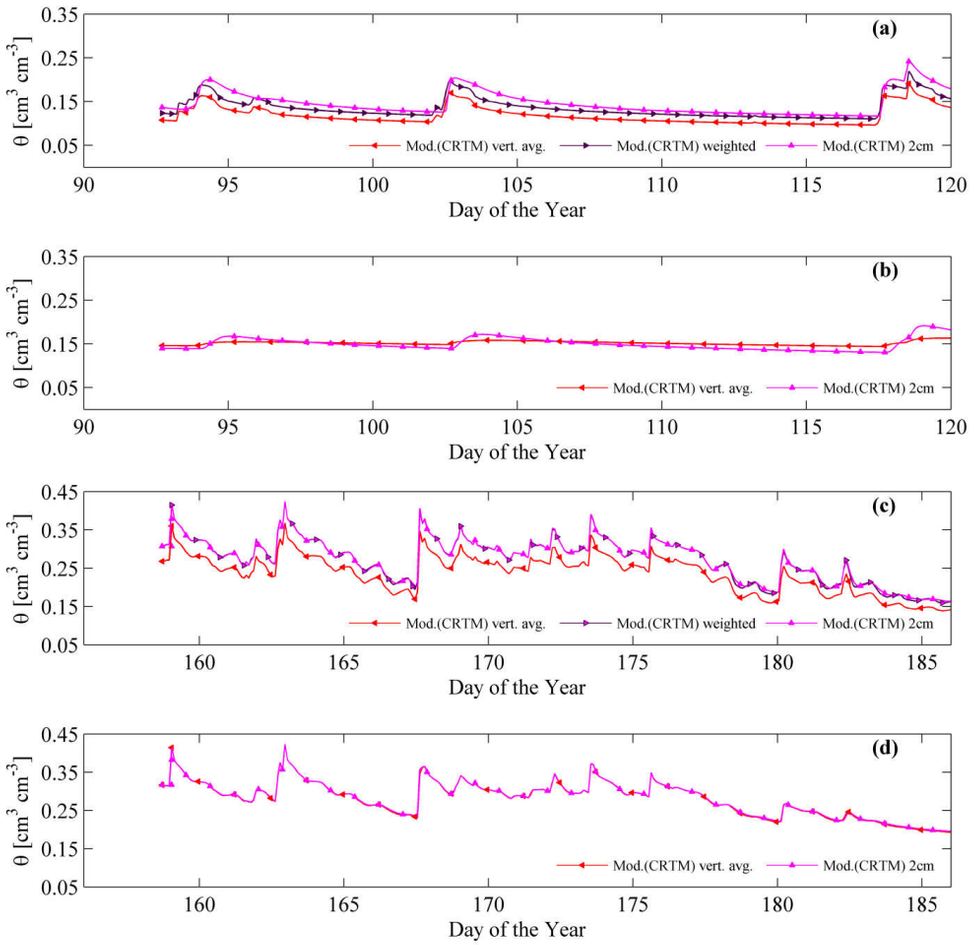

Figure III.16 Time series for two periods: DOY 92-120, 2011 (a, b) and DOY 158-186, 2011 (c, d), and two depths: 2 cm (a, c) and 5 cm (b, d) of volumetric soil moisture contents, θ, that are retrieved from brightness temperatures using the CRTM and the Durner bi-modal model: at the respective depths (magenta line); that are averaged over the entire presumed sensor's measurement volume, i.e. with inclusion of an air layer for the sensor installed at 2 cm depth, (red line); or that are averaged over the sensor's measurement volume excluding this air layer (dark magenta line).

In the previous comparisons, sensor measured water contents were compared with simulated water contents at a given depth. To evaluate the effect of vertical averaging of water contents by soil sensors on this comparison, depth weighted averages of the retrieved soil moisture contents were compared with the retrieved soil moisture contents at a single

depth (2 and 5 cm depth) and plotted together in Figure III.16. For 5 cm, the depth averaged retrieved water contents were very similar to the retrieved ones at 5 cm. For 2 cm depth, the vertically averaged retrieved soil moisture contents, which include low water contents in an air layer above the soil surface, represent soil moisture contents that would be measured by a sensor installed at 2 cm depth when no depth specific calibration would be used. Excluding the air layer from the calculation of depth averaged moisture contents (i.e. by dividing the depth weighted averaged water content in the 0 – 5.25 cm layer by the integral of weighting factors in this layer) reduced the difference between depth averaged moisture contents and the moisture contents at 2 cm considerably. This indicates that the moisture content that would be derived from a sensor installed at 2 cm depth using a depth specific calibration is not very different from the soil moisture at 2 cm depth. It must be noted that the vertical averaging and the thickness of the air layer that was considered in this averaging procedure was based on a very crude assessment.

5 Summary and conclusion

We monitored L-band brightness temperatures at horizontal polarization (TBH) of a tilled bare soil plot with a relatively high surface roughness. This was done for five 28-d periods so as to cover the range of soil hydrological conditions that may occur in different seasons of a temperate humid climate. From the measured brightness temperatures and the meteorological conditions at the site, soil surface roughness and soil hydraulic parameters were estimated using a closed loop inversion that linked a soil hydrological model with a roughness correction model and a radiative transfer model. The different 28-d periods were independently inverted so that the variation and consistency of the inverted parameters from independent measurements could be assessed. For the hydrological model, two models that describe the soil hydraulic properties: the uni-modal Mualem van Genuchten model (MvG), and the Durner bi-modal model (DBM), were considered. For the radiative transfer, a coherent radiative transfer model (CRTM), which accounts for the effect of vertical variations in dielectric permittivity, and the Fresnel model that predicts the emission from a soil profile with a vertically uniform dielectric permittivity, which was taken to be the average soil permittivity of a soil layer between 0 and 2 cm, or between 0 and 5 cm, were considered. The CRTM model in combination with the DBM model offered the most flexibility to match the simulated and measured TBHs (RMSDs between 4.4 and 12.3 K in the different periods). The results with Fresnel 0 – 2 cm were better than the results with Fresnel 0 – 5 cm and similar to

the results obtained with the CRTM. Based on this, it might be concluded that for this soil, a Fresnel model with a 2 cm layer thickness may be used to describe the brightness temperature dynamics.

A second important aspect of this paper was the validation of the retrieved parameters, in our case soil surface roughness and soil hydraulic properties, and the validation of the retrieved soil moisture contents by in situ measurements. The estimated values of the roughness parameter compared well with the observations made with the laser profiler, except for the dry period (DOY 92-120) when the model overestimated the roughness parameter. But, considering the semi-empirical nature of the surface roughness correction model and the spatial and temporal variability of soil surface roughness during the investigated periods, it seems difficult to obtain better correspondence.

The retrieved soil hydraulic properties were compared with soil hydraulic properties measured on soil columns in the lab. Despite the fact that soil surface was homogenized by tillage, the hydraulic properties of the different soil cores varied considerably, which may be attributed to their relatively small size (100 cm^3). Furthermore, the difference in spatial scale of the footprint of the radiometer and the soil columns may also result in differences between retrieved and directly measured soil hydraulic properties. The measured water retention curves on the soil cores indicated a bi-modal pore size distribution which justified the use of the DBM model for the inversion of the brightness temperatures. The retrieved retention curves for the different periods varied but all showed similar bi-modal distributions. This indicates that the time courses of the brightness temperatures contain some information about the multimodal shape of the water retention curve. A comparison between measured and retrieved unsaturated hydraulic conductivity curves is more difficult since no measurements containing information about the unsaturated hydraulic conductivity were done in the lab. When comparing the measured with retrieved saturated hydraulic conductivities, the retrieved saturated conductivities for the MvG model were smaller than the measured ones. This can be explained by the drastic change of the hydraulic conductivity close to saturation which is typical for well structured soils with a well developed interaggregate pore network besides the micropore network. The MvG model, which represents only one pore size distribution, tries to find a compromise between the high conductivities close to saturation and the lower conductivities under unsaturated conditions. The DBM model has more flexibility and the retrieved DBM conductivity curves showed a higher conductivity close to saturation and lower conductivity for more negative pressure heads than the MvG.

Finally, the retrieved soil moisture contents were compared with in-situ measurements. Similar to the brightness temperatures, we found that soil moisture contents that were retrieved using the CRTM model or 0 – 2 cm Fresnel model corresponded better with the in-situ measured moisture contents than the retrieved moisture contents using the 0 – 5 cm Fresnel model. This indicates that brightness temperatures are sensitive to soil moisture contents near to the soil surface.

However, measuring soil moisture using in-situ sensors close to the soil surface is a challenge. Only when a depth and site-specific calibration relation was used, the retrieved and measured soil moisture contents compared relatively well. The RMSDs between measured and retrieved soil moisture contents were slightly lower for the DBM than for the MvG model. The better fit of the brightness temperatures by the DBM model is therefore also translated into a better description of the soil moisture. However, the dynamics of the retrieved soil moisture, i.e. the change of water content just after a rain event, did not agree with that measured by the soil moisture sensors. It remains an open question whether this is due to a problem with the soil moisture sensors or the radiative transfer models for rough soil surfaces.

6 Acknowledgments

The presented in this study work is a part of the research unit FOR 1083 MUSIS (Multi-Scale Interfaces in Unsaturated Soil) funded by the German Research Foundation (DFG). We thank Prof. Dr. P.-S. Lammers and Dr. Lutz Damerow (Institute of Agriculture Engineering, Bonn) for the providing of the laser profiler. We thank the team of H. Jagdfeld (Central Institute of Technology, Research Centre Jülich) for the development of the holding construction of the radiometer; the team of A. Egmen and D. Schnabel (Technician workshop of IBG, Research Centre Jülich) for the building of the holding construction of the radiometer. We thank C. Steenpass, Dr. U. Rosenbaum and Dr. F. Jonard for the support during the development of the inversion approach. We thank the technician staff of the Agrosphere Institute, especially R. Harms and F. Engels for the technical support during the measurements; A. Langen for the laboratory measurements of the soil hydraulic properties and N. Hermes for the logging software for the radiometer data. M. Dimitrov thanks Dr. S. Huisman, Dr. A. Graf, Dr. J. Bikowski, Dr. I. Mladenova and Dr. Th. Holmes for all of the consultations and the model improvement.

IV Soil hydraulic parameters of bare soil plots with different soil structure inversely derived from L-band brightness temperatures

M. Dimitrov[(1)], J. Vanderborght [(1)], K.G. Kostov[(2)], B. Debecker[(3)], P. Schulze Lammers[(4)], L. Damerow[(4)], and H. Vereecken[(1)]

[(1)] Research Centre Jülich, Institute of Bio- and Geosciences: Agrosphere (IBG 3), Jülich, 52425, Germany

[(2)] Bulgarian Academy of Sciences, Institute of Electronics, Sofia, 1784, Bulgaria

[(3)] University of Leuven, Leuven, 3000, Belgium

[(4)] University of Bonn, Institute of Agricultural Engineering Bonn, Bonn, 53115, Germany

Submitted to Vadose Zone Journal

Received: Sept 30, 2014

1 Abstract

The structure of the surface layer of the soil is strongly influenced by soil tillage practices with important consequences for the hydraulic properties and soil moisture dynamics in the top soil layer. In this study we monitored during four 28-day periods L-band brightness temperatures and infrared temperatures over bare silt loam soil plots with different soil surface structure: tilled, seedbed, and compacted plots. Differences in absolute and normalized L-band brightness temperatures between the plots indicated that plot specific roughness, soil moisture contents, and soil hydraulic properties could be inverted from L-band brightness temperatures using a coupled radiative transfer, roughness correction, and soil hydrological models. The inversely estimated surface roughness parameters compared well with those derived from laser profiler measurements. The estimated saturated water contents of the tilled and seedbed plots were larger than the one of the compacted plot and the unsaturated hydraulic conductivity was smaller in the former plots than in the compacted plot for more negative pressure heads. These differences in hydraulic properties translated into larger dynamics and standard deviations of the simulated soil moisture during a 28-d measurement period in the tilled and seedbed plots than in the compacted plot. This difference was qualitatively confirmed by in-situ soil moisture measurements. Furthermore, differences in simulated actual evaporation rates between the plots were confirmed by observed differences in measured IR temperatures. The results indicate that effects of soil management on soil surface roughness and soil hydraulic properties can be inferred from L-band brightness temperatures.

2 Introduction

Knowledge about the soil hydraulic properties is important for determination of the water and energy flow in the soil (Vereecken et al., 2008). Thus, information about soil hydraulic properties is essential to model water balance, runoff and plant growth (Camillo et al., 1986), but an accurate description of water flow and contaminant transport in the vadose zone relies on accurate estimation of soil water retention and hydraulic conductivity functions (Vrugt and Dane, 2005).

Soil hydraulic properties are typically determined from soil cores in the laboratory (e.g. Dane et al., 2002; Durner and Lipsius, 2005) or from infiltration experiments in the field using various types of infiltrometers (Clothier and Brent, 2001). However, these measurements represent the properties of a relatively small soil volume. This in combination with a large spatial variability of soil hydraulic properties poses a problem when deriving effective hydraulic

properties of larger field plots. Furthermore, the boundary conditions that are used in these experiments may be distinctly different from field scale conditions. Inverse modelling approaches using in-situ field soil moisture measurements may be used to estimate effective soil hydraulic parameters (Vereecken et al., 2008). When the spatial support of the soil moisture measurements is sufficiently large using a large number of local soil moisture sensors that are connected in a wireless network (Bogena et al., 2010) or using sensors with a large support volume such as cosmic ray sensors (Zreda et al., 2008), gravimetry (Christiansen et al., 2011), electrical resistivity tomography or ground penetrating radar (Vanderborght et al., 2013), effective hydraulic properties at the field plot or field scale can be derived.

Besides varying in space, soil hydraulic properties may also vary considerably over time. Soil tillage and soil management have an important impact on the soil structure and consequently on soil hydraulic properties. Furthermore, the changes to the soil structure induced by tillage are unstable and vary over time (Strudley et al., 2008). Monitoring of the water content in the soil surface layer of field plots, fields or landscapes would therefore be useful to derive spatial and temporal patterns of soil properties that are induced by soil management (Hebrard et al., 2006) and to evaluate the impact of tillage practices on the soil water balance (Moret et al., 2007). In this perspective, remote sensing methods that provide information about the state of the soil surface over relatively large areas are of interest for upscaling from the point to the field scale and for deriving spatial patterns at the landscape scale.

Ground-based remote sensors were used frequently for calibration and validation of satellite based sensors and their data products (e.g. Wigneron et al., 2011; Schwank et al., 2012). However, ground-based sensors may also be used to observe soil processes at the field plot scale. In contrast to satellite or airborne sensors, ground-based sensors provide information with a high temporal resolution and can be used to monitor the land surface over a relatively long time period. They provide area wide information and therefore overcome the problem of upscaling point scale measurements. Considering microwave and infrared sensors, the vertical extent of the monitored soil volume is small so that these sensors provide information about the state of a thin soil surface layer. Therefore, they offer opportunities for investigating how properties of the soil surface layer influence processes at the land surface. In this study we used an L-band passive microwave radiometer and an infrared camera (IR) to monitor the state of the soil surface of differently tilled soil plots. Ground-based passive microwave and infrared measurements were implemented for estimating the relationships 1) between brightness temperature and soil moisture, saturated hydraulic conductivity and soil texture (Mattikalli et al., 1995; Burke et al., 1998; Mattikalli et al., 1998; Chang and Islam, 2000) and 2) between surface temperature and

evaporation rates (e.g. Olioso et al., 1996; Mauser and Schadlich, 1998). Based on these relationships brightness temperatures were used to estimate inversely hydraulic conductivity, matrix potential, soil moisture at saturation and bulk density (Burke et al., 1998) while infrared temperatures were used to estimate the Mualem van Genuchten (MVG) (Van Genuchten, 1980) soil hydraulic parameters (Steenpass et al., 2010).

L-band brightness temperatures depend on the roughness of the soil surface (Ulaby et al., 1986) so that roughness effects need to be disentangled from soil moisture and soil hydraulic property effects.

In the study presented in the previous chapter, radiative transfer, hydrological, dielectric mixing, and roughness correction models were coupled to determine and disentangle soil hydraulic and surface roughness parameters of a tilled bare soil plot from time series of L-band brightness temperatures using inverse modeling. In this study, we use the experimental setup and approach outlined in (Dimitrov et al., 2014) to investigate the effect of the structure of the soil surface layer of differently tilled soil plots on monitored L-band brightness temperatures and IR temperatures. Observed brightness temperatures of different plots were subsequently used to derive soil hydraulic parameters and surface roughness parameters using inverse modeling. The differences in L-band brightness temperatures between the plots were therefore used to identify differences in hydraulic properties and soil surface roughness parameters. However, inversely estimated parameters are uncertain due to measurement and model errors and limited information content in the observations. In order to evaluate whether the differences in estimated hydraulic parameters and simulated water contents and also the water fluxes between the different plots were consistent, we used the following evaluation criteria. An obvious criterion are posterior distributions of likely parameters given the observations, which we determined using the $DREAM_{ZS}$ algorithm (Vrugt et al., 2008a). In a second consistency check, hydraulic and roughness parameters that were derived from data during different time periods were compared. A third check consisted of comparing L-band derived roughness and hydraulic parameters with laser profiles measurements and hydraulic parameters that were derived from soil samples, respectively. In a fourth check, it was evaluated whether the predicted differences in hydrological behavior of the different plots was consistent with independent measurements. Therefore, predicted soil moisture contents were compared with in-situ soil moisture measurements and differences in predicted evaporation rates between the plots were compared with differences in measured IR surface temperatures.

3 Materials and Methods

3.1 Experimental setup and instrumentation

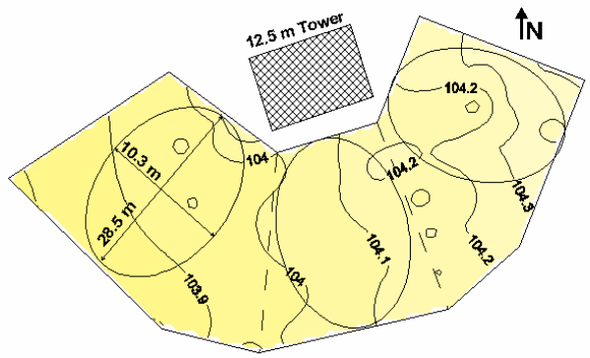

Figure IV.1 Top: mechanical field preparation (tilled plot (left from the tractor), seedbed plot (right from the tractor)). Photo from DOY 223. Bottom: location of the radiometer tower, different plots and -3 dB radiometer footprints, labeled lines and color scale denote the elevation (m.a.s.l.).

Three trapezoidal bare soil plots with widths between 12 m and 8 m and 28 m length were prepared for measurements within the Selhausen test site of the Forschungszentrum Jülich, Germany, (50° 52’ 8.6’’ N, 06° 27’ 57.2’’ E), which is part of the TERENO Rur observatory (Zacharias et al., 2011). The soil in the investigated plots has a silt loam texture (14.5 % sand, 69 % silt and 16.5 % clay, USDA classification). Since September 2006 the Selhausen test site was regularly treated with herbicides and kept free from weeds. Detailed description of the test site is given in (Weihermuller et al., 2007). The whole plot area was tilled to 15 – 20 cm depth with a semicircular Rabe Blue Bird 3GR (14 tooth, working width 3 m), manufactured by

Grégoire-Besson GmbH. After tillage 2/3 of the area was harrowed in the top 10 cm with a disc harrow Rabe Euro 7 (Figure IV.1). Finally, the soil surface of halve of the harrowed area, i.e. 1/3 of the field plot, was compacted with a hand operated roller. As a result, three measurement plots with three different soil surface structures were created: tilled plot, seedbed plot and compacted plot.

The preparation was repeated three times during the measurement campaign in 2011: March 15, 2011 (day of the year (DOY) 74), May 27, 2011 (DOY 147) and August 11, 2011 (DOY 223), respectively.

On DOY 80, five soil samples of 100 cm³ (5.0 cm diameter and 5.1 cm length) were taken in each plot and were used to determine the water retention curves in the lab and to measure the saturated water content.

The L-band radiometer JÜLBARA, equipped with dual-mode horn antenna (12° full beamwidth at -3 dB), operated at 1.4 GHz (corresponding to wavelength λ = 21.4 cm) was mounted on a tower at 12.5 m height above the soil surface, and measured the brightness temperature TB (K) at horizontal and vertical polarizations in two separate channels: 1.400-1.418 GHz and 1.409-1.427 GHz. Internal hot (338 K) and cold (278 K) loads were used for internal calibration of the radiometer. Additionally, external calibration of the radiometer was performed daily by measuring the sky brightness temperature. JÜLBARA is a follow-up model of the ELBARA radiometer, of which a detailed description is given in (Matzler et al., 2003). The integration time of the measurements was set to 10 seconds, the measurement cycle at one position was 1 minute and the sensitivity of the radiometer was 0.1 K.

Additionally, an infrared camera (VarioCam, Infratec GmbH, Dresden, Germany) with resolution of 320 by 240 pixels and spectral range from 8 to 14 µm was installed to measure the soil surface temperature every 2 minutes. Again, hourly mean values of the soil surface temperature were used in the analysis. In the temperature range between -10° and +50° C, an absolute measurement accuracy of ± 1.5 K was reported in (Steenpass et al., 2010).

The L-band radiometer JÜLBARA and the IR camera were mounted on rotating platform, which was fixed on the top of a 12.5 m high tower. The platform was operated by two electrical motors: one for horizontal (0 – 90°) and one for vertical (45 – 165° relative to nadir) movements of the L-band radiometer. The IR camera was moved only in the horizontal direction and was mounted on a special holding board with fixed angle of incidence β_0 = 45°. The movements of the platform, carrying the L-band radiometer and the infrared camera, were controlled using the software package LabView (National Instruments Inc.). In horizontal direction, the platform was set to move from the tilled plot over the seedbed plot to the compacted plot and back. A sketch

of the plots is given in Figure IV.1. In the vertical direction, the system was set to measure at three angles of incidence 52°, 56° and 60° over the soil surface, as well as at 135° in sky direction. The platform was stopped for measurements over every plot and incidence angle (except for the sky measurements which were performed every 8 hours for one hour) for 2 minutes so that the duration of the whole rotation cycle of the system was 18 minutes. Hourly mean values of the measured brightness temperature over a certain plot at horizontal polarization and 52° incidence angle were used for further analyses. The footprint of the L-band radiometer for this incidence angle was calculated as an oval with dimensions ~ 28.5 m by ~ 10.3 m without overlap between the plots.

A three dimensional laser profiler LMP-II (Sun et al., 2006), was used to determine the micro-topography of the soil surface of the plots. The measurements were carried out on the day after the plot preparation. The micro-topography of the plots (Figure IV.2) was determined using 124 profiles of 1500 mm length with a sampling interval of 2 or 4 mm.

Five ECH2O 5TE sensors (Decagon Devices Inc., Pullman, WA, USA) were installed horizontally in every measurement plot at ~ 2 cm depth. In 10 minutes intervals the relative dielectric permittivity of the soil, ε_r and soil temperature T_{Soil} (°C) were recorded and stored automatically in Em50 data loggers (Decagon Devices Inc., Pullman, WA, USA). Soil moisture was derived from ε_r measurements using a soil and sensor depth specific calibration relation for details see (Dimitrov et al., 2014).

Air temperature, precipitation, wind speed, humidity at 2 m height and the solar and global radiation were measured at the test-site and were used as forcing for the hydrological model. The meteorological data was used for calculation of hourly potential evaporation rates using the FAO guidelines (Allen et al., 1998).

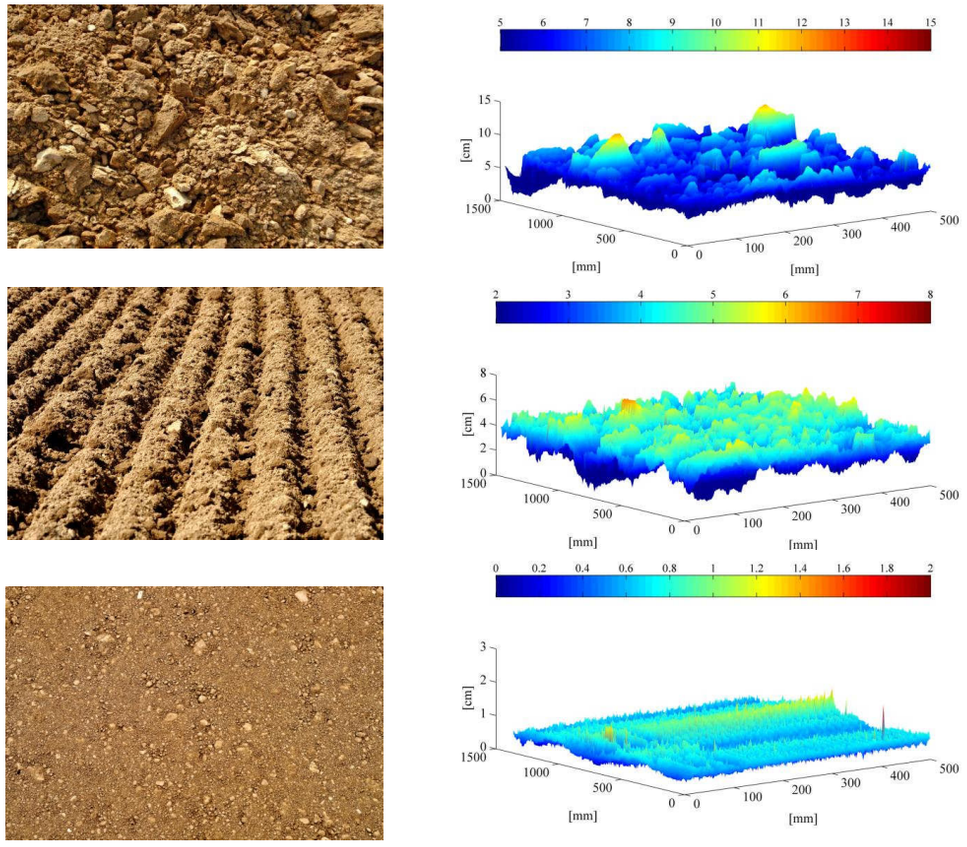

Figure IV.2 Tilled, seedbed and compacted plot (left). Topography of a 1500 x 500 mm area of the tilled, seedbed and compacted plot measured with the laser profiler. Photos and topography from DOY 96.

3.2 Models

3.2.1 Governing flow equation and soil hydraulic properties

One-dimensional vertical water flow was simulated in a homogeneous profile using the Richards equation (Jury and Horton, 2004):

$$\frac{\partial\theta(h)}{\partial t} = \frac{\partial}{\partial z}\left[K(\theta)\left(\frac{\partial h}{\partial z}+1\right)\right] \qquad \textbf{[IV.I]}$$

where h (cm) is the pressure head, θ (cm^{-3} cm^{-3}) the volumetric water content, K(θ) (cm/min) the hydraulic conductivity function, and z (cm) the elevation (positive upward).

The soil hydraulic properties θ(h) and K(θ) were parameterized assuming a bi-modal pore size distribution (Durner, 1994; Priesack and Durner, 2006):

$$\theta(h) = \begin{cases} \theta_r + (\theta_s - \theta_r)(w_1 S_{e1}(h) + w_2 S_{e2}(h)) & h < 0 \\ \theta_s & h \geq 0 \end{cases} \quad \textbf{[IV.II]}$$

$$S_{e,i}(h) = \left[1 + (\alpha_i |h|)^{n_i}\right]^{-m_i} \quad \textbf{[IV.III]}$$

$$K(\theta) = K_s \frac{(w_1 S_{e_1} + w_2 S_{e_2})^l \left(w_1 \alpha_1 \left[1 - (1 - S_{e_1}^{1/m_1})^{m_1}\right] + w_2 \alpha_2 \left[1 - (1 - S_{e_2}^{1/m_2})^{m_2}\right] \right)^2}{(w_1 \alpha_1 + w_2 \alpha_2)^2} \quad \textbf{[IV.IV]}$$

where θ_r is the residual ($cm^3\ cm^{-3}$) and θ_s the saturated volumetric water contents ($cm^3\ cm^{-3}$), S_{ei} is the saturation degree of the i^{-th} pore size distribution, α_i (cm^{-1}) and n_i are shape parameters, $m_i = 1\text{-}1/n_i$, and w_i is the volume fraction of the i^{-th} pore size distribution with $w_1 + w_2 = 1$, and l is the pore-connectivity parameter which was assumed to be 0.5 (Mualem, 1976).

The HYDRUS 1D code (Simunek et al., 2008) was used to solve the Richards equation for given initial and boundary conditions. A 200 cm deep soil profile with a spatial discretization of 0.25 cm was considered. The water flux on the soil surface was controlled by potential evapotranspiration rates and precipitation. All model runs were started from a uniform initial pressure head of -100 cm. A spin-up period of one month was used to reduce the impact of the initial conditions on the simulation results (Chanzy et al., 2008).

3.3 Model coupling and parameter estimation

3.3.1 Forward run and model coupling

Precipitation and calculated potential evaporation were used to define upper boundary conditions of the flow domain and Richards equation was used to simulate the observed soil moisture profiles. A mixed upper boundary condition was used with prescribed fluxes when the soil water pressure head was above a critical pressure head (h_{crit} = -15000 cm) and lower than 0 cm or a fixed pressure head when the critical pressure heads were reached and the simulated fluxes were (in absolute values) lower than the precipitation rate or potential evaporation rate. From the simulated soil moisture profiles, dielectric permittivity profiles were calculated using the Wang and Schmugge model (Wang and Schmugge, 1980). From the dielectric permittivity profiles the reflectivity, R_H, was calculated using the multilayer CRTM given in (Bass et al.,

1996). In the next step, a correction for the surface roughness effect was implemented using the model of (Choudhury et al., 1979), which includes the reflectivity R_H, the variance of surface heights σ^2, the incidence angle β_0 and the wavelength λ. According to this model, the rough surface reflectivity R_{rH}, is related to the reflectivity of a smooth surface R_H as:

$$R_{rH} = R_H \exp\left(-\frac{16\pi^2}{\lambda^2}\sigma^2 \cos^2\beta_0\right) \qquad \textbf{[IV.V]}$$

Finally, simulated brightness temperature values, TBH, were calculated using the radiative transfer model presented in (Ulaby et al., 1986):

$$TBH = (1 - R_{rH})T_{eff} + TB_{sky}R_{rH} \qquad \textbf{[IV.VI]}$$

where R_{rH} is the reflectivity, corrected for surface roughness, TB_{sky} is the sky brightness temperature, calculated as in (Dimitrov et al., 2012) and T_{eff} is the effective soil temperature. In this study the measured soil temperature values at 2 cm were used in the radiative transfer model [IV.VI] instead of effective soil temperature: for details see the previous chapter or (Dimitrov et al., 2014). During every single forward run of the model time series of simulated brightness temperatures were calculated with a given parameter set which consists of eight hydraulic parameters $(\theta_r, \theta_s, \alpha, n, K_s, w_2, \alpha_2, n_2)$ and a surface roughness correction parameter σ, and which was provided by the global optimization algorithm presented in the next subsections. A complete description of the models as well as a flow chart diagram of the inversion procedure are given in the previous chapter, as well as in (Dimitrov et al., 2014).

3.3.2 Parameter estimation for plots with different soil structure

The measurement campaign carried out in 2011 was split in four different measurement periods, each 28 days long (DOY 92-120, DOY 158-186, DOY 188-216 and DOY 226-254). Soil hydraulic and roughness parameters were estimated for each period. These periods were selected because of: 1) field preparation; 2) changes in the soil surface structure of the plots after the field preparation; 3) gaps in the TBH data series; and 4) measurements for external calibration of the radiometer. Therefore, with the splitting of the periods, the inversion approach could be tested for periods with different meteorological conditions. The periods may be

described as dry with total amount of rainfall equal to 1.49 cm (DOY 92-120), as wet with total amount of rainfall equal to 13.32 cm (DOY 158-186) or as mixed periods of dry and wet phases (DOY 188-216 and DOY 226-254) (see also Table IV.5 for the rainfall and potential evaporation rates during the different periods).

3.3.3 Global optimization algorithms

In this study two different optimization techniques were implemented to estimate not only the optimal solution ("best parameter set") of hydraulic parameters and roughness correction factor, but also to provide information about the posterior distribution of the estimated parameters.

The Shuffled Complex Evolution (SCE-UA) algorithm (Duan et al., 1992; Duan et al., 1993) and the DiffeRential Evolution Adaptive Metropolis ($DREAM_{zs}$) algorithm (Vrugt et al., 2008b; Vrugt et al., 2009) were implemented in the inversion approach. As a result, one parameter set (SCE-UA) or information about the parameter uncertainty and posterior distribution of the optimized parameters ($DREAM_{zs}$) was obtained. For a detailed description of the SCE-UA and $DREAM_{zs}$ algorithms we refer also to (e.g. Sorooshian et al., 1993; Duan et al., 1994) for SCE-UA and (e.g. Scharnagl et al., 2011; Bikowski et al., 2012; Laloy and Vrugt, 2012) for $DREAM_{zs}$.

3.4 Objective / likelihood functions

Following the classical statistical estimation theory, the best parameter set estimated from L-band brightness temperatures can be obtained after minimizing the following least square objective function:

$$\Phi_{TBH} = \sum_{i=1}^{N} (TBH_{meas,i} - TBH_{mod,i})^2 \qquad \textbf{[IV.VII]}$$

where TBH_{meas} and TBH_{mod} are the measured and modeled brightness temperature values at horizontal polarization and N is the number of measurements. This function was used in the inversion routine with the SCE-UA global optimizer algorithm.

If an inversion is cast in a Bayesian framework, the difference between measured and modeled values is defined as a likelihood, which is the probability of observing the data given the model parameters (Bikowski et al., 2012). Several different formulations of likelihood

functions are available in the DREAM$_{ZS}$ code and are presented in (Schoups and Vrugt, 2010). In our study, we used the following likelihood function:

$$l_{TBH}(\Theta) = -0.5N * \ln(2\pi) - \sum_{i=1}^{N} \ln\left(s_{meas,i}\right) - 0.5\sum_{i=1}^{N}\left(\frac{TBH_{meas,i} - TBH_{\mathrm{mod},i}(\Theta)}{s_{meas,i}}\right)^2 \qquad \textbf{[IV.VIII]}$$

where Θ is the vector of parameters that are optimized and s_{meas} denotes the standard deviation of the residuals between the measured and modeled brightness temperature values. s_{meas} is typically unknown and was implemented in the inversion routine as an additional fitting parameter.

4 Results and disscussion

4.1 Measured and modelled brightness temperature

Figure IV.3 shows time series of measured brightness temperature at 52°, horizontal polarization TBH for all measurement periods and plots together with the cumulative rainfall. TBH differed between plots and between periods due to differences in soil moisture content: higher TBH were observed during the driest period DOY 92-120 with only 1.49 cm of total rainfall (see also Table IV.5) and lowest TBH were observed during the wetter periods DOY 158-186 with 13.32 cm total rainfall and period DOY 226-254 with 9.01 cm of rain. The TBH values also changed during a period as a response to rainfall and soil evaporation with rapid and large drops of TBH just after rainfall events.

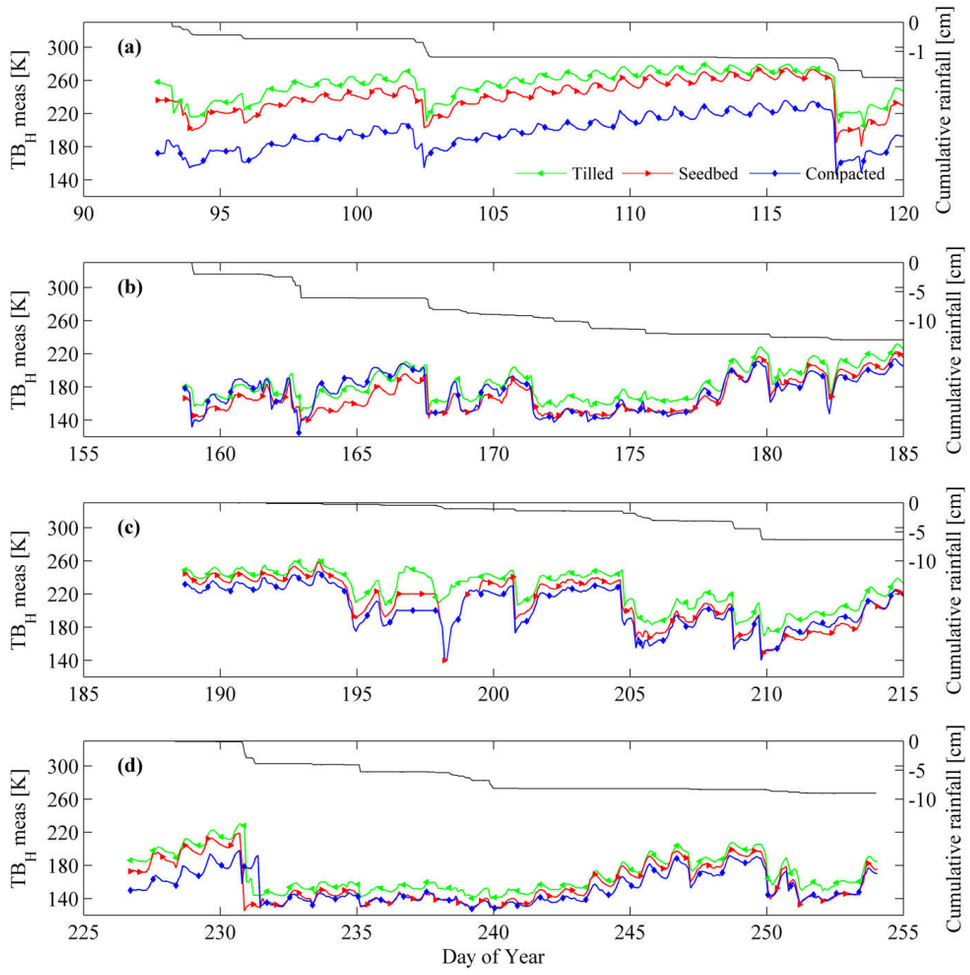

Figure IV.3 Time series of measured brightness temperatures TBHs from the tilled plot, the seedbed plot and the compacted plot, as well as cumulative rainfall for periods (a) DOY 92-120, (b) DOY 158-186, (c) DOY 188-216 and (d) DOY 226-254.

Figure IV.4 illustrates for the compacted plot and for two investigated periods that the temporal dynamics of TBH due to atmospheric boundary conditions (rainfall and soil evaporation) can be described quite well using a coupled soil hydrological, radiative transfer, and roughness correction models of which the soil hydraulic parameters and roughness correction parameters were obtained using inverse modeling. The 95 % confidence intervals of the modeled TBH, which were obtained using $DREAM_{zs}$, comprehended almost all measured TBH values which indicates that the model assumption of constant roughness and soil hydraulic parameters was appropriate.

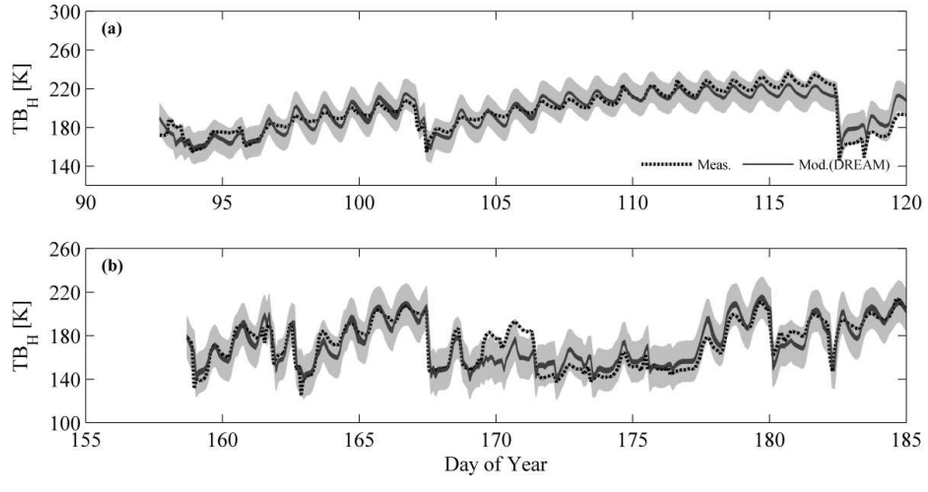

Figure IV.4 Time series of measured (dotted black line) and modeled (black line) brightness temperatures TBHs of the compacted plot for period DOY 92-120 (a) and DOY 158-186 (b). The transparent gray bands represent the 95% confidence intervals of the modeled brightness temperatures estimated with DREAM$_{ZS}$.

Concerning the differences in TBH between the plots it can be concluded in general that the differences were larger during drier periods (period DOY 92-120, DOY 188-204 and DOY 226-231) and that during these drier periods the TBH of the compacted plot were smaller than those of the seedbed and tilled plots. For the wetter periods, the differences were smaller and the compacted plot did not always show the lowest TBH values. For the same soil moisture content, a higher roughness leads to a lower reflection and therefore a higher TBH. Due to different hydraulic properties of the plots, the soil moisture contents may differ between the plots at a certain time, which also contributes to the difference in brightness temperature between the plots.

In order to disentangle the effect of differences in soil moisture contents and soil roughness on TBH differences between plots, a normalized brightness temperature TBH_{norm} was defined as:

$$TBH_{norm} = \frac{TBH_{smooth} - TBH_{rough}}{TBH_{smooth} - T_{eff}} = \frac{(R_{Hsmooth} - R_{Hrough}) * (T_{eff} - TB_{sky})}{R_{Hsmooth} * (T_{eff} - TB_{sky})} = 1 - \frac{R_{Hrough}}{R_{Hsmooth}} \quad \textbf{[IV.IX]}$$

where TBH_{rough} and TBH_{smooth} are the brightness temperatures of the rough surface (tilled or seedbed plot) and of the smooth surface (compacted plot), R_{Hrough} is the reflectivity of the tilled /

seedbed plot and $R_{Hsmooth}$ is the reflectivity of the compacted plot. When there is no difference in soil moisture between the plots and when the roughness of the plots remains constant over time, then TBH_{norm} should remain constant over time as well. For a constant roughness, changes of TBH_{norm} over time must therefore be due to different changes in water contents in the different plots and therefore contain information that can be used to infer differences in soil hydraulic properties between the different plots.

Figure IV.5 shows measured and modeled TBH_{norm} for the dry (DOY 92-120) (a, b) and wet (DOY 158-186) (c, d) periods and for the tilled (a, c) and seedbed (b, d) plots. Similar plots are shown for the other periods in Figure IV.6. During the dry period, TBH_{norm} decreases substantially after rainfall events. These results indicate that because of the wetting of the soil surface, the reflection coefficients of the rougher tilled and seedbed plots increase more than the reflection coefficient of the smoother compacted plot. During wet periods, TBH_{norm} is generally smaller than during dry periods and increases with time when the soil dries out. The modeled normalized brightness temperatures matched the evolution of the measured normalized brightness temperatures quite well. It should be noted that the model was parameterized using TBH values. The fact that TBH_{norm} varies over time and that this variation can be described by the model of which roughness and hydraulic parameters are derived from TBH measurements, indicates that time series of TBH values contain information that enables to infer differences in soil hydraulic properties besides differences in surface roughness of the different plots. However, there is one noticeable mismatch between the simulated and measured TBH_{norm} between DOY 226 and 231. The plot preparation for this period took place on DOY 223 (see also Table IV.4), i.e. just before the measurement period, during a relatively dry period. A strong rainfall on DOY 230.9 therefore altered the structure of the soil surface and the soil surface roughness. In the model approach, soil surface roughness and structure was assumed to be constant over time so that changes in surface roughness could not be described by the model.

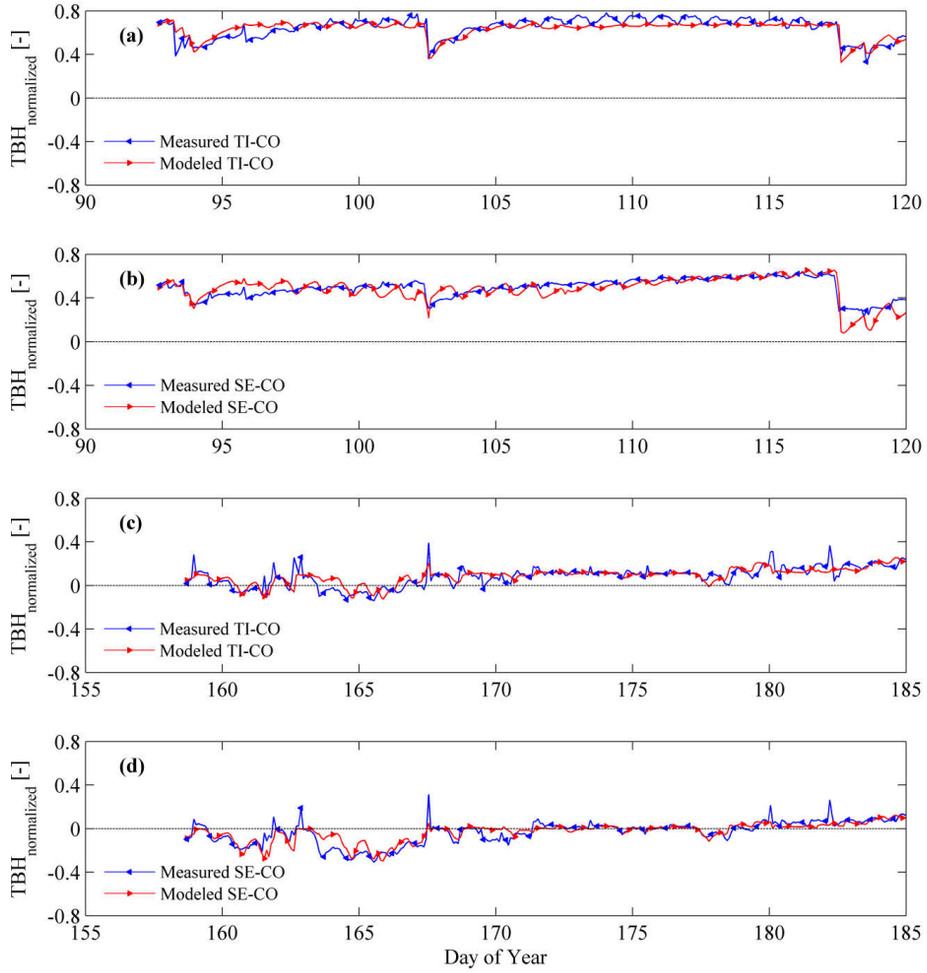

Figure IV.5 Time series of measured and modeled normalized TBHs, calculated as the difference between TBHs from tilled and compacted plots (a and c) or as the difference between TBHs from seedbed and compacted plots (b and d) for periods DOY 92-120 (a and b) and DOY 158-186 (c and d).

To evaluate the model performance and the two optimization algorithms, SCE-UA and $DREAM_{zs}$, the RMSD between modeled and measured TBH is given in Table IV.1, Table IV.2 and Table IV.3. The two optimization algorithms yielded similar results. The RMSDs varied between 6 and 10 K for the different periods and plots, except for the period DOY 226-254 for which RMSDs of 15 K were obtained. As was inferred from the TBH_{norm} for this period, this is probably due to the change in soil surface structure after the strong rainfall at the beginning of the monitoring period.

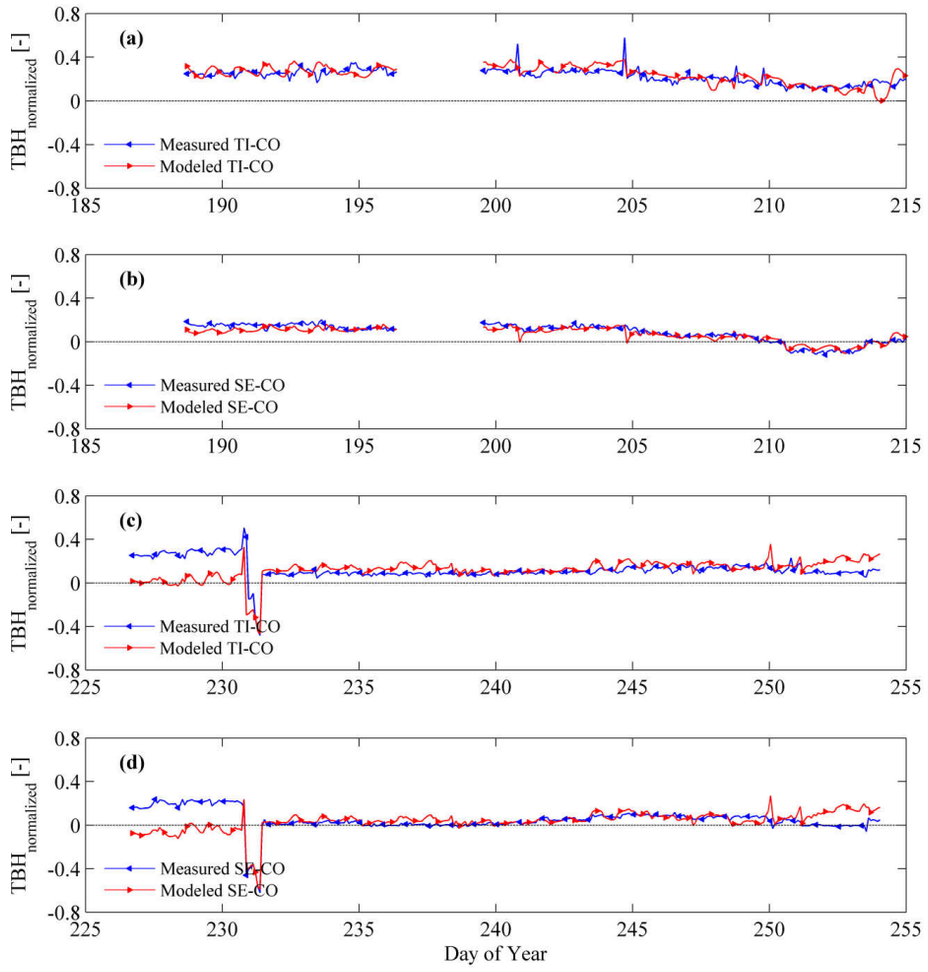

Figure IV.6 Time series of measured and modeled normalized TBH, calculated as the difference between TBHs from tilled and compacted plots (a and c) or as the difference between TBHs from seedbed and compacted plots (b and d) for periods DOY 188-216 (a and b) and DOY 226-254 (c and d).

Table IV.1 Parameters of the Durner bi-modal soil hydraulic functions estimated for the tilled plot and derived by DREAM$_{zs}$ and SCE-UA from measured L-band brightness temperatures using coupled inversion for the different measurement periods.

Tilled		θ_r (cm^3cm^{-3})	θ_s (cm^3cm^{-3})	α_1 (1/cm)	n_1 -	K_s (cm/min)	λ -	w_2 -	α_2 (1/cm)	n_2 -	RMSD (K)
Method	Period DOY	Inverted from TBH									
	Initial Range	0-0.1	0.30-0.5	(0.5-100)10^{-3}	1–3	(1 – 1000)10^{-3}	0.5	0 -0.6	(10-1000)10^{-3}	1 - 4	
SCE-UA	92-120	0.01	0.49	0.0147	2.74	0.0015	0.5	0.088	0.526	1.47	6.28
DREAM$_{zs}$	92-120	0.00	0.42	0.012	2.89	0.002	0.5	0.09	0.639	1.43	6.43
DREAM$_{zs}$ ranges	92-120	0.00-0.02	0.40-0.5	0.009-0.022	2.2-3.0	0.001-0.026	0.5	0.046-0.263	0.17-0.99	1.05-1.77	6.28-6.64
SCE-UA	158-186	0.03	0.47	0.0018	2.01	0.003	0.5	0.37	0.030	2.51	8.44
DREAM$_{zs}$	158-186	0.03	0.47	0.002	2.17	0.001	0.5	0.36	0.017	3.86	8.47
DREAM$_{zs}$ ranges	158-186	0-0.05	0.41-0.5	0.001-0.016	1.31-2.5	0.001-0.84	0.5	0.015-0.60	0.01-0.84	1.16-3.99	8.44-8.81
SCE-UA	188-216	0.00	0.48	0.0018	2.27	0.026	0.5	0.10	0.220	2.61	8.24
SCE-UA	226-254	0.06	0.50	0.001	1.68	0.002	0.5	0.22	0.033	2.87	15.47
Lab	data	0.0	0.373	0.0032	1.44	0.066	0.5	0.26	0.077	2.64	

Table IV.2 Parameters of the Durner bi-modal soil hydraulic functions estimated for the seedbed plot and derived by DREAM$_{zs}$ and SCE-UA from measured L-band brightness temperatures using coupled inversion for the different measurement periods.

Seedbed		θ_r (cm^3cm^{-3})	θ_s (cm^3cm^{-3})	α_1 (1/cm)	n_1 -	K_s (cm/min)	λ -	w_2 -	α_2 (1/cm)	n_2 -	RMSD (K)
Method	Period DOY	Inverted from TBH									
	Initial Range	0-0.1	0.30 – 0.50	(0.5-100)10^{-3}	1–3	(1 – 1000)10^{-3}	0.5	0 -0.6	(10-1000)10^{-3}	1 - 4	
SCE-UA	92-120	0.01	0.45	0.012	2.68	0.002	0.5	0.156	0.504	1.50	8.15
DREAM$_{zs}$	92-120	0.01	0.43	0.0009	2.47	0.054	0.5	0.25	0.50	3.74	8.06
DREAM$_{zs}$	92-120	0-0.01	0.43-0.47	0-0.02	2.42-2.53	0.001-0.06	0.5	0.15-0.25	0.5-0.87	2.2-2.46	8.06-8.49
SCE-UA	158-186	0.015	0.460	0.004	1.625	0.030	0.5	0.28	0.116	1.67	8.12
DREAM$_{zs}$	158-186	0.033	0.459	0.002	2.946	0.012	0.5	0.47	0.055	1.74	7.89
DREAM$_{zs}$ ranges	158-186	0-0.06	0.39-0.5	0.0-0.004	1.52-3	0.001-0.975	0.5	0.13-0.6	0.01-0.9	1.03-4	7.89-8.43
SCE-UA	188-216	0.001	0.475	0.003	2.11	0.013	0.5	0.40	0.07	1.83	11.08
SCE-UA	226-254	0.09	0.50	0.005	1.79	0.029	0.5	0.19	0.35	1.38	14.66
Lab	data	0.0	0.40	0.0034	1.32	0.038	0.5	0.203	0.067	2.64	

Table IV.3 Parameters of the Durner bi-modal soil hydraulic functions estimated for the compacted plot and derived by DREAM$_{zs}$ and SCE-UA from measured L-band brightness temperatures using coupled inversion for the different measurement periods.

Compacted		θ_r (cm^3cm^{-3})	θ_s (cm^3cm^{-3})	α_1 (1/cm)	n_1 -	K_s (cm/min)	λ -	w_2 -	α_2 (1/cm)	n_2 -	RMSD (K)
Method	Period DOY	Inverted from TBH									
	Initial Range	0-0.1	0.30-0.5	(0.5-100)10^{-3}	1–3	(1 – 1000)10^{-3}	0.5	0 -0.6	(10-1000)10^{-3}	1 - 4	
SCE-UA	92-120	0.02	0.38	0.001	1.49	0.014	0.5	0.33	0.015	2.40	8.01
DREAM$_{zs}$	92-120	0.00	0.40	0.001	1.36	0.257	0.5	0.28	0.073	2.32	7.89
DREAM$_{zs}$ ranges	92-120	0.0-0.003	0.30-0.49	0.0-0.01	1.31-1.57	0.001-0.99	0.5	0.07-0.47	0.01-0.72	1.26-3.99	7.89-8.21
SCE-UA	158-186	0.01	0.32	0.004	1.33	0.001	0.5	0.002	0.035	2.12	9.35
DREAM$_{zs}$	158-186	0.04	0.33	0.004	1.59	0.004	0.5	0.09	0.078	1.06	9.51
DREAM$_{zs}$ ranges	158-186	0-0.05	0.30-0.39	0.002-0.008	1.25-2.44	0.001-0.03	0.5	0.006-0.22	0.01-0.63	1-3.94	9.51-9.81
SCE-UA	188-216	0.014	0.35	0.018	1.52	0.006	0.5	0.313	0.094	2.09	11.55
SCE-UA	226-254	0.039	0.42	0.003	1.23	0. 230	0.5	0.053	0.673	2.34	11.21
Lab	data	0.00	0.41	0.0039	1.33	0.017	0.5	0.211	0.060	2.88	

4.2 Water retention and hydraulic conductivity functions

Figure IV.7 presents the water retention (Figure IV.7 (a, c, e)) and hydraulic conductivity curves (Figure IV.7 (b, d, f)) of the different plots that were derived from soil cores (black lines with bars for maximum and minimum at each pressure step represent the laboratory data) and from L-band brightness temperatures using the coupled inversion approach for all investigated periods (colored lines). To avoid extrapolation of the soil hydraulic functions for conditions that were not observed during the periods, water contents and hydraulic conductivities are shown only for the range of pressure heads in the 0 – 2 cm top soil layer i.e. the soil layer that is seen by the L-band radiometer (e.g. Escorihuela et al., 2010; Dimitrov et al., 2014) that were simulated using the optimal parameter set during the respective periods. The gray zones in Figure IV.7 (a-f) denote the 95 % confidence intervals of the hydraulic functions estimated with DREAM$_{zs}$ for the periods DOY 92-120 and DOY 158-186. For the other periods, the optimal hydraulic functions obtained using SCE-UA are given. In Table IV.1, Table IV.2 and Table IV.3 the parameters of Durner bi-modal model that were derived from the laboratory data for every plot and from the inversion of the brightness temperatures with DREAM$_{zs}$ or SCE-UA are given.

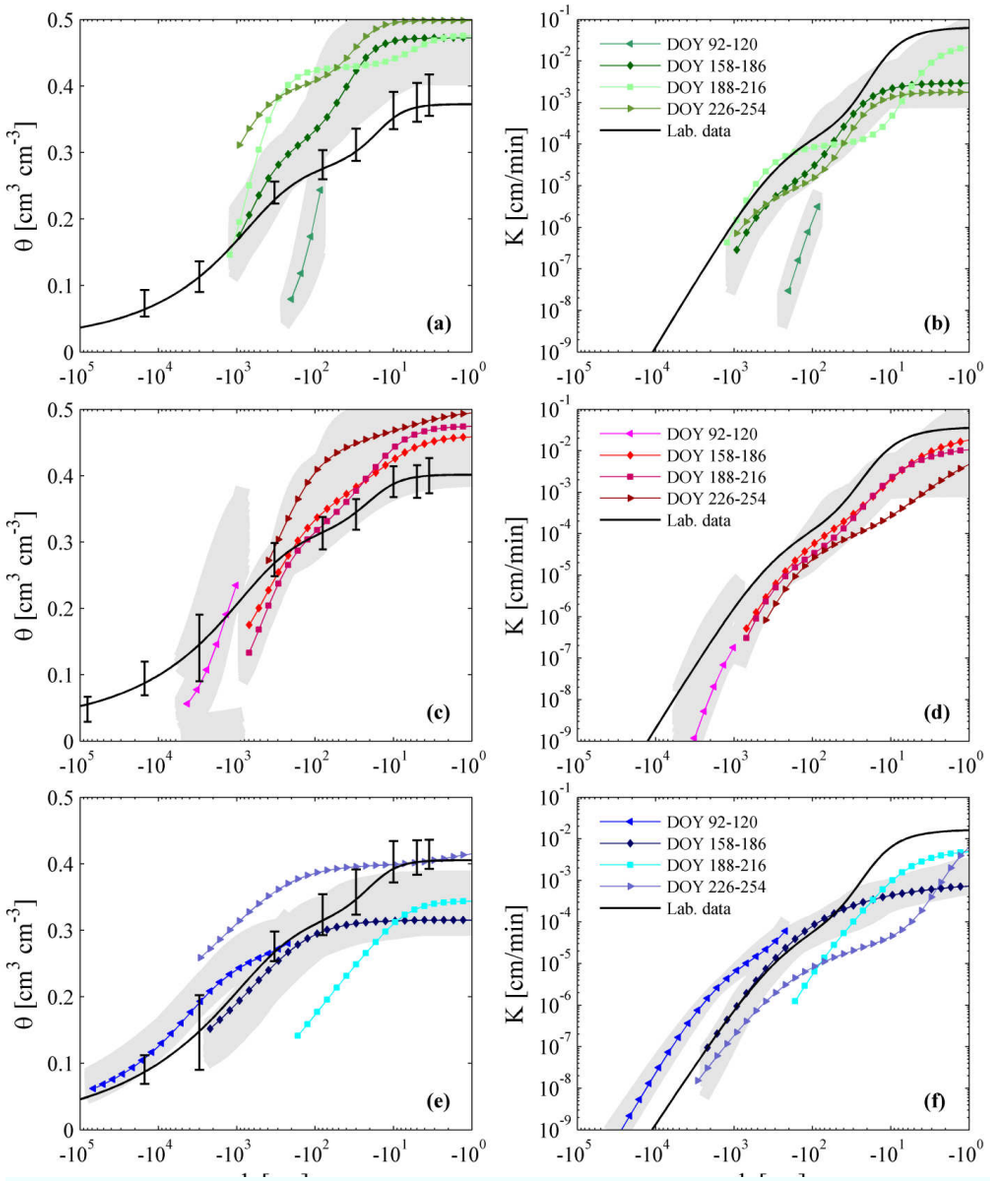

Figure IV.7 Volumetric water content θ (a, c, e), and hydraulic conductivity, K (b, d, f) as function of pressure head h. The parameters of the curves were derived from time series of the brightness temperatures using SCE-UA for tilled plot (a, b), seedbed plot (c, d) and compacted plot (e, f). The gray zones represent the 95% confidence intervals and were constructed using the marginal distributions of soil hydraulic parameters obtained with DREAM$_{ZS}$ for the periods DOY 92-120 and DOY 158-186.

The water retention and hydraulic conductivity curves, derived from the laboratory data suggest bi-modal pore size distributions for all plots. Despite the large differences in soil structure due to the plot preparation, the hydraulic functions and parameters that were derived

from the soil samples did not differ considerably between the different soil plots. Furthermore, the saturated soil moisture θ_s = 0.41 cm^3 cm^{-3} value, estimated for the compacted plot was the highest compared to θ_s estimated for the tilled and the seedbed plots. The highest pressure head, which was used in the laboratory for the estimation of the water retention curve, was -3.5 cm. As mentioned in (Dimitrov et al., 2014) at this pressure head the inter-aggregate pores of the tilled plot drained already, so the saturated water content θ_s might be larger than the water content at -3.5 cm. Similar differences between θ_s and water content at -3.5 cm pressure head were expected for the seedbed plot. The values of the lab measured saturated hydraulic conductivity K_s were slightly different between the different plots: for the compacted plot 0.017 cm/min, for the seedbed plot 0.038 cm/min and for the tilled plot 0.066 cm/min were measured, respectively (Table IV.1, Table IV.2 and Table IV.3).

When comparing the inversely estimated soil hydraulic functions and parameters from L-band brightness temperatures with those from the soil cores (Figure IV.7 (a-f), Table IV.1, Table IV.2 and Table IV.3), there are more outspoken differences between the different plots. Because of the different hydrological conditions and possible differences in soil structure, the inversely estimated functions and parameters also differed between different periods. For the dry period DOY 92-120, the values of the modeled soil moisture in the 0 – 2 cm layer varied between 0.05 and 0.25 cm^3 cm^{-3}. In the other wetter periods the values varied between 0.15 and 0.49 cm^{-3} cm^{-3} (DOY 158-186), 0.13 and 0.48 cm^3 cm^{-3} (DOY 188-216), and 0.25 and 0.49 cm^3 cm^{-3} (DOY 226-254), respectively. For the seedbed and compacted plots, the functions obtained for the dry period (DOY 92-120) seemed to connect well with those obtained from the wetter periods. However, for the tilled plot and the dry period, the pressure heads were for the same water contents and hydraulic conductivity larger than for the wetter periods.

During the whole dry period DOY 92-120, the soil was not saturated so that the inversely estimated K_s and θ_s are extrapolations of the hydraulic functions that were calibrated to measurements in the dry range of soil moisture contents. This extrapolation may lead to large uncertainties of water contents and hydraulic conductivities for larger pressure heads and consequently to large uncertainties of inversely estimated K_s and θ_s. For the compacted plot, the 95 % uncertainty range of K_s and θ_s obtained with $DREAM_{ZS}$ spanned almost the range of the prior distribution. Also for the wet period DOY 158-186, the uncertainty of the estimated θ_s and K_s was large. For this period, the uncertainties of K_s for the tilled and seedbed plot spanned almost the range of the prior distribution. However, although the uncertainty of the saturated hydraulic conductivity (at h = 0 cm) is about a factor 10^3, the uncertainty in the conductivity drops to a factor 10 when h becomes smaller than -10 cm (see Figure IV.7 (b, d, f)). For h larger

than -10 cm, the soil water content hardly changes with increasing h (see Figure IV.7 (a, c, e)) whereas the soil hydraulic conductivity may change in this range of pressure heads by a few orders of magnitude. Because L-band brightness temperature is correlated to soil water content and because of the highly nonlinear behavior of the hydraulic conductivity function close to saturation, the uncertainty of the estimated saturated hydraulic conductivity can be much larger than the uncertainty of the unsaturated hydraulic conductivities. As an illustration, the hydraulic conductivity of the compacted plot that was derived for the period DOY 226-254, which was much wetter than the period DOY 92-120, could be considered. Despite the wetter conditions, the simulated pressure heads in the plot did not reach saturated conditions. Due to the large fitted α_2 parameter ($\alpha_2 = 0.673$ cm^{-1}, see Table IV.3) for this period, the hydraulic conductivity curve was highly nonlinear in h close to saturation. In Figure IV.7 (f) the conductivity is plotted for the range of pressure heads that were simulated for the compacted plot in this period (up to h = 1 cm). The corresponding hydraulic conductivities in the compacted plot for the range of simulated pressure heads during this period were not considerably larger than during other periods (even smaller for smaller pressure heads) as would be suggested by the fitted K_s. This example illustrates again that, due to the nonlinearity of the hydraulic properties, the fitted parameters of hydraulic functions could not be interpreted as physically meaningful when they represent a property that falls outside the range of conditions that were considered to derive the parameter.

Despite the large uncertainty of the fitted parameters of the hydraulic functions, the uncertainty of the functions themselves allows drawing some conclusions about the differences between the plots and between the lab derived and L-band brightness temperature derived hydraulic properties.

Most of the hydraulic functions suggested a bi-modal pore size distribution ($w_2 > 0$). However, some of the parameter sets estimated for the compacted plot, suggested also a uni-modal model parameter distribution ($w_2 = 0$).

For the tilled plot, the inversely estimated water retention curves from L-band brightness temperatures showed larger soil moisture contents at higher pressure than the laboratory derived retention curves. Although not significant (error bars of the lab derived data and the 95 % confidence intervals of the water retention curves estimated with DREAM$_{zs}$ overlapped), the same holds true for the seedbed plot whereas for the compacted plot, the L-band derived water retention curves show smaller water contents at larger pressure heads than the lab derived retention curves. The inversely estimated saturated soil moisture θ_s for the tilled plot varied between 0.42 and 0.49 cm^3 cm^{-3} for all investigated periods, for the seedbed plot between 0.42 and 0.50 cm^3 cm^{-3}, and for compacted plot between 0.32 and 0.42 cm^3 cm^{-3} (Table IV.1, Table

IV.2, Table IV.3). In general, the differences in water contents at higher pressure heads between the different plots, with higher water contents in the tilled and seedbed plots than in the compacted plot are more outspoken for the water retention curves that were derived from L-band data than from the soil cores that were analyzed in the laboratory.

Although very uncertain, the inversely estimated hydraulic conductivities between h = -10 cm and -1 cm are larger for the tilled and seedbed plots than for the compacted plot. In the range of pressure heads between -10^4 and -10^2 cm, the inversely estimated hydraulic conductivities are larger for the compacted plot than for the seedbed and the tilled plots. In the latter two plots, the hydraulic conductivity decreases more strongly with decreasing pressure head.

The differences in L-band derived hydraulic properties between the different plots reflect the effect of tillage on the soil structure, the pore size distributions and the pore connectivity. Tillage creates a separate population of large inter-aggregate pores that drain at large pressure heads.

Due to compaction, the inter-aggregate pores are lost so that the porosity and water content at larger pressure heads is decreased. The large inter-aggregate pores also lead to larger hydraulic conductivities when the soil is nearly saturated. On the other hand, the micro-pores or intra-aggregate pores structure is disconnected by the aggregate formation. As a consequence, the water flow through the contact area between the aggregates becomes a bottleneck for the unsaturated flow when the inter-aggregate pores drain. This explains the sharp decrease of the hydraulic conductivity with decreasing pressure heads (e.g. Carminati et al., 2007b; Carminati et al., 2007a; Carminati et al., 2007c). Upon compaction, the connection between the aggregates is restored.

The difference between the lab and L-band derived hydraulic properties may be due to the fact that the compaction affected the structure of the upper few cm of the soil, which are ‘seen’ by the radiometer, whereas the soil cores, which sampled a 5 cm thick soil layer, that contained also less compacted soil.

4.3 Surface roughness correction factor

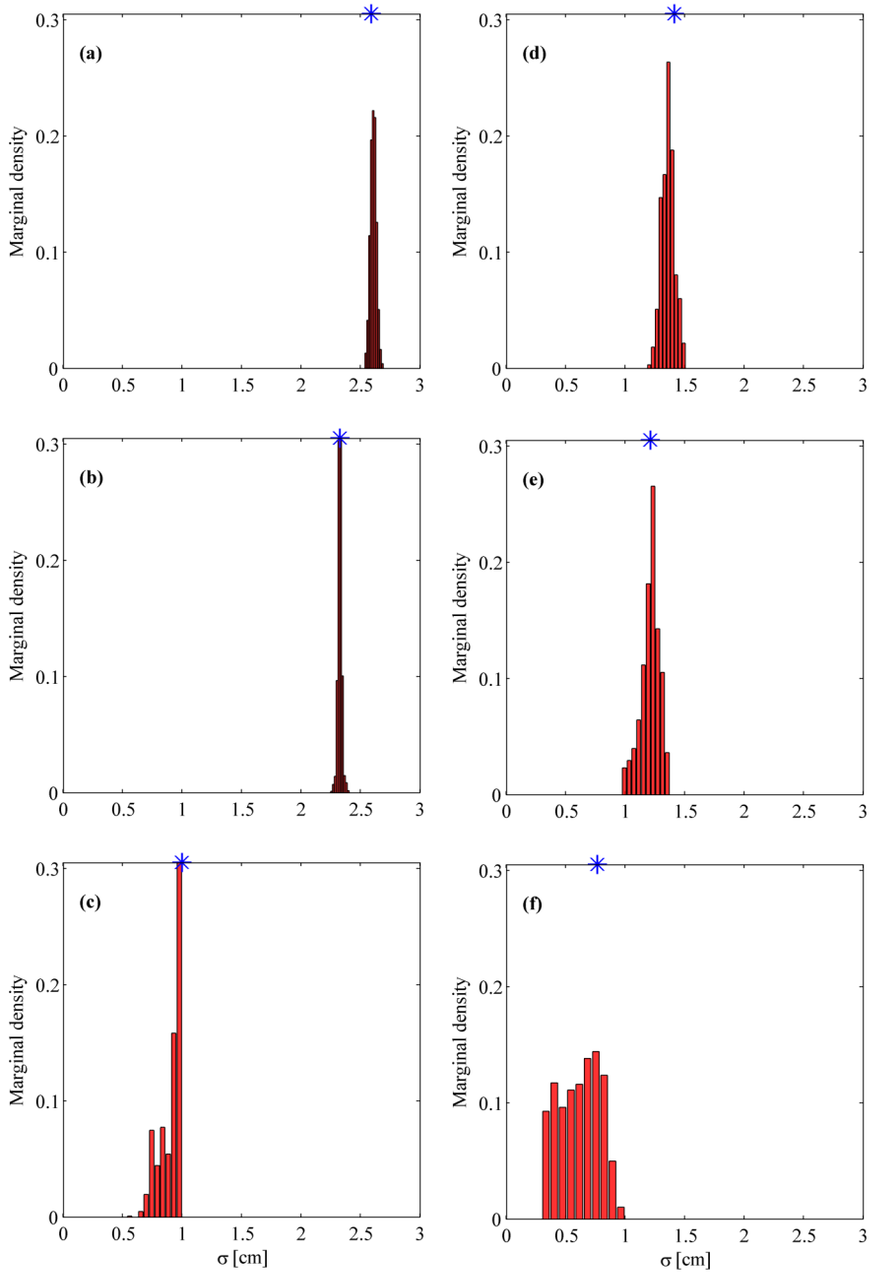

Figure IV.8 Histograms of the marginal posterior distributions of surface roughness parameter σ for periods DOY 92-120 (a-c) and DOY 158-186 (d-f) for tilled plot (a, d), seedbed plot (b, e) and compacted plot (c, f). The star represents the σ parameter in the parameter set with the highest likelihood.

The root mean square roughness height σ was calculated from the profile lines for all three plots. In Figure IV.8, the histograms of the marginal distributions of the inversely estimated roughness parameter σ from L-band radiometer measurements are given for two periods (DOY 92-120 (Figure IV.8 (a-c)) and DOY 158-186 (Figure IV.8 (d-f)).

In Table IV.4, inverted σ using the SCE-UA and the $DREAM_{zs}$ algorithms are given for all periods and plots. For the $DREAM_{zs}$, also the 95 % confidence intervals are given. In addition, σ derived from the laser profiler LMP-II measurements is given. The range of σ values for these measurements represents the range of σ values that were derived for the 124 profile lines in a plot.

Table IV.4 Dates of mechanical field preparations and of laser profiler measurements, root-mean-square-roughness height σ: measured with laser profiler and inverted with $DREAM_{zs}$ and SCE-UA from measured L-band brightness temperatures for different measurement periods and plots. Values given in parentheses are the minimal and the maximal σ_i along individual profiles.

Preparation	Meas.	Period	Measured σ (cm)	Inverted σ (cm)		
DOY	DOY	DOY	Tilled plot	SCE-UA	$DREAM_{zs}$	$DREAM_{zs}$ ranges
74	96	92-120	1.41 (0.97-1.79)	2.63	2.59	2.53-2.69
147	158	158-186	2.19 (1.97-2.48)	1.42	1.41	1.19-1.51
147	186	188-216	1.60 (1.33-1.86)	1.84	‘-‘	‘-‘
223	224	226-254	1.50 (1.05-1.82)	1.17	‘-‘	‘-‘
DOY	DOY	DOY	Seedbed plot	SCE-UA	$DREAM_{zs}$	$DREAM_{zs}$ ranges
74	96	92-120	0.78 (0.56-1.07)	2.48	2.46	2.33-2.66
147	158	158-186	0.99 (0.83-1.27)	1.22	1.21	1.00-1.37
147	186	188-216	0.78 (0.55-1.02)	1.47	‘-‘	‘-‘
223	224	226-254	1.21 (1.17-1.55)	1.06	‘-‘	‘-‘
DOY	DOY	DOY	Compacted plot	SCE-UA	$DREAM_{zs}$	$DREAM_{zs}$ ranges
74	96	92-120	0.57 (0.39-0.77)	0.79	0.99	0.53-1.00
147	158	158-186	0.17 (0.12-0.24)	0.64	0.77	0.30-0.99
147	186	188-216	0.40 (0.36-0.62)	0.89	‘-‘	‘-‘
223	224	226-254	0.45 (0.44-0.61)	0.82	‘-‘	‘-‘

The values of the inversely estimated roughness parameter for the tilled and the seedbed plots varied between 1.06 and 2.63 cm, the values of the roughness parameter for the compacted plot varied between 0.53 and 1 cm.

The mean value of σ obtained from laser profiler measurements varied for the different periods between 1.41 and 2.19 cm for the tilled plot, between 0.78 and 1.21 cm for the seedbed plot, and between 0.17 and 0.57 cm for the compacted plot. The ranges of inversely estimated σ values, provided with $DREAM_{zs}$ and SCE-UA, were for a certain plot very similar and the optimal parameters ranged between 1.17 and 2.63 cm for the tilled plot, between 1.06 and 2.48 cm for the seedbed plot, and between 0.64 and 0.99 cm for the compacted plot. For a certain plot, the range of inversely estimated σ corresponded fairly well with the range of directly measured σ,

although the inversely estimated σ of the compacted plot were somewhat larger than the directly measured σ. However, the variation of σ between different periods was not congruent for the directly and inversely estimated roughness parameters. The range of the directly estimated σ in the different profiles due to plot heterogeneity and the uncertainty of the inversely estimated σ is one reason for this inconsistency. The range of the 95 % confidence intervals of the inverted σ using $DREAM_{ZS}$ is about 0.3 cm for the tilled plot, 0.4 cm for the seedbed plot and up to 0.7 cm for the compacted plot. Therefore, the inversely estimated roughness parameters can be considered to be significantly larger for the seedbed and tilled plots than for the compacted plot. For the tilled and seedbed plot, the inverted σ for the dry period (DOY 92-120) is significantly larger than for the three other periods. The uncertainty intervals obtained by $DREAM_{ZS}$ indicate that the differences in σ between the other three periods are not significant. Another reason for the inconsistency is that the directly measured σ represents the roughness at one specific time. However, the roughness of the soil surface changes during a 28-day period, especially due to the impact of rain. The inversely estimated σ value represents an 'effective' surface roughness for the entire period and may hence be different from the surface roughness that is measured at a specific time (Dimitrov et al., 2014). Finally, it should be mentioned that the roughness correction model (Eq. [IV.V]) is a semi-empirical model so that fitted and directly measured σ may differ.

Despite all of the restrictions, mentioned above, our results show that σ can be estimated when using the inversion routine, i.e. the σ was inversely estimated together with all hydraulic parameters from L-band brightness temperature and it was in the same order of magnitude as directly measured σ.

4.4 Retrieved and in situ measured soil moisture content

In this section, we investigate whether the differences in soil hydraulic properties that are derived from L-band brightness temperature measurements from plots with different tillage are consistent with differences in soil moisture contents and dynamics that are measured in the different plots. Therefore, we compare soil moisture that is measured by in-situ sensors at 2 cm depth with 'retrieved' soil moisture contents, i.e. soil moisture contents that are simulated at 2 cm depth using HYDRUS 1D and the inversely estimated soil hydraulic parameters that are derived from L-band brightness temperatures.

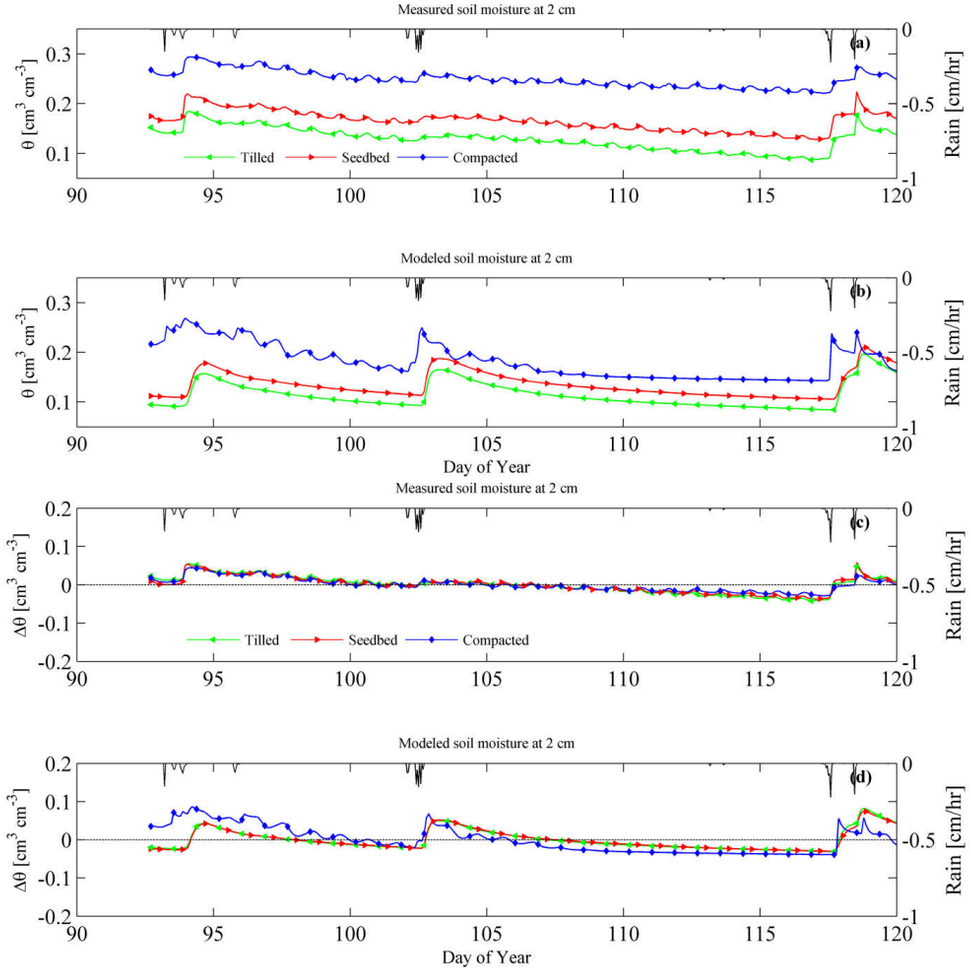

Figure IV.9 Time series of volumetric soil moisture contents at 2 cm for tilled, seedbed and compacted plots: measured with soil moisture sensors (a) and retrieved from L-band brightness temperatures (b). Deviations from averaged moisture contents during a period: measured (c) and modeled (d).

Figure IV.9 (a-b) and Figure IV.10 (a-b) show the measured and retrieved soil moisture contents at 2 cm for the tilled (green line), seedbed (red line), and compacted plot (blue line) for period DOY 92-120 and DOY 158-186, respectively. In Figure IV.9 (c, d) and Figure IV.10 (c, d), the deviation of the measured and retrieved moisture contents from the average measured/retrieved moisture content in a plot during the periods DOY 92-120 (Figure IV.9) and DOY 158-186 (Figure IV.10) are shown. The results for the other two investigated periods are presented in Figure IV.11 (period DOY 188-216) and in Figure IV.12 (period DOY 226-254). In order to facilitate the comparison between retrieved and measured soil moisture contents in the

different plots and for the different periods, the average measured water contents during a period are plotted versus the averaged retrieved water contents in Figure IV.13 (a) and the standard deviations of the measured versus retrieved soil moisture contents in Figure IV.13 (b).

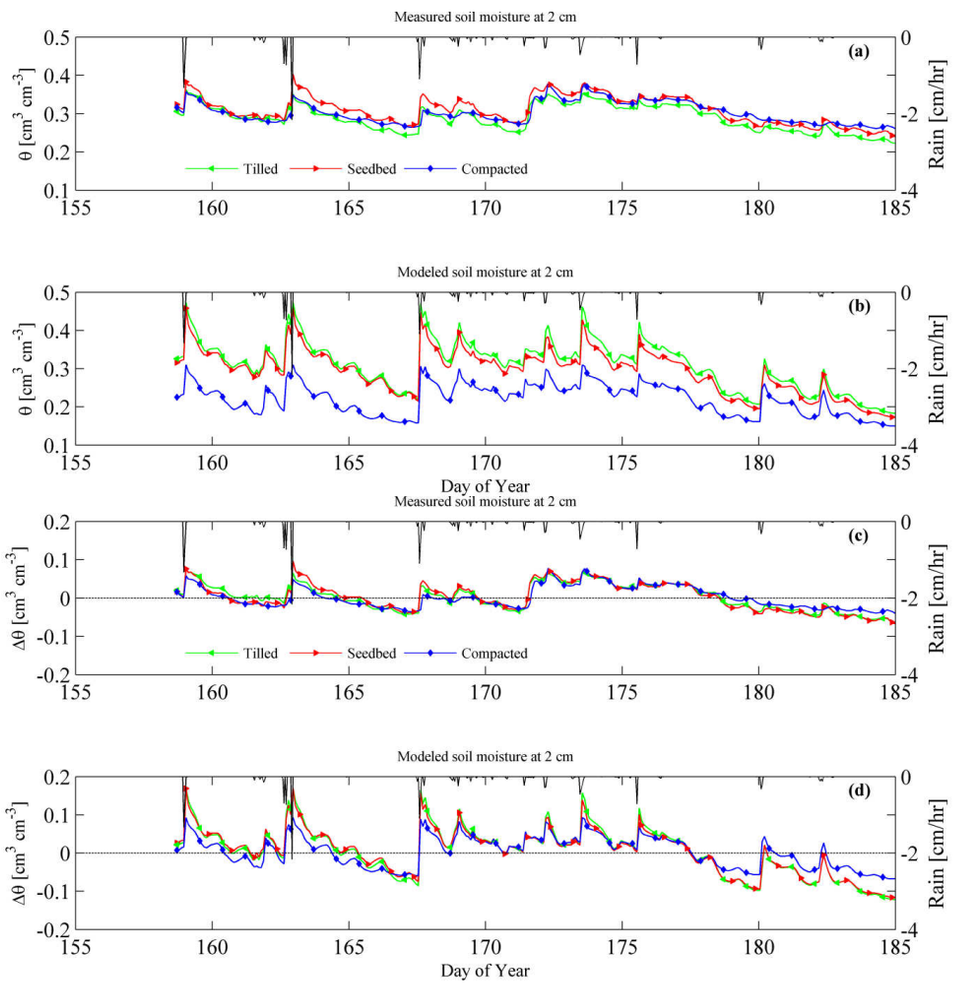

Figure IV.10 Time series of volumetric soil moisture contents at 2 cm for tilled, seedbed, and compacted plots: measured with soil moisture sensors (a) and retrieved from L-band brightness temperatures (b). Deviations from averaged moisture contents during a period: measured (c) and modeled (d).

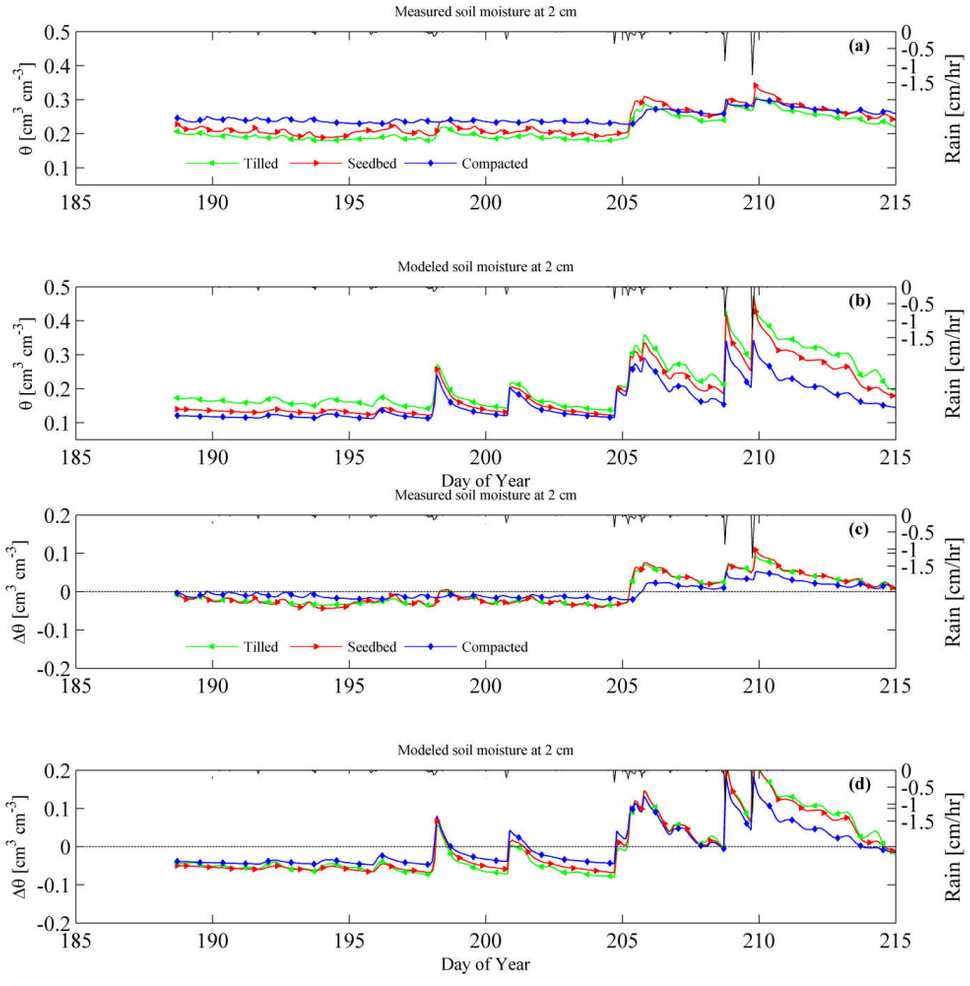

Figure IV.11 Time series of volumetric soil moisture contents at 2 cm for tilled, seedbed and compacted plots: measured with soil moisture sensors (a) and retrieved from L-band brightness temperatures (b). Deviations from averaged moisture contents during a period: measured (c) and modeled (d).

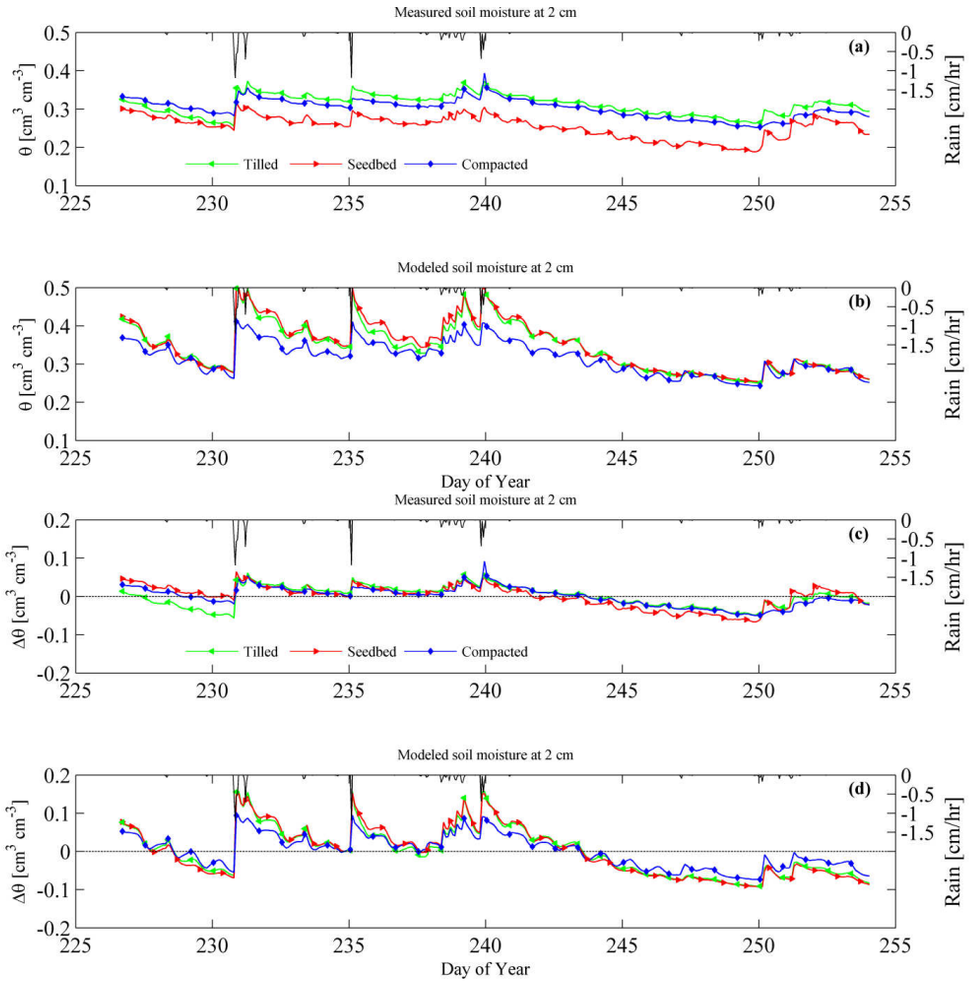

Figure IV.12 Time series of volumetric soil moisture contents at 2 cm for tilled, seedbed, and compacted plots: measured with soil moisture sensors (a) and retrieved from L-band brightness temperatures (b). Deviations from averaged moisture contents during a period: measured (c) and modeled (d).

Figure IV.13 (a) shows that the points of the average retrieved versus measured soil moisture fall around the one-to-one line. The wetter periods (DOY 158-186 and DOY 226-254) have both higher measured and retrieved water contents than the drier periods (DOY 92-120, DOY 188-216). Rainfall amounts and potential evaporation are given in Table IV.5. Except for the dry period DOY 92-120, in-situ measured and retrieved averaged water contents during a certain period did not show consistent differences between different plots. For the retrieved water contents and except for the dry period DOY 92-120, the compacted plot had lower averaged water contents than the tilled and seedbed plots, which had similar water contents. But this was not confirmed by the in-situ measurements. Only for the dry period, DOY 92-120, the retrieved and in-situ measured averaged soil moisture contents showed consistent differences between the different plots.

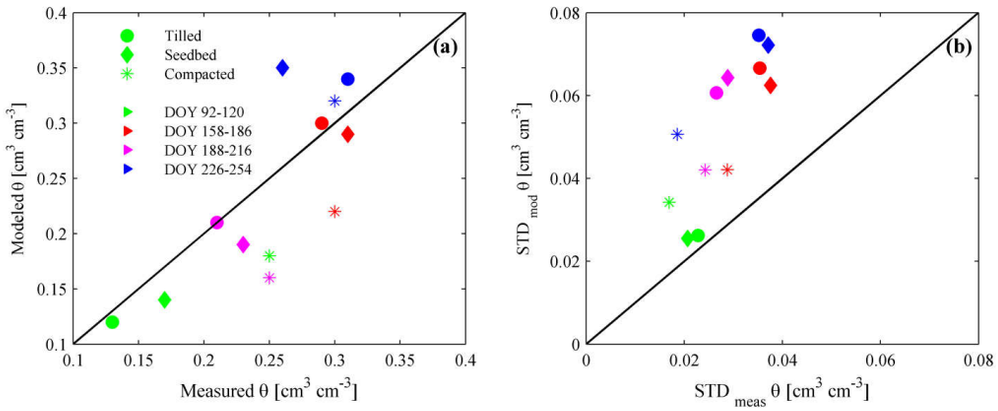

Figure IV.13 Averages over time during an investigation period of modeled and measured soil moisture contents at 2 cm depth (a) and standard deviations of the variations over time during an investigation period of measured and modeled soil moisture contents (b). The symbols represent the plots and the colors the different periods.

Looking at the dynamics of the soil moisture or the variations of the soil moisture with respect to the temporal average both the in-situ measured and the retrieved soil moisture contents show that this variation is smaller for the compacted than for the tilled and seedbed plots, except for the dry period (see Figure IV.9 (c-d), Figure IV.10 (c-d), Figure IV.11 (c-d), Figure IV.12, (c-d), Figure IV.13 (b)). Especially after rain events (e.g. DOY 102.5, DOY 162.5, DOY 167.5, DOY 230.9), these variations were much stronger for the tilled and the seedbed plot than for the

compacted plot. The variations of the retrieved soil moisture contents are directly linked to the variations of TBH (Figure IV.3) and normalized TBH values (Figure IV.5). The changes of the TBH values after rain events are much smaller for the compacted than for the tilled and seedbed plots (e.g. DOY 102.5, DOY 117.6, DOY 230.9).

However, the variations of the retrieved soil moisture contents are considerably larger than that of the in-situ measured soil moisture contents (all points are above the one-to-one line in Figure IV.13 (b)). The 5TE sensors were not able to register the large changes in soil moisture after the rain events that correspond with drastic decreases in TBH by more than 50 K after main rain events (e.g. DOY 117.5, DOY 204.7, DOY 230.9). The maximum changes of the measured soil moisture at 2 cm were ~ 0.1 cm^3 cm^{-3} whereas retrieved soil moisture contents increased by more than 0.2 cm^3 cm^{-3}. Especially when the soil was saturated, the sensors did not show a strong reaction after rain events. A similar behavior and reaction of soil moisture sensors was already observed by (Escorihuela et al., 2010) and (Mialon et al., 2012), whereby (Mialon et al., 2012) found that the radiometer showed also a faster response after rainfall compared to the sensors.

4.5 Soil surface temperature and evaporation

In Figure IV.14 (a, c) the differences in measured with the IR camera soil surface temperatures between the seedbed and compacted plot, and between the tilled and compacted plot are shown for periods DOY 95-110 and DOY 168-180, respectively. A positive difference refers to a cooler compacted than tilled or seedbed plot. For the dry period DOY 95-110, the differences in temperature show a clear diurnal fluctuation with maximal temperature differences of + 2.8 K around noon and minimal differences of – 1.7 K at predawn. For the wet period, clear diurnal fluctuations in temperature differences were observed at the end of the investigated period (at DOY 178, 179) but now, negative temperature differences (compacted plot is warmer than seedbed and tilled plots) of -1.4 K were observed around noon. The observed temperature differences during the two periods were smaller than almost 4 K differences, between tilled plots and no-tilled presented by (Richard and Cellier, 1998) (4 K) or by (Moroizumi and Horino, 2002) (5.5 K). This may be due to the fact that the climatological conditions in which we investigated the different behaviour of the differently tilled plots were wetter than in those studies. Besides differences in thermal soil properties between plots with different porosity, soil water content and bulk density, also differences in soil evaporation contributes to a large extent to differences in soil surface temperature. In order to investigate whether the observed surface temperature

differences are consistent with differences in simulated soil evaporation, in Figure IV.14 (b and d), the potential evaporation and the simulated actual evaporation from the soil surfaces are shown.

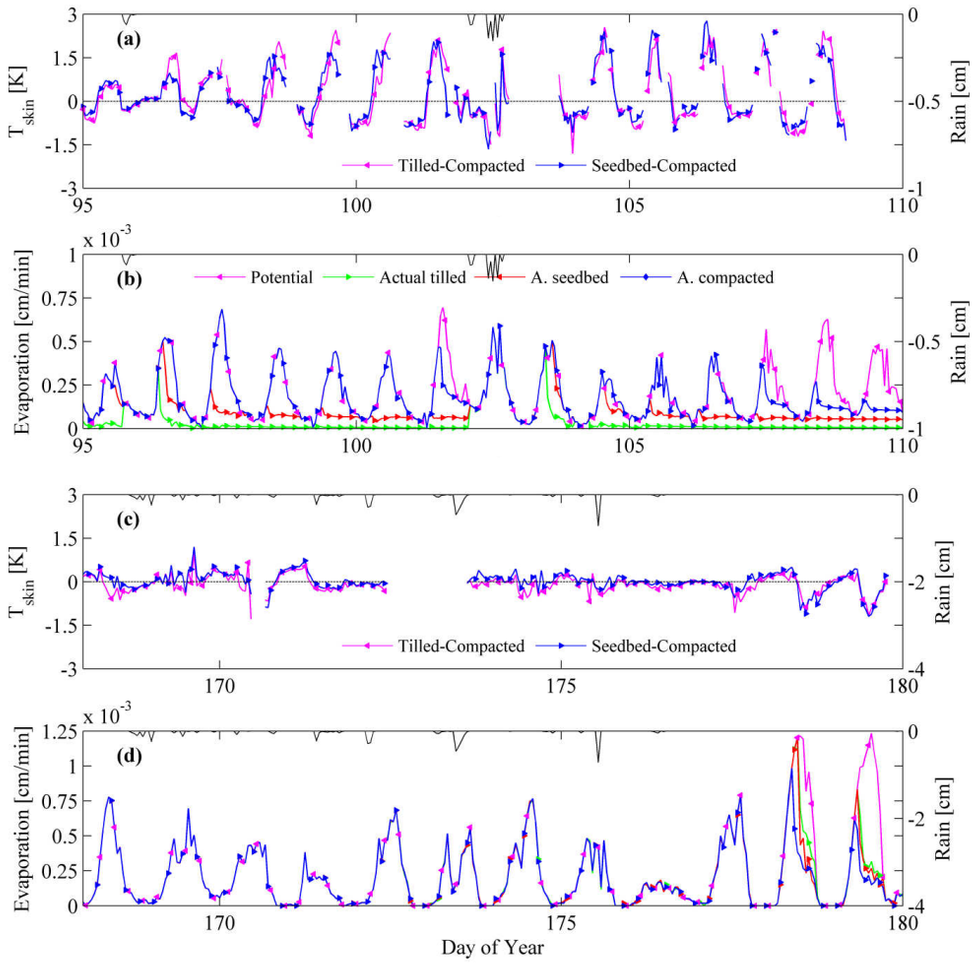

Figure IV.14 Time series of differences of measured infrared temperature between the tilled and compacted plot and between the seedbed and compacted plot for period DOY 95-110 (a) and period DOY 165-180 (c). Potential evaporation and actual evaporation simulated with HYDRUS using the DREAM$_{ZS}$ parameter set with the highest likelihood for tilled, seedbed and compacted plots (b and d).

The potential evaporation represents the evaporation from sufficiently wet soil surfaces, i.e. the soil surface is sufficiently wet so that it can supply the evaporative demand from the atmosphere by a liquid water flow towards the evaporating surface. When evaporation equals potential evaporation, the evaporation is said to be in stage I (Jury and Horton, 2004). The

potential evaporation was assumed to be the same for the three different plots (i.e. we did not include the effects of the differences in soil surface roughness on the aerodynamic resistance and consequently on the potential evaporation) so that during stage I, the simulated evaporation from the plots was identical. During the wet period, evaporation was in stage I for the three plots from DOY 168 until DOY 177. For the dry period, only during the rainy day at DOY 102, evaporation was at stage I for the three plots. On days when the three plots were in stage I evaporation, the differences in surface temperatures between the different plots did not show a clear diurnal signal. When the soil surface gets dry and cannot supply the evaporation rate that is 'demanded' by the atmosphere, the evaporation shifts to phase II evaporation when the evaporation rate is controlled by the soil hydraulic properties. The soil hydraulic properties determine how the evaporation rate decreases during phase II and the time when the evaporation regime shifts from phase I to phase II. Differences in soil hydraulic properties between the different plots lead to different times at which evaporation shifts from phase I to phase II and to different evaporation rates when one or two of the compared plots are in phase II. Since differences in evaporation go along with differences in evaporative cooling, differences in evaporation should lead to differences in soil surface temperatures between the different plots. During the dry period, the simulated evaporation rates of the compacted plot were on most days higher than those of the seedbed and tilled plots. During the wet period, the simulated evaporation rates were smaller in the compacted than in the seedbed and tilled plots at the end of the considered period. The differences in simulated evaporation were consistent with the differences in observed surface temperatures. This demonstrates that differences in soil hydraulic properties between the different plots that were derived from L-band brightness temperatures can be used to predict the different hydraulic behavior of plots with different surface structures.

In order to demonstrate the effect of the different soil surface structures on the soil water balance, we listed in Table IV.5 the simulated cumulative actual evaporation losses from the different plots for the different time periods together with the rainfall and potential evaporation amounts during these periods. For periods DOY 92-120 and DOY 188-216, rainfall was smaller than potential evaporation. Only for the driest period DOY 92-120, the simulated evaporation loss from the compacted plot was considerably higher than that of the tilled and seedbed plots. For the periods DOY 158-186 and DOY 188-216, the simulated evaporation losses for the compacted plot were lower than those of the seedbed and tilled plots. These results confirm other studies showing that tillage may have opposite effects on soil water conservation depending on the meteorological conditions. Substantially higher evaporation rates on a compacted plot compared to several differently tilled plots have also been reported by (Sillon et al., 2003) and

these results were explained by a higher unsaturated hydraulic conductivity in the dense plot. The results of (Rydberg, 1990) furthermore showed that stage I was shorter on the soil with stable aggregates. The mechanisms described above for period DOY 95-110 were strongly different for period DOY 168-180 where stage I lasted longest and actual evaporation was highest on the tilled plot. Similar results were obtained by (Mwendera and Feyen, 1994) and (Hatfield et al., 2001) who measured a higher evaporation on a ploughed plot shortly after tillage. Due to the large stable aggregates and more large pores and higher saturated water content in the tilled and seedbed plots more water could infiltrate. As a result more water was available for evaporation on the tilled plot leading to a longer stage I evaporation.

Table IV.5 Potential evaporation and actual evaporation simulated with HYDRUS-1D using the $DREAM_{ZS}$ or SCE-UA parameter set with the highest likelihood for tilled, seedbed, and compacted plot.

Preparation DOY	Period	Model	Total Rain (cm)	Eto (cm)	Tilled Eta (cm)	Seedbed Eta (cm)	Compacted Eta (cm)	Tilled Eto-Eta (cm)	Seedbed Eto-Eta (cm)	Compacted Eto-Eta (cm)
74	92-120	SCE-UA	1.49	8.08	1.56	1.57	5.73	6.52	6.51	2.35
		$DREAM_{ZS}$		8.08	1.59	1.55	5.77	6.49	6.53	2.32
147	158-186	SCE-UA	13.32	9.52	8.58	8.58	7.92	0.93	0.94	1.60
		$DREAM_{ZS}$		9.52	8.64	8.50	7.81	0.87	1.02	1.71
147	188-216	SCE-UA	6.61	8.22	6.07	4.52	3.89	2.15	3.70	4.34
223	226-254	SCE-UA	9.01	8.40	7.36	7.07	7.85	1.04	1.33	0.55

5 Summary and conclusion

L-band brightness temperatures could be used to infer differences in soil hydraulic properties and surface roughness of plots with different tillage and compaction. The fact that both surface roughness and soil hydraulic properties can be derived from time series of TBH can be made clear using normalized brightness temperatures. By comparing modeled and simulated normalized brightness temperatures also changes in surface structure, which was not included in the model, could be identified. In order to consider changes in surface roughness or hydraulic parameters over time in the model, data assimilation methods (Montzka et al., 2013) could be used.

The derived roughness parameter from inversion of TBHs corresponded fairly well with the standard deviation of the surface heights that were measured using a laser profiler. The inverted

parameters of the hydraulic functions that are related to hydraulic properties of saturated soil were very uncertain. This is due to the highly nonlinear behavior of the hydraulic functions close to saturation and the fact that saturated conditions were seldom reached during the monitoring periods. However, the uncertainty of the hydraulic functions decreases considerably when pressure heads become slightly negative. The inverted hydraulic functions differed between the tilled, compacted and seedbed treated soil plots. The L-band derived hydraulic functions of the tilled and seedbed plots showed a higher water content and higher hydraulic conductivity than the compacted plots for relatively high pressure heads. However, the hydraulic conductivity decreased rapidly with decreasing pressure head in the tilled and seedbed plots. The hydraulic functions of the tilled and seedbed plots were better described by assuming a bi-modal pore size distribution. This was in line with the hydraulic functions that were derived from soil samples taken from the plots. However, the hydraulic functions of the soil samples did not show such distinct differences between the different plots as the hydraulic functions that were inverted from TBH values. The TBH measurements respond to the changes in water contents of a thin surface layer (e.g. Dimitrov et al., 2014). We speculate that the compaction did not affect the upper 5 cm of the soil profile to the same extent as the upper few millimeters which are seen by the radiometer.

In order to validate the derived soil hydraulic functions, simulated water contents were compared with in-situ measurements obtained from soil water content sensors. The differences in average water contents between the different plots during a period were not congruent with the in-situ measurements. However, the difference in dynamics of soil moisture contents between the different plots, with the tilled and seedbed plots showing larger variations in soil moisture than the compacted plot was confirmed by in-situ soil moisture measurements. But, in-situ measurements did not show that large variation of water contents over time. Whether the in-situ soil moisture sensors better represent the field plot averaged water contents than the simulated water contents that were derived from L-band TBH values remains an open question. First, the installation of soil moisture sensors disturbs the soil around the sensor which influences the sensor readings. The soil may be compacted around the sensor (Ghezzehei, 2008) or gaps, holes and cracks may be created when inserting the probes. Second, due to spatial variability, the averaged value of a limited number of in-situ sensors may not be representative for the average water content in a plot. Third, the simulated changes in water contents after a rainfall event are based on the Richards equation which solves a mass balance equation. Therefore, the considerably smaller changes in water contents that were measured by the in-situ sensors are not consistent with the amount of rainfall. It must be noted however that non-equilibrium

phenomena such as preferential flow and runoff (which was not observed) may lead to much smaller changes in soil moisture contents at the soil surface than what would be expected using a flow model that assumes instantaneous equilibrium such as the Richards equation (e.g. Neuweiler et al., 2012; Schluter et al., 2012).

When looking at differences in soil evaporation between the plots that were simulated using hydraulic parameters derived from L-band TBH measurements, it was found that whether the compacted or tilled/seedbed plots evaporated more depended on the weather conditions during the considered period. The differences in simulated evaporation were consistent with differences in measured surface temperatures, which also give some confidence in the derived soil hydraulic functions.

6 Acknowledgments

The presented in this study work is part of the research unit FOR 1083 MUSIS (Multi-Scale Interfaces in Unsaturated Soil) and TERENO TERrestrial ENviromental Observatories. The authors are thankful to Prof. Dr. J.A. Vrugt for his assistance with the implementation and the use of the $DREAM_{zs}$ code. We thank Dr. K. Z. Jadoon, Dr. M. Schwank, Dr. L. Weihermueller, for the support during the development of the inversion approach. We thank the team of H. Jagdfeld (Central Institute of Technology, Research Centre Jülich) for the development of the radiometer tower. M. Dimitrov thanks Dr. J. Bikowski and Dr. I. Mladenova for the implementation of the models.

V Synopsis

1 Summarizing conclusions

In this thesis measured L-band brightness temperature data from bare soil plots with different soil structure were used for inverse estimation of soil hydraulic properties. L-band brightness temperature data from the clear sky were also used for calibration algorithm development.

A new algorithm for sky calibration was proposed and tested to derive effective transmissivities that account for feed cable loss effects and variations in radiometer gain due to air temperature changes for two L-band radiometers, both of them with built-in noise sources for internal calibration. The effective transmissivities depend strongly on the air temperature and decrease with increasing air temperature or the L-band radiometer JÜLBARA. Such strong dependence was not observed for the L-band radiometer ELBARA II.

Another research topic of this study was the estimation of soil hydraulic properties, soil moisture and soil surface roughness from measured L-band brightness temperature data for three different bare soil structure types. Time series of soil moisture, soil temperature, soil surface temperature and L-band brightness temperature of differently prepared bare soil plots were collected. One plot was tilled, one was tilled and harrowed (seedbed plot), and one plot was after harrowing levelled and compacted (compacted plot). Five different 28-days measurement periods were used to investigated different meteorological and soil hydrologic conditions. From measured L-band temperatures hydraulic parameters and a roughness correction parameter were inversely estimated for all three investigated plots.

In the coupled inversion routine, presented in this study, a hydrological model, a radiative transfer model, a surface roughness correction model and a radiative transfer model were combined with a global optimization algorithm. For the hydrological model, two models that describe the soil hydraulic properties were considered: the uni-modal Mualem van Genuchten and bi-modal Durner models. For the radiative transfer, a coherent radiative transfer model and the Fresnel model for an averaged soil permittivity of a layer between 0 and 2 cm and between 0 and 5 cm were considered. Two different optimization techniques, namely $DREAM_{zs}$ and SCE-UA, were implemented to estimate not only the optimal solution, but also to provide information about the posterior distribution of the estimated parameters.

All inversely estimated parameters and simulated soil moisture, as well as the simulated L-band brightness temperatures were compared for all three investigated plots with the corresponding field measured values or laboratory estimated parameters. The calculated

RMSD values between the measured and the simulated L-band brightness temperatures, as well as between the measured and the inversely estimated soil moisture values were calculated for all plots and periods. It was found that the CRTM in combination with the DBM provided the lowest RMSD values when comparing L-band brightness temperatures. Results with the Fresnel equation for 0 – 2 cm layer were better than results with Fresnel equation for 0 – 5 cm layer and were very similar to the results with CRTM. The inversely derived roughness parameter for the investigated plots corresponded fairly well with the standard deviation of the surface heights, measured on the field. The inversely estimated hydraulic parameters differed between the tilled, the seedbed and the compacted plots. The inversely derived hydraulic functions were better described when using the Durner bi-modal model and for the tilled and the seedbed plots showed higher water content and higher hydraulic conductivity for higher pressure head values than the compacted plot. However, using the optimisation algorithm $DREAM_{zs}$ it was shown that the inverted parameters were very uncertain.

Different soil evaporation values were estimated for the different plots using the hydraulic parameters derived from the L-band brightness temperatures. It was found that whether the compacted or the tilled and seedbed plots evaporated more depended on the weather conditions during the investigated period.

2 Outlook

This study showed that L-band brightness temperatures from bare soil plots with different soil structures could be used to estimate inversely soil hydraulic parameters and roughness correction parameter.

However, this study was based only on field measurements over bare soil plots with the same soil texture. L-band brightness temperature measured on bare soils with different soil texture may provide information for soil hydraulic parameters and can be used for soil moisture retrieval. Overall, the measured L-band brightness temperatures differed between the investigated plots and periods, especially during drying periods, which lead to differences in the inversely estimated hydraulic parameters.

Using satellite or aircraft L-band brightness temperature data the presented in this study inverse procedure may be implemented for larger areas or scales. The models, used within the presented coupled inversion, may also be replaced with other existing models.

Such complex study in the future needs to be strongly supported by precisely organized field measurements campaigns (e.g. surface soil moisture, surface roughness, meteorological

data) and could also be tested over more differently tilled measurement plots. A combined analysis of L-band data from different scales (e.g. field, airborne and satellite scales), can provide a lot of new knowledge for the soil surface state and can be useful for different scientific communities.

References

Allen R.G., L.S. Pereira, D. Raes and M. Smith. 1998. Crop evapotranspiration-Guidelines for computing crop water requirements-FAO Irrigation and drainage paper 56. FAO, Rome. 300:6541.

Bass M., E. Van Stryland, D. Williams and W. Wolfe. 1996. Handbook of Optics McGraw-Hill.

Bikowski J., J.A. Huisman, J.A. Vrugt, H. Vereecken and J. van der Kruk. 2012. Integrated analysis of waveguide dispersed GPR pulses using deterministic and Bayesian inversion methods. Near Surface Geophysics. 10:641-652. doi:10.3997/1873-0604.2012041.

Bindlish R., T.J. Jackson, A. Gasiewski, B. Stankov, M. Klein, M.H. Cosh, I. Mladenova, C. Watts, E. Vivoni, V. Lakshmi, J. Bolten and T. Keefer. 2008. Aircraft based soil moisture retrievals under mixed vegetation and topographic conditions. Remote Sensing of Environment. 112:375-390. doi:10.1016/j.rse.2007.01.024.

Bogena H., M. Herbst, J. Huisman, U. Rosenbaum, A. Weuthen and H. Vereecken. 2010. Potential of wireless sensor networks for measuring soil water content variability. Vadose Zone Journal. 9:1002-1013. doi:10.2136/vzj2009.0173.

Burke E.J., R.J. Gurney, L.P. Simmonds and P.E. O'Neill. 1998. Using a modeling approach to predict soil hydraulic properties from passive microwave measurements. Ieee Transactions on Geoscience and Remote Sensing. 36:454-462. doi:10.1109/36.662729.

Camillo P.J., P.E. Oneill and R.J. Gurney. 1986. Estimating soil hydraulic parameters using passive microwave data. IEEE Transactions on Geoscience and Remote Sensing. 24:930-936. doi:10.1109/tgrs.1986.289708.

Carminati A., A. Kaestner, R. Hassanein, O. Ippisch, P. Vontobel and H. Fluhler. 2007a. Infiltration through series of soil aggregates: Neutron radiography and modeling. Advances in Water Resources. 30:1168-1178. doi:10.1016/j.advwatres.2006.10.006.

Carminati A., A. Kaestner, H. Fluhler, P. Lehmann, D. Or, E. Lehmann and M. Stampanoni. 2007b. Hydraulic contacts controlling water flow across porous grains. Physical Review E. 76. doi:10.1103/PhysRevE.76.026311.

Carminati A., A. Kaestner, O. Ippisch, A. Koliji, P. Lehmann, R. Hassanein, P. Vontobel, E. Lehmann, L. Laloui, L. Vulliet and H. Fluhler. 2007c. Water flow between soil

aggregates. Transport in Porous Media. 68:219-236. doi:10.1007/s11242-006-9041-z.

Chang D.H. and S. Islam. 2000. Estimation of soil physical properties using remote sensing and artificial neural network. Remote Sensing of Environment. 74:534-544. doi:10.1016/s0034-4257(00)00144-9.

Chanzy A., M. Mumen and G. Richard. 2008. Accuracy of top soil moisture simulation using a mechanistic model with limited soil characterization. Water Resources Research. 44. doi:10.1029/2006wr005765.

Choudhury B.J., T.J. Schmugge and T. Mo. 1982. A parameterization of effective soil temperature for microwave emission. Journal of Geophysical Research-Oceans and Atmospheres. 87:1301-1304. doi:10.1029/JC087iC02p01301.

Choudhury B.J., T.J. Schmugge, A. Chang and R.W. Newton. 1979. Effect of surface roughness on the microwave emission from soils. Journal of Geophysical Research-Oceans and Atmospheres. 84:5699-5706. doi:10.1029/JC084iC09p05699.

Christiansen L., E.B. Haarder, A.B. Hansen, M.C. Looms, P.J. Binning, D. Rosbjerg, O.B. Andersen and P. Bauer-Gottwein. 2011. Calibrating vadose zone models with time-lapse gravity data. Vadose Zone Journal. 10:1034-1044. doi:10.2136/vzj2010.0127.

Clothier E. and E. Brent. 2001. Infiltration, soil and environmental analysis, physical methods, edited by Smith and Mullins, Marcel Dekker, Inc., New York, USA.

Cobos D.R. and C. Chambers. 2010. Calibrating ECH2O soil moisture sensors.

Dane J.H., C. Topp, G.S. Campbell, R. Horton, W.A. Jury, D.R. Nielsen, H.M. van Es, P.J. Wierenga and G.C. Topp. 2002. Part 4-Physical methods, In: C. Topp (Ed.), Methods of soil analysis, Madison, WI.

de Rosnay P., J.C. Calvet, Y. Kerr, J.P. Wigneron, F. Lemaitre, M.J. Escorihuela, J.M. Sabater, K. Saleh, J.L. Barrie, G. Bouhours, L. Coret, G. Cherel, G. Dedieu, R. Durbe, N.E.D. Fntz, F. Froissard, J. Hoedjes, A. Kruszewski, F. Lavenu, D. Suquia and P. Waldteufel. 2006. SMOSREX: A long term field campaign experiment for soil moisture and land surface processes remote sensing. Remote Sensing of Environment. 102:377-389. doi:10.1016/j.rse.2006.02.021.

Delahaye J.Y., P. Golé and P. Waldteufel. 2002. Calibration error of L-band sky‐looking ground‐based radiometers. Radio Science. 37:11-1-11-11. doi:10.1029/2001RS002490.

Dimitrov M., K. Kostov, F. Jonard, K. Jadoon, M. Schwank, L. Weihermuller, N. Hermes, J. Vanderborght and H. Vereecken. 2012. New improved algorithm for sky calibration of L-band radiometers JÜLBARA and ELBARA II. Microwave Radiometry and Remote Sensing of the Environment (MicroRad), 2012 12th Specialist Meeting on.1-4. doi:10.1109/MicroRad.2012.6185259.

Dimitrov M., J. Vanderborght, K.G. Kostov, K.Z. Jadoon, L. Weihermuller, T.J. Jackson, R. Bindlish, Y. Pachepsky, M. Schwank and H. Vereecken. 2014. Soil Hydraulic Parameters and Surface Soil Moisture of a Tilled Bare Soil Plot Inversely Derived from L-Band Brightness Temperatures. Vadose Zone Journal. 13. doi:10.2136/vzj2013.04.0075.

Duan Q., S. Sorooshian and V.K. Gupta. 1994. Optimal use of the SCE-UA global optimization method for calibrating watershed models. Journal of Hydrology. 158:265-284. doi:10.1016/0022-1694(94)90057-4.

Duan Q.Y., S. Sorooshian and V. Gupta. 1992. Effective and Efficient Global Optimization for Conceptual Rainfall-Runoff Models. Water Resources Research. 28:1015-1031. doi:10.1029/91WR02985.

Duan Q.Y., V.K. Gupta and S. Sorooshian. 1993. Shuffled complex evolution approach for effective and efficient global minimization. Journal of Optimization Theory and Applications. 76:501-521. doi:10.1007/bf00939380.

Durner W. 1994. Hydraulic conductivity estimation for soils with heterogeneous pore structure. Water Resources Research. 30:211-223. doi:10.1029/93wr02676.

Durner W. and K. Lipsius. 2005. Determining soil hydraulic properties, In: M. G. Anderson (Ed.), Encyclopedia of Hydrological Sciences, John Wiley & Sons, Chichester.

Entekhabi D., E.G. Njoku, P.E. O'Neill, K.H. Kellogg, W.T. Crow, W.N. Edelstein, J.K. Entin, S.D. Goodman, T.J. Jackson, J. Johnson, J. Kimball, J.R. Piepmeier, R.D. Koster, N. Martin, K.C. McDonald, M. Moghaddam, S. Moran, R. Reichle, J.C. Shi, M.W. Spencer, S.W. Thurman, L. Tsang and J. Van Zyl. 2010. The Soil Moisture Active Passive (SMAP) Mission. Proceedings of the Ieee. 98:704-716. doi:10.1109/jproc.2010.2043918.

Escorihuela M., A. Chanzy, J. Wigneron and Y. Kerr. 2010. Effective soil moisture sampling depth of L-band radiometry: A case study. Remote Sensing of Environment. 114:995-1001. doi:10.1016/j.rse.2009.12.011.

Ghezzehei T.A. 2008. Errors in determination of soil water content using time domain reflectometry caused by soil compaction around waveguides. Water Resources Research. 44. doi:10.1029/2007wr006502.

Hatfield J.L., T.J. Sauer and J.H. Prueger. 2001. Managing soils to achieve greater water use efficiency. Agronomy journal. 93:271-280. doi:10.2134/agronj2001.932271x.

Hebrard O., M. Voltz, P. Andrieux and R. Moussa. 2006. Spatio-temporal distribution of soil surface moisture in a heterogeneously farmed Mediterranean catchment. Journal of Hydrology. 329:110-121. doi:10.1016/j.jhydrol.2006.02.012.

Hogue T.S., L. Bastidas, H. Gupta, S. Sorooshian, K. Mitchell and W. Emmerich. 2005. Evaluation and transferability of the Noah land surface model in semiarid environments. Journal of Hydrometeorology. 6:68-84. doi:10.1175/JHM-402.1.

Holmes T.R.H., P. de Rosnay, R. de Jeu, R.J.P. Wigneron, Y. Kerr, J.C. Calvet, M.J. Escorihuela, K. Saleh and F. Lemaitre. 2006. A new parameterization of the effective temperature for L band radiometry. Geophysical Research Letters. 33. doi:10.1029/2006gl025724.

Jackson T.J., P.E. Oneill and C.T. Swift. 1997. Passive microwave observation of diurnal surface soil moisture. Ieee Transactions on Geoscience and Remote Sensing. 35:1210-1222. doi:10.1109/36.628788.

Jackson T.J., D.M. Le Vine, A.Y. Hsu, A. Oldak, P.J. Starks, C.T. Swift, J.D. Isham and M. Haken. 1999. Soil moisture mapping at regional scales using microwave radiometry: The Southern Great Plains Hydrology Experiment. Ieee Transactions on Geoscience and Remote Sensing. 37:2136-2151. doi:10.1109/36.789610.

Jonard F., L. Weihermuller, K.Z. Jadoon, M. Schwank, H. Vereecken and S. Lambot. 2011. Mapping Field-Scale Soil Moisture With L-Band Radiometer and Ground-Penetrating Radar Over Bare Soil. Ieee Transactions on Geoscience and Remote Sensing. 49:2863-2875. doi:10.1109/tgrs.2011.2114890.

Jury W.A. and R. Horton. 2004. Soil physics John Wiley & Sons.

Kerr Y.H., P. Waldteufel, J.P. Wigneron, S. Delwart, F. Cabot, J. Boutin, M.J. Escorihuela, J. Font, N. Reul, C. Gruhier, S.E. Juglea, M.R. Drinkwater, A. Hahne, M. Martin-Neira and S. Mecklenburg. 2010. The SMOS Mission: New Tool for Monitoring Key Elements of the Global Water Cycle. Proceedings of the Ieee. 98:666-687. doi:10.1109/jproc.2010.2043032.

Kostov K.G. and B.I. Vichev. 1995. Near-surface moisture profile effects on the microwave emission of bare soils. Igarss '95. Geoscience and Remote Sensing Symposium.:1991-1993. doi:10.1109/IGARSS.1995.524088.

Laloy E. and J.A. Vrugt. 2012. High dimensional posterior exploration of hydrologic models using multiple‐try DREAM (ZS) and high‐performance computing. Water Resources Research. 48. doi:10.1029/2011WR010608.

Mattikalli N.M., E.T. Engman, L.R. Ahuja and T.J. Jackson. 1995. Estimating soil properties from microwave measurements of soil moisture. Remote Sensing for Agriculture, Forestry, and Natural Resources. 2585:89-101. doi:10.1117/12.227172.

Mattikalli N.M., E.T. Engman, T.J. Jackson and L.R. Ahuja. 1998. Microwave remote sensing of temporal variations of brightness temperature and near-surface soil water content during a watershed-scale field experiment, and its application to the estimation of soil physical properties. Water Resources Research. 34:2289-2299. doi:10.1029/98wr00553.

Matzler C., D. Weber, M. Wuthrich, K. Schneeberger, C. Stamm, H. Wydler and H. Fluhler. 2003. ELBARA, the ETH L-band radiometer for soil-moisture research:3058-3060. doi:10.1109/IGARSS.2003.1294682.

Mauser W. and S. Schadlich. 1998. Modelling the spatial distribution of evapotranspiration on different scales using remote sensing data. Journal of Hydrology. 213:250-267. doi:10.1016/S0022-1694(98)00228-5.

Mialon A., J.-P. Wigneron, P. De Rosnay, M.J. Escorihuela and Y.H. Kerr. 2012. Evaluating the L-MEB model from long-term microwave measurements over a rough field, SMOSREX 2006. Geoscience and Remote Sensing, IEEE Transactions on. 50:1458-1467. doi:10.1109/TGRS.2011.2178421.

Mohanty B.P. 2013. Soil hydraulic property estimation using remote sensing: A review. Vadose Zone Journal. 12. doi:10.2136/vzj2013.06.0100.

Montzka C., H.R. Bogena, L. Weihermuller, F. Jonard, C. Bouzinac, J. Kainulainen, J.E. Balling, A. Loew, E. Rouhe and J. Vanderborght. 2013. Brightness temperature and soil moisture validation at different scales during the SMOS validation campaign in the Rur and Erft catchments, Germany. Ieee Transactions on Geoscience and Remote Sensing. 51:1728-1743. doi:10.1109/tgrs.2012.2206031.

Moret D., I. Braud and J.L. Arrue. 2007. Water balance simulation of a dryland soil during fallow under conventional and conservation tillage in semiarid Aragon, Northeast Spain. Soil & Tillage Research. 92:251-263. doi:10.1016/j.still.2006.03.012.

Moroizumi T. and H. Horino. 2002. The effects of tillage on soil temperature and soil water. Soil science. 167:548-559. doi:35400010914936.0060.

Mualem Y. 1976. New model for predicting hydraulic conductivity of unsaturated porous-media. Water Resources Research. 12:513-522. doi:10.1029/WR012i003p00513.

Mwendera E. and J. Feyen. 1994. Effects of tillage and evaporative demand on the drying characteristics of a silt loam: an experimental study. Soil and Tillage Research. 32:61-69. doi:10.1016/0167-1987(94)90033-7.

Neuweiler I., D. Erdal and M. Dentz. 2012. A Non-Local Richards Equation to Model Unsaturated Flow in Highly Heterogeneous Media under Nonequilibrium Pressure Conditions. Vadose Zone Journal. 11. doi:10.2136/vzj2011.0132.

Newton R.W., Q.R. Black, S. Makanvand, A.J. Blanchard and B.R. Jean. 1982. Soil moisture information and thermal microwave emission. Ieee Transactions on Geoscience and Remote Sensing. 20:275-281. doi:10.1109/tgrs.1982.350443.

Njoku E.G. and D. Entekhabi. 1996. Passive microwave remote sensing of soil moisture. Journal of Hydrology. 184:101-129. doi:10.1016/0022-1694(95)02970-2.

Olioso A., O. Taconet and M. Ben Mehrez. 1996. Estimation of heat and mass fluxes from IR brightness temperature. Geoscience and Remote Sensing, IEEE Transactions on. 34:1184-1190. doi:10.1109/36.536535.

Pellarin T., J.P. Wigneron, J.C. Calvet, M. Berger, H. Douville, P. Ferrazzoli, Y.H. Kerr, E. Lopez-Baeza, J. Pulliainen, L.P. Simmonds and P. Waldteufel. 2003. Two-year global simulation of L-band brightness temperatures over land. Ieee Transactions on Geoscience and Remote Sensing. 41:2135-2139. doi:10.1109/tgrs.2003.815417.

Peters‐Lidard C.D., D.M. Mocko, M. Garcia, J.A. Santanello, M.A. Tischler, M.S. Moran and Y. Wu. 2008. Role of precipitation uncertainty in the estimation of hydrologic soil properties using remotely sensed soil moisture in a semiarid environment. Water Resources Research. 44. doi:10.1029/2007WR005884.

Priesack E. and W. Durner. 2006. Closed-form expression for the multi-modal unsaturated conductivity function. Vadose Zone Journal. 5:121-124. doi:10.2136/vzj2005.0066.

Richard G. and P. Cellier. 1998. Effect of tillage on bare soil energy balance and thermal regime: an experimental study. Agronomie. 18:163-181. doi:dx.doi.org/10.1051/agro:19980301.

Robinson D.A., C.S. Campbell, J.W. Hopmans, B.K. Hornbuckle, S.B. Jones, R. Knight, F. Ogden, J. Selker and O. Wendroth. 2008. Soil moisture measurement for ecological and hydrological watershed-scale observatories: A review. Vadose Zone Journal. 7:358-389. doi:10.2136/vzj2007.0143.

Roth K., R. Schulin, H. Fluhler and W. Attinger. 1990. Calibration of time domain reflectometry for water content measurement using a composite dielectric approach. Water Resources Research. 26:2267-2273. doi:10.1029/90wr01238.

Rydberg T. 1990. Effects of ploughless tillage and straw incorporation on evaporation. Soil and Tillage Research. 17:303-314. doi:10.1016/0167-1987(90)90043-D.

Santanello Jr J.A., C.D. Peters-Lidard, M.E. Garcia, D.M. Mocko, M.A. Tischler, M.S. Moran and D. Thoma. 2007. Using remotely-sensed estimates of soil moisture to infer soil texture and hydraulic properties across a semi-arid watershed. Remote Sensing of Environment. 110:79-97. doi:10.1016/j.rse.2007.02.007.

Schaap M.G. and F.J. Leij. 2000. Improved prediction of unsaturated hydraulic conductivity with the Mualem-van Genuchten model. Soil Science Society of America Journal. 64:843-851. doi:10.2136/sssaj2000.643843x.

Scharnagl B., J. Vrugt, H. Vereecken and M. Herbst. 2011. Inverse modelling of in situ soil water dynamics: investigating the effect of different prior distributions of the soil hydraulic parameters. Hydrology & Earth System Sciences. 15. doi:10.5194/hess-15-3043-2011.

Schluter S., J. Vanderborght and H.J. Vogel. 2012. Hydraulic non-equilibrium during infiltration induced by structural connectivity. Advances in Water Resources. 44:101-112. doi:10.1016/j.advwatres.2012.05.002.

Schmugge T.J. 1985. Remote Sensing of Soil Moisture John Wiley & Sons.

Schoups G. and J.A. Vrugt. 2010. A formal likelihood function for parameter and predictive inference of hydrologic models with correlated, heteroscedastic, and non‐Gaussian errors. Water Resources Research. 46. doi:10.1029/2009WR008933.

Schwank M., J.P. Wigneron, E. Lopez-Baeza, I. Volksch, C. Matzler and Y.H. Kerr. 2012. L-Band Radiative Properties of Vine Vegetation at the MELBEX III SMOS Cal/Val Site. Ieee Transactions on Geoscience and Remote Sensing. 50:1587-1601. doi:10.1109/tgrs.2012.2184126.

Schwank M., I. Volksch, J.P. Wigneron, Y.H. Kerr, A. Mialon, P. de Rosnay and C. Matzler. 2010a. Comparison of Two Bare-Soil Reflectivity Models and Validation With L-Band Radiometer Measurements. Ieee Transactions on Geoscience and Remote Sensing. 48:325-337. doi:10.1109/tgrs.2009.2026894.

Schwank M., A. Wiesmann, C. Werner, C. Matzler, D. Weber, A. Murk, I. Volksch and U. Wegmuller. 2010b. ELBARA II, an L-Band Radiometer System for Soil Moisture Research. Sensors. 10:584-612. doi:10.3390/s100100584.

Shutko A.M. 1982. Microwave radiometry of lands under natural and artificial moistening. Ieee Transactions on Geoscience and Remote Sensing. 20:18-26. doi:10.1109/tgrs.1982.4307514.

Sillon J., G. Richard and I. Cousin. 2003. Tillage and traffic effects on soil hydraulic properties and evaporation. Geoderma. 116:29-46. doi:10.1016/S0016-7061(03)00092-2.

Simunek J., M. Sejna, H. Saito, M. Sakai and M.T. van Genuchten. 2008. The HYDRUS-1D Software Package for Simulating the Movement of Water, Heat, and Multiple Solutes in Variably Saturated Media, Version 4.08 Department of Environmental Sciences, University of California Riverside, Riverside.

Sorooshian S., Q. Duan and V.K. Gupta. 1993. Calibration of rainfall-runoff models: Application of global optimization to the Sacramento Soil Moisture Accounting Model. Water Resources Research. 29:1185-1194. doi:10.1029/92WR02617.

Steenpass C., J. Vanderborght, M. Herbst, J. Simunek and H. Vereecken. 2010. Estimating soil hydraulic properties from infrared measurements of soil surface temperatures and TDR data. Vadose Zone Journal. 9:910-924. doi:10.2136/vzj2009.0176.

Strudley M.W., T.R. Green and J.C. Ascough II. 2008. Tillage effects on soil hydraulic properties in space and time: State of the science. Soil and Tillage Research. 99:4-48. doi:10.1016/j.still.2008.01.007.

Sun Y., J. Lin, P. Schulze Lammers and L. Damerow. 2006. Estimating surface porosity by roughness measurement in a silt‐loam field. Journal of Plant Nutrition and Soil Science. 169:630-632. doi:10.1002/jpln.200521935.

Topp G.C., J.L. Davis and A.P. Annan. 1980. Electromagnetic determination of soil water content: Measurements in coaxial transmission lines. Water Resources Research. 16:574-582. doi:10.1029/WR016i003p00574.

Ulaby F., R. Moore and A. Fung. 1986. Microwave Remote Sensing: Active and Passive, vol. III, Volume Scattering and Emission Theory, Advanced Systems and Applications.

Van Genuchten M.T. 1980. A Closed-form Equation for Predicting the Hydraulic Conductivity of Unsaturated Soils. Soil Science Society of America Journal. 44:892-898. doi:10.2136/sssaj1980.03615995004400050002x.

Vanderborght J., J.A. Huisman, J. van der Kruk and H. Vereecken. 2013. Geophysical Methods for Field-Scale Imaging of Root Zone Properties and Processes, In: S. H. Anderson and J. W. Hopmans (Eds.), Soil–Water–Root Processes: Advances in Tomography and Imaging, SSSA, Madison, WI 53711, USA. pp. 247-281.

Vereecken H., R. Kasteel, J. Vanderborght and T. Harter. 2007. Upscaling hydraulic properties and soil water flow processes in heterogeneous soils: A review. Vadose Zone Journal. 6:1-28. doi:10.2136/vzj2006.0055.

Vereecken H., J.A. Huisman, H. Bogena, J. Vanderborght, J.A. Vrugt and J.W. Hopmans. 2008. On the value of soil moisture measurements in vadose zone hydrology: A review. Water Resources Research. 44. doi:10.1029/2008wr006829.

Vrugt J., C. Diks and M. Clark. 2008a. Ensemble Bayesian model averaging using Markov Chain Monte Carlo sampling. Environmental Fluid Mechanics. 8:579-595. doi:10.1007/s10652-008-9106-3.

Vrugt J.A. and J.H. Dane. 2005. Inverse Modeling of Soil Hydraulic Properties, In: M. G. Anderson (Ed.), Encyclopedia of Hydrological Sciences, John Wiley & Sons, Chichester, UK. pp. 1151-1170.

Vrugt J.A., C.J.F. ter Braak, M.P. Clark, J.M. Hyman and B.A. Robinson. 2008b. Treatment of Input Uncertainty in Hydrologic Modeling: Doing Hydrology Backwards with Markov Chain Monte Carlo Simulation. Water Resources Research. doi:10.1029/2007WR006720.

Vrugt J.A., C. Ter Braak, C. Diks, B.A. Robinson, J.M. Hyman and D. Higdon. 2009. Accelerating Markov chain Monte Carlo simulation by differential evolution with self-adaptive randomized subspace sampling. International Journal of Nonlinear Sciences and Numerical Simulation. 10:273-290. doi:10.1515/IJNSNS.2009.10.3.273.

Wang J.R. 1987. Microwave emission from smooth bare fields and soil moisture sampling depth. Ieee Transactions on Geoscience and Remote Sensing. 25:616-622. doi:10.1109/tgrs.1987.289840.

Wang J.R. and T.J. Schmugge. 1980. An empirical model for the complex dielectric permittivity of soils as a function of water content. Ieee Transactions on Geoscience and Remote Sensing. 18:288-295. doi:10.1109/tgrs.1980.350304.

Weihermuller L., J.A. Huisman, S. Lambot, M. Herbst and H. Vereecken. 2007. Mapping the spatial variation of soil water content at the field scale with different ground penetrating radar techniques. Journal of Hydrology. 340:205-216. doi:10.1016/j.jhydrol.2007.03.013.

Weynants M., H. Vereecken and M. Javaux. 2009. Revisiting Vereecken Pedotransfer Functions: Introducing a Closed-Form Hydraulic Model. Vadose Zone Journal. 8:86-95. doi:10.2136/vzj2008.0062.

Wigneron J.P., L. Laguerre and Y.H. Kerr. 2001. A simple parameterization of the L-band microwave emission from rough agricultural soils. Ieee Transactions on Geoscience and Remote Sensing. 39:1697-1707. doi:10.1109/36.942548.

Wigneron J.P., A. Chanzy, P. de Rosnay, C. Rudiger and J.C. Calvet. 2008. Estimating the effective soil temperature at L-band as a function of soil properties. Ieee Transactions on Geoscience and Remote Sensing. 46:797-807. doi:10.1109/tgrs.2007.914806.

Wigneron J.P., A. Chanzy, Y.H. Kerr, H. Lawrence, J.C. Shi, M.J. Escorihuela, V. Mironov, A. Mialon, F. Demontoux, P. de Rosnay and K. Saleh-Contell. 2011. Evaluating an Improved Parameterization of the Soil Emission in L-MEB. Ieee Transactions on Geoscience and Remote Sensing. 49:1177-1189. doi:10.1109/tgrs.2010.2075935.

Zacharias S., H. Bogena, L. Samaniego, M. Mauder, R. Fuss, T. Putz, M. Frenzel, M. Schwank, C. Baessler, K. Butterbach-Bahl, O. Bens, E. Borg, A. Brauer, P. Dietrich, I. Hajnsek, G. Helle, R. Kiese, H. Kunstmann, S. Klotz, J.C. Munch, H. Papen, E. Priesack, H.P. Schmid, R. Steinbrecher, U. Rosenbaum, G.

Teutsch and H. Vereecken. 2011. A Network of Terrestrial Environmental Observatories in Germany. Vadose Zone Journal. 10:955-973. doi:10.2136/vzj2010.0139.

Zannoni M., A. Tartari, M. Gervasi, G. Boella, G. Sironi, A. De Lucia, A. Passerini and F. Cavaliere. 2008. TRIS. I. Absolute Measurements of the Sky Brightness Temperature at 0.6, 0.82, and 2.5 GHz. The Astrophysical Journal. 688:12. doi:10.1086/592133.

Zobeck T.M. and C.A. Onstad. 1987. Tillage and rainfall effects on random roughness: a review. Soil & Tillage Research. 9:1-20. doi:10.1016/0167-1987(87)90047-x.

Zreda M., D. Desilets, T. Ferré and R.L. Scott. 2008. Measuring soil moisture content non‐invasively at intermediate spatial scale using cosmic‐ray neutrons. Geophysical Research Letters. 35. doi:10.1029/2008GL035655.

Acknowledgements

I would like to thank to my direct supervisor Prof. Jan Vanderborght for the professional guidance and valuable support, all ideas and the whole understanding.

This dissertation would have let to nowhere without the encouragement and valuable support of Assist. Prof. Kosta Kostov, Institute of Electronics, Bulgarian Academy of Sciences.

I would like to express my very great appreciation to the head of the Institute of Bio- and Geoscience Agrosphere (IBG-3) Prof. Harry Vereecken for the possibility he gave me to work in the Agrosphere.

I'm also very grateful to Prof. Peter Schulze Lammers and Dr. Lutz Damerow for their valuable and constructive suggestions during the planning and development of the field work.

I especially thank Dr. Khan Zaib Jadoon, who provided me the basics of the coupled inversion procedure. I am particularly grateful for all model settings and discussions to Dr. Lutz Weihermüller, Dr. Mike Schwank and Dr. Francois Jonard.

My special thanks are extended to Ferdinand Engels, Normen Hermes and Rainer Harms, who were strongly involved in the hard field work and also to Anke Langen for the analysis of the soil core samples.

I'm thankful to Heinrich Meier, Werner Schmitz and the whole team around Heinz Jagdfeld, who helped me to test the L-band radiometer and later on to create and calculate the holding construction the L-band radiometer. I also would like to thank the team around Ayhan Egmen and Hans-Dieter Schnabel who build this construction.

I wish to acknowledge the help provided by Dr. Thomas J. Jackson, Dr. Rajat Bindlish, Dr. Yakov A. Pachepsky for consultations during my stay abroad in ARS USDA.

Advices given by Dr. Jutta Bikowski, Dr. Iliana Mladenova, Dr. Nils Borchard has been a great help during the whole writing period.

I would like to thank all the PhD students of the IBG-3 and especially my former colleagues Dr. Ulrike Rosenbaum, Dr. Christian Steenpass, Dr. Cho Miltin Mboh, Nils Prolingheuer and Benedikt Scharnagl for their help when I needed it.

I wish to thank my friends, my parents and especially my brother for their support.

Finally, I would like to thank to Boryana Dimitrova and Emilia Dimitrova for their love and patience. I love you!

Schriften des Forschungszentrums Jülich
Reihe Energie & Umwelt / Energy & Environment

Band / Volume 280
IEK-3 Report 2015
Systemforschung und –technik für eine nachhaltige Energieversorgung
(2015)
ISBN: 978-3-95806-078-4

Band / Volume 281
Integration of the German energy transition in the EU-context
A. Ernst (2015), 76 pp
ISBN: 978-3-95806-079-1

Band / Volume 282
Modelling and Experimental Validation of the Viscosity of Liquid Phases in Oxide Systems Relevant to Fuel Slags
G. Wu (2015), XVI, 170 pp
ISBN: 978-3-95806-081-4

Band / Volume 283
Entwicklung von geträgerten protonenleitenden Dünnschichtmembranen für die Wasserstoffabtrennung
W. Deibert (2015), XI, 117 pp
ISBN: 978-3-95806-082-1

Band / Volume 284
Thermochemische Beständigkeit von keramischen Membranen und Katalysatoren für die H_2-Abtrennung in CO-Shift-Reaktoren
E. M. H. Forster (2015), X, 137 pp
ISBN: 978-3-95806-084-5

Band / Volume 285
Spektrale aktinische Flussdichten und Photolysefrequenzen - Untersuchungen in der atmosphärischen Grenzschicht und der freien Troposphäre
I. M. Lohse (2015), VI, 111, VII-XXIII pp
ISBN: 978-3-95806-086-9

Band / Volume 286
Neue Charakterisierungsmethoden für die Gasdiffusionslage in PEM-Brennstoffzellen vor dem Hintergrund produktionsprozessbedingter Materialschwankungen
S. M. Bach (2015), VIII, 149 pp
ISBN: 978-3-95806-088-3

Schriften des Forschungszentrums Jülich
Reihe Energie & Umwelt / Energy & Environment

Band / Volume 287
Using the anisotropy of electrical properties for the characterization of sedimentological structures and preferential flow processes
S. Al-Hazaimay (2015), xxii, 94 pp
ISBN: 978-3-95806-090-6

Band / Volume 288
Aktivitätsuntersuchungen und Methoden zur Regeneration von Katalysatoren für die autotherme Reformierung von Dieselkraftstoffen
K. Löhken (2015), II, 147 pp
ISBN: 978-3-95806-093-7

Band / Volume 289
Large-Scale Three Dimensional Modelling of a Direct Methanol Fuel Cell Stack
J. W. McIntyre (2015), 138 pp
ISBN: 978-3-95806-094-4

Band / Volume 290
Abscheidung von Wärmedämmschichtsystemen mit dem Plasma Spray-Physical Vapor Deposition- (PS-PVD-) Prozess – Untersuchung des Prozesses und der hergestellten Schichten
S. Rezanka (2015), XII, 234 pp
ISBN: 978-3-95806-095-1

Band / Volume 291
Characterization & Modification of Copper and Iron Oxide Nanoparticles for Application as Absorber Material in Silicon based Thin Film Solar Cells
M. R. Nuys (2015), XII, 123 pp
ISBN: 978-3-95806-096-8

Band / Volume 292
Interpretation of L-band brightness temperatures of differently tilled bare soil plots
M. Dimitrov (2015), XIV, 116 pp
ISBN: 978-3-95806-098-2

Weitere ***Schriften des Verlags im Forschungszentrum Jülich*** unter
http://wwwzb1.fz-juelich.de/verlagextern1/index.asp

Interpretation of L-band brightness temperatures of differently tilled bare soil plots

Marin Dimitrov

Energie & Umwelt / Energy & Environment
Band / Volume 292
ISBN 978-3-95806-098-2

JÜLICH
FORSCHUNGSZENTRUM

Energie & Umwelt / Energy & Environment
Band / Volume 292
ISBN 978-3-95806-098-2

JÜLICH
FORSCHUNGSZENTRUM